Technical Report

DSWA-TR-97-83

Development of Novel Spectroscopic Diagnostics for Plasma Radiation Sources

Approved for public release; distribution is unlimited.

December 1999

Prepared for:
Defense Threat Reduction Agency
45045 Aviation Drive
Dulles, VA 20166-7517

DNA001-93-C-0206

Eugene J. Clothiaux
Eugene Oks
Joseph D. Perez

Prepared by: Auburn University
Department of Physics
206 Allison Laboratory
Auburn, AL 36849-5311

DISTRIBUTION LIST UPDATE

This mailer is provided to enable DTRA to maintain current distribution lists for reports. (We would appreciate you providing the requested information.)

- ❑ Add the individual listed to your distribution list.
- ❑ Delete the cited organization/individual.
- ❑ Change of address.

Note:
Please return the mailing label from the document so that any additions, changes, corrections or deletions can be made easily. For distribution cancellation or more information call DTRA/ADM (703) 325-1036.

NAME: _____

ORGANIZATION: _____

OLD ADDRESS	NEW ADDRESS
_____	_____
_____	_____
_____	_____

TELEPHONE NUMBER: ( ) _____

DTRA PUBLICATION NUMBER/TITLE	CHANGES/DELETIONS/ADDITIONS, etc.) *(Attach Sheet if more Space is Required)*
_____	_____
_____	_____
_____	_____

DTRA or other GOVERNMENT CONTRACT NUMBER: _____

CERTIFICATION of NEED-TO-KNOW BY GOVERNMENT SPONSOR (if other than DTRA):

SPONSORING ORGANIZATION: _____

CONTRACTING OFFICER or REPRESENTATIVE: _____

SIGNATURE: _____

CUT HERE AND RETURN

DEFENSE THREAT REDUCTION AGENCY
ATTN: ADM
45045 AVIATION DRIVE
DULLES, VA 20166-7517

DEFENSE THREAT REDUCTION AGENCY
ATTN: ADM
6810 TELEGRAPH ROAD
ALEXANDRIA, VA 22310-3398

REPORT DOCUMENTATION PAGE

Form Approved OMB No. 0704-0188

1. AGENCY USE ONLY *(Leave blank)*	2. REPORT DATE	3. REPORT TYPE AND DATES COVERED
	991200	Technical 28Sep93 - 30Sep96

4. TITLE AND SUBTITLE

Development of Novel Spectroscopic Diagnostics for Plasma Radiation Sources

5. FUNDING NUMBERS

C - DNA 001-93-C-0206
PE - 62715H
PR - AB
TA- GH
WU - DH00023

6. AUTHOR(S)

Eugene J. Clothiaux, Eugene Oks, Joseph D. Perez

7. PERFORMING ORGANIZATION NAME(S) AND ADDRESS(ES)

Auburn University
Department of Physics
206 Allison Laboratory
Auburn, AL 36849-5311

8. PERFORMING ORGANIZATION REPORT NUMBER

9. SPONSORING/MONITORING AGENCY NAME(S) AND ADDRESS(ES)

Defense Special Weapons Agency
6801 Telegraph Road
Alexandria, VA 22310-3398

EST/Schneider

10. SPONSORING/MONITORING AGENCY REPORT NUMBER

DSWA-TR-97-83

11. SUPPLEMENTARY NOTES

This work was sponsored by the Defense Special Weapons Agency under RDT&E RMC code B 4662 D AB GH 00023 5400 A 25904D.

12a. DISTRIBUTION/AVAILABILITY STATEMENT

Approved for public release; distribution is unlimited

12b. DISTRIBUTION CODE

13. ABSTRACT *(Maximum 200 words)*

This report gives the details of experiments performed to measure the levels and the angular distribution of oscillating electric fields in an aluminum plasma produced by the Phoenix advanced pulsed radiation source. The electric field values were obtained by measuring the L_β, L_γ, L_δ, and L_ϵ line profiles of Al XIII and fitting the profiles to a model for the Phoenix plasma source.

The model attempts to take into account all of the mechanisms which lead to broadening of the observed profiles for the conditions present in the Phoenix plasma. The main broadening mechanisms used in the model include Doppler broadening from the bulk motion of the plasma, Stark broadening by electrons, ions and oscillating electric fields, and self absorption.

In addition to the flat crystal and two curved crystal spectrometers used to measure the lines profiles, a pinhole camera and a four frame camera were used to try and obtain the size of the most dense retions in the plasma.

14. SUBJECT TERMS

Phoenix radiation source
Oscillating electric fields
Four frame camera
X-ray spectroscopy
Line broadening mechanisms
Crystal spectrographs

15. NUMBER OF PAGES

159

16. PRICE CODE

17. SECURITY CLASSIFICATION OF REPORT	18. SECURITY CLASSIFICATION OF THIS PAGE	19. SECURITY CLASSIFICATION OF ABSTRACT	20. LIMITATION OF ABSTRACT
UNCLASSIFIED	UNCLASSIFIED	UNCLASSIFIED	SAR

CLASSIFIED BY: N/A since Unclassified

DECLASSIFY ON: N/A since Unclassified

13. ABSTRACT (Continued)

The size of these "hot spots" were found to be less than 500 um. From fits of the experimental profiles to the data, the level of anomalous electric fields in the Phoenix plasma source were found to be E_o = 1 - 9 GV/cm, indicative of a strong Langmuir turbulence. The fields were also found to develop anisotropically, primarily along the direction of the discharge.

TABLE OF CONTENTS

LIST OF FIGURES

TABLES

SECTION 1
INTRODUCTION

Since using nuclear devices to test military hardware is clearly out of the question, an alternate approach is needed. To this end, plasma radiation sources were designed and built, and one such device is the Phoenix plasma radiation source (PRS).

The goal of the Phoenix project is to produce x rays with wavelengths less than 1 Å to best simulate the radiation produced by nuclear devices. The Phoenix machine produces the radiation by exploding wires and driving them into a z-pinch. During the compression of the plasma, electrons are stripped from the atoms, resulting in highly ionized atoms. To produce high energy x rays it is necessary to remove all but a few electrons from the atoms. Since the remaining electrons will be tightly bound to the nucleus, the radiation they produce when they undergo transitions will be in the x-ray region. The energy of the x rays scale with atomic number Z, and it is necessary to use iron or copper to achieve radiation with wavelengths less than 1 Å. If copper or iron wires are used in the Phoenix device however, the highest ionization states of the atoms are not reached. An instability is thought to develop which prevents a total collapse of the plasma column. There are several possible instabilities which can develop, but it is still unclear which one is responsible for the disruption of the pinch.

One theory is that this instability is due to anomalous electric fields (AEFs).[1] These

fields are manifested as waves which are disruptive to a smooth collapse of the plasma. AEFs have been experimentally verified in many plasma devices with lower densities than Phoenix.[2] It is suspected that these AEFs may also occur in a dense plasma like in the Phoenix device, and to test this hypothesis a method for measuring such electric fields has been developed. The effect of these electric fields on emitting atoms is quite complex. By knowing how these electric fields broaden the spectral lines produced by the atoms in the plasma, a measure of the electric fields can be made. This dissertation describes and discusses the experiments performed on the Phoenix device to measure the levels and angular distribution of AEFs in a superdense plasma. An aluminum plasma was used for the study, since the hydrogen-like state can be reached where the affects of oscillating electric fields on line broadening are well known. The presence of these fields in a plasma of this density would suggest that this type of instability may be present in superdense plasmas and needs to be considered as a possible explanation for the inability to reach the highest ionization states in higher Z elements.

SECTION 2
DENSE PLASMA MODEL

2.1 PRELIMINARY CONSIDERATIONS.

The key to plasma spectroscopy is understanding the internal state of a plasma by observing the radiation emitted from the plasma. To do this it is necessary to have a model which can predict lineshapes based on the physical parameters of the plasma. The model used in this analysis assumes that the observed lineshapes result from three primary broadening mechanisms: Doppler broadening, Stark broadening and self absorption. Zeeman splitting is also considered as a possible broadening mechanism. In the Phoenix device it is expected that the plasma has an electron density of $N_e >> 10^{20}$ cm^{-3}, and an electron temperature of $T_e \approx T_i \approx 1$ keV. For this density and temperature, the electron collision frequency ω_e will be on the order of 10^{13} s^{-1}. Waves that do not have a frequency higher than this collision frequency will not propagate. The only waves which can have a frequency higher than this collision frequency will be Langmuir waves with frequencies at $\omega_{pe} \approx 10^{15}$ s^{-1}.[3] For that reason, the source of the oscillating electric fields in the model was taken to be Langmuir waves.

2.2 LINE BROADENING MECHANISMS IN THE PHOENIX PLASMA SOURCE.

This section outlines the model used in the analysis of the spectra obtained on the Phoenix device. Reviews of the theory behind the broadening mechanisms, relevant to the model, are presented here.

2.2.1 Doppler Broadening.

Doppler broadening of spectral lines results from the relative motion of emitting atoms or ions towards or away from the observer.[4] Photons which are emitted with a fixed wavelength, as given by the difference in energy levels of the atom, are shifted when observed in the rest frame of the laboratory. The two sources of ion motion in plasmas are thermal motion and bulk plasma motion.

For the thermal motion of the ions where the velocity distribution is assumed to be Maxwellian, the number of atoms dN with velocity between v and $v+dv$ will be given by[5]

$$dN(v) = N_0 \exp(-\frac{mv^2}{2KT})dv . \tag{2.1}$$

Using the Doppler formula $\lambda = \lambda_0[1 \pm (v/c)]$, the expression for the Doppler broadening, which gives the number of atoms emitting with wavelength between λ and $\lambda + d\lambda$, is

$$dN(\lambda) = \left(\frac{Mc^2}{2\pi KT\lambda_0^2}\right) \exp\left[-\frac{mc^2}{2KT}\left(\frac{\Delta\lambda}{\lambda_0}\right)^2\right] d\lambda . \tag{2.2}$$

Since the intensity is proportional to the number of emitters in the range λ to $\lambda + d\lambda$, Eq. (2.2) gives the Doppler broadened profile. The resulting half width at half maximum of this profile is

$$\Delta\lambda_{HWHM} = \frac{\lambda}{2c}\left[\frac{2KT\log 2}{M}\right]^{1/2} . \tag{2.3}$$

For an estimated ion plasma temperature in the Phoenix device of $T \approx 1$ keV at $\lambda = 6.053$ Å (Al XIII), the resulting HWHM is 1.35 mÅ.

In many laboratory plasma devices, such as tokamaks and stellarators, the bulk motion of the ions is small compared to the thermal motion.[6,7] In z-pinch devices, however, the bulk plasma velocities are on the order of 0.1 % c and are generally larger than the ion thermal velocities due to the presence of strong driving currents.[8] The bulk plasma motion then plays a dominant role in the Doppler broadening of the spectral lines. Our model assumes that the velocity distribution of the bulk plasma is Gaussian, as commonly done when there is no information about the velocity distribution.

The velocity distribution for the bulk plasma motion is constructed by replacing the thermal velocity by an average bulk plasma velocity v such that

$$\frac{2KT}{M} = v_t^{\,2} \Rightarrow v^2 . \tag{2.4}$$

Introducing a new parameter $b = 10^3\, v/c$, the width of the Doppler profile $\Delta\lambda_D$ is given by $\Delta\lambda_D = 10^{-3} b\lambda_0 (m\text{Å})$. The normalized line profile then becomes

$$G(\Delta\lambda, \Delta\lambda_D) = \frac{1}{\Delta\lambda_D \sqrt{\pi}} e^{-\frac{\Delta\lambda^2}{\Delta\lambda_D^{\,2}}}, \tag{2.5}$$

with a halfwidth at half maximum given by $\Delta\lambda_{HWHM}\left(m\text{Å}\right) = b\lambda_0\left(m\text{Å}\right)10^{-3}\sqrt{\ln 2}$. A b value of 1 for $\lambda_0 = 6.053$ Å leads to a $HWHM \approx 5.0\ m$ Å. This value of b corresponds to a bulk velocity of 0.1% c.

The complete Doppler broadening of the line will realistically be a convolution of the Doppler broadening from both the thermal motion and bulk motion. Since both profiles are Gaussian, the convoluted line will also be Gaussian. The width of the convoluted profile will be given by the square root of the square of the widths of the individual Gaussians. Since the broadening by bulk motion is significantly larger than that of the thermal broadening, the resulting width will be close to that of the bulk plasma motion alone. For this reason, the thermal Doppler broadening is ignored in the model.

2.2.2 Stark Broadening.

Stark broadening results from the change in energy levels and wave functions of an atom due to the presence of electric fields. In a plasma, static macroscopic electric fields are not present due to the shielding effects of the plasma. The atoms encounter electric fields only from neighboring charged particles and from waves traveling in the plasma. We start our discussion of Stark broadening by briefly summarizing the solution of the linear Stark effect using parabolic coordinates.[9-11]

2.2.2.1 Linear Stark Effect. The change in energy levels of an atom due to a constant external electric field can be found from a solution of the Schrödinger equation as $H = H_0 + H'$, where H_0 is the hydrogenic Hamiltonian and $H' = qFZ$ is the interaction term with the electric field F. The problem becomes one of solving Schrödinger's equation for the system

$$\nabla^2 u + \frac{2m}{\hbar}\left[E + \frac{Ze^2}{r} + Fez\right]u = 0\,. \tag{2.6}$$

As long as the electric field is not too strong, the potential term arising from F can be treated with standard perturbation theory using the wave functions for the unperturbed hydrogen atom. Schrödingers' equation for a H-like atom without an electric field, solved in parabolic coordinates, has the well known solutions

$$u = \frac{e^{\pm im\rho}}{\sqrt{\pi n}} \frac{n_1!^2\, n_2!^2\, \varepsilon^{m+3/2}}{(n_1+m)!^{3/2}(n_2+m)!^{3/2}} e^{-\varepsilon(\xi+\eta)/2} (\xi\eta)^{m/2} L^m_{n_1+m}(\varepsilon\xi) L^m_{n_2+m}(\varepsilon\eta) \qquad (2.7)$$

where

$\varepsilon = \sqrt{-E}$

L^λ_μ = Laguerre polynomials

n, n_1, n_2, m = parabolic quantum numbers that must satisfy $n = n_1 + n_2 + m + 1$

n = principle quantum number

m = magnetic quantum number having positive values less than n

With the electric field present, a perturbation is performed and the corrected energies to first order are

$$E_{n,n_1,n_2} = -\frac{1}{2}\frac{Z^2}{n^2}\frac{Me^4}{\hbar^3} + \frac{3}{2}\frac{ea_0Fn}{Z\hbar}(n_1 - n_2). \qquad (2.8)$$

The second term is the linear Stark shift of the energy level given by the quantum numbers n, n_1, and n_2.

2.2.1 Allowed Transitions for Lyman β, γ, δ and ε.

For transitions between levels in hydrogen-like atoms the dipole selection rules must be satisfied, that is $\Delta m = 0$ for the π polarization and $\Delta m = \pm 1$ for the σ polarization.[12] The

π polarization corresponds to the electric field of the radiation along the direction of the applied electric field and the σ polarization corresponds to the electric field of the radiation perpendicular to the direction of the applied electric field. In this experiment we are interested in the Lyman β, γ, δ, and ε lines corresponding to transitions to the ground state (n = 1). Figure 2-1 shows the Stark components for each of the allowed transitions with corresponding intensities and polarizations for each of these lines. The energy shift of each component is given by

$$\Delta E = \frac{3}{2}\frac{ea_0F}{Z\hbar}\Delta k \tag{2.9}$$

where

$$\Delta k = n'(n_1' - n_2') - n(n_1 - n_2).$$

2.2.2 Electric Fields Arising from Charged Particles in a Plasma.

The interactions of ions with the neighboring charged particles depend upon the properties of the perturbing particles.[4,13] For slowly moving particles such as ions, the electric fields do not vary rapidly in time. The resulting electric field can then be calculated by taking a statistical average over the perturbers using a quasi-static approximation. Fast moving particles, such as electrons, interact with the atom by collisions. When electrons collide with the ions they cause phase and amplitude modulations of the radiating oscillator and shorten its lifetime. All three of these electronic effects lead to spectral broadening and are treated with an impact approximation.

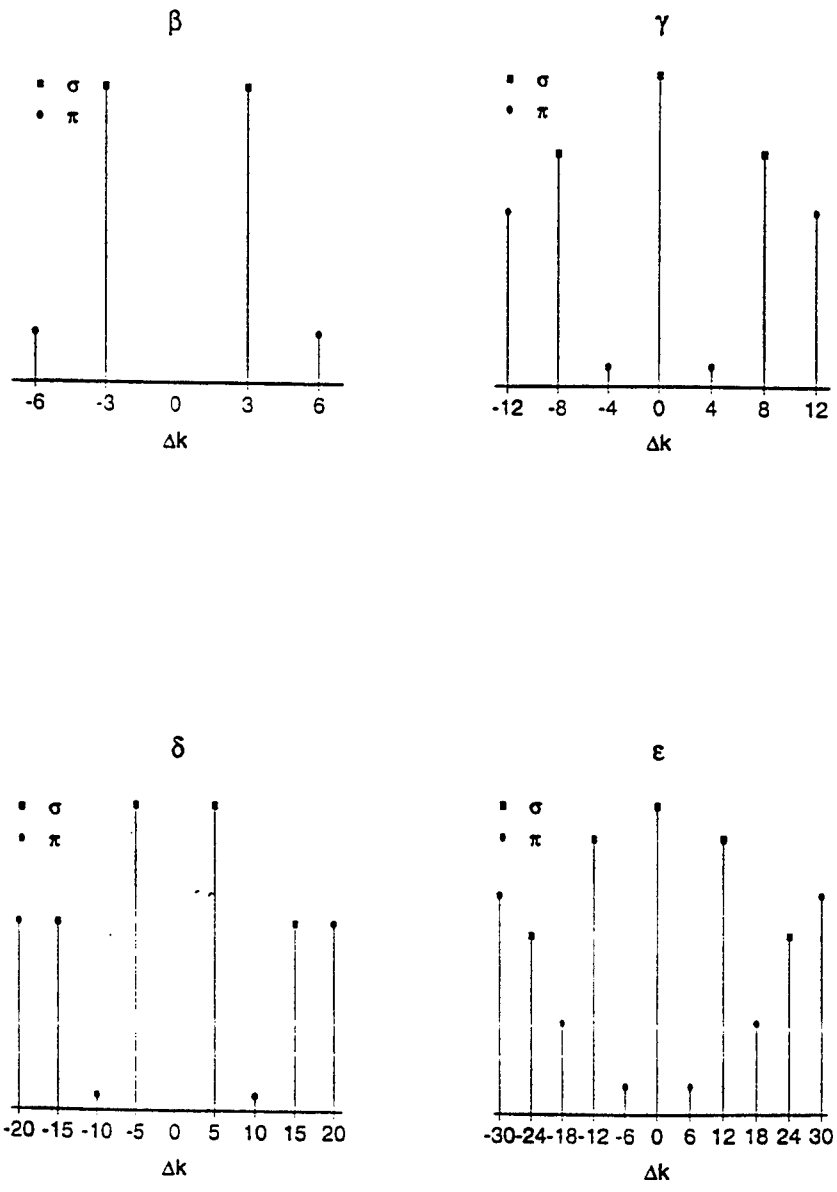

Figure 2-1. Stark components for Lyman β, γ, δ and ε.

The range of validity for these two approximations depends on the number of particles in the Weisskopf sphere given by $g \equiv (\rho_w / \rho_N)^3$ where the Weisskopf radius ρ_w and the average distance between particles ρ_N are [14, 15]

$$\rho_w = \frac{3}{2}\frac{na_0e^2}{\hbar v} \tag{2.10}$$

and

$$\rho_N = N^{-1/3}. \tag{2.11}$$

The Weisskopf radius gives the effective optical cross section for the collisions of particles with the radiating ion. If the number of particles in the Weisskopf sphere is small so that g << 1, then the nearest perturbing particle causes the dominant broadening and the impact approximation can be used. If the number of particles is large so that g >> 1, then the atom interacts with a large number of particles allowing for a statistical approach and the quasi-static approximation can be used.

2.2.2.1 Ion Broadening by the Quasi-Static Approximation. We first consider the emitter interacting with neighboring ions. Since the ions are massive and slow, the ions can be treated as fixed for the calculation of the electric fields they produce.[16]

We need to calculate the distribution $W_0(F)$ of electric fields F that an emitting atom or ion encounters from neighboring ions. We assume that the ions are statistically independent so that the probability of finding a field $\vec{F}$ in the interval from $\vec{F}$ to $\vec{F} + d\vec{F}$ is given by

$$W_0(\bar{F}) = \int \ldots \int \delta\left(\bar{F} - \sum_{j=1}^{n} \bar{F}_j\right) P(\bar{r}_1, \bar{r}_2, \ldots, \bar{r}_n) d^3 r_1 d^3 r_2, \ldots dr_n{}^3 \qquad (2.12)$$

where

$$\bar{F}_j = -\frac{Z_p e \bar{r}_j}{r_j^3}, \qquad (2.13)$$

the Coulomb field of each neighboring ion. $P(\bar{r}_1, \bar{r}_2, \ldots, \bar{r}_n)$ is the probability of finding ion 1 in the range $\bar{r}_1$ to $\bar{r}_1 + \mathrm{d}\bar{r}_1$, finding ion 2 in the range $\bar{r}_2$ to $\bar{r}_2 + \mathrm{d}\bar{r}_2$, etc. Since the particles are statistically independent, this probability will be given simply by V^{-n}.

For isotropic plasmas $W_0(\bar{F})$ only depends upon the magnitude of $\bar{F}$, so we have $W(F) = 4\pi F^2 W_0(\bar{F})$. Carrying out the integration we arrive at the result first obtained by Holtsmark, namely,

$$W(u) = \frac{2\beta}{\pi} \int_0^{\infty} x e^{-x^{3/2}} \sin(ux) dx, \qquad (2.14)$$

where

$$u = F / F_0$$
$$F_0 = 2.6 Z^{1/3} e N_e{}^{2/3}. \text{ (17)}$$

For our model, we define a dimensionless variable C for density, such that $N_e = C$ 1.56 x 10^{22} cm^{-3}.

To get the line profile from this distribution of electric fields we find the wavelength change $\Delta\lambda$ associated with the Stark shift due to the electric field F,

$$\Delta\lambda = \frac{3}{4\pi} \frac{e a_0 \lambda_0^2}{\hbar Z c} n(n_1 - n_2) F. \qquad (2.15)$$

For a transition between two levels, where both levels are split under the electric field, the change in wavelength from the unperturbed transition will then be given by

$$\Delta\lambda_{n\to n'} = \frac{3}{4\pi}\frac{ea_0\lambda_0^2}{\hbar Zc}F\Delta k, \tag{2.16}$$

where

Δk = Stark constant associated with the shift between the two energy levels given by $\Delta k = n(n_1 - n_2) - n'(n_1' - n_2')$.

Defining $\Delta_0 = 3ea_0\lambda^2{}_0 / 4\pi\hbar cZ$, then $F = \Delta\lambda_{n\to n'} / \Delta_0\Delta k$ and $u = \Delta\lambda_{n\to n'} / \Delta_0 F_0\Delta k$, and the line profile for ion broadening is given by

$$I(\Delta\lambda, \Delta k) = \int du\, W(u)\,\delta(\Delta\lambda - \Delta_0 F_0 u\,\Delta k) = \frac{1}{\Delta_0 F_0 \Delta k} W(\Delta\lambda / \Delta_0 F_0 \Delta k). \tag{2.17}$$

This profile does not exhibit maximum intensity at the line center, see Figure 2-2. This occurs because the most probable electric field that the atom will encounter will be different from zero, thus leading to a shift of wavelengths from the zero field values. Figure 2-2 gives the shift and the width of the Holtsmark profiles as a function of $C^{2/3}\Delta k$ for the L_β and L_γ lines of Al XIII. From this graph we can get an idea of the size of the broadening due to the neighboring ions as a function of the density and the Stark constants.

2.2.2.2 Electron Broadening by the Impact Approximation. For the impact approximation, we require that the duration of the collision between the electron and atom is small compared to the time between collisions. The assumptions of this theory are[18]

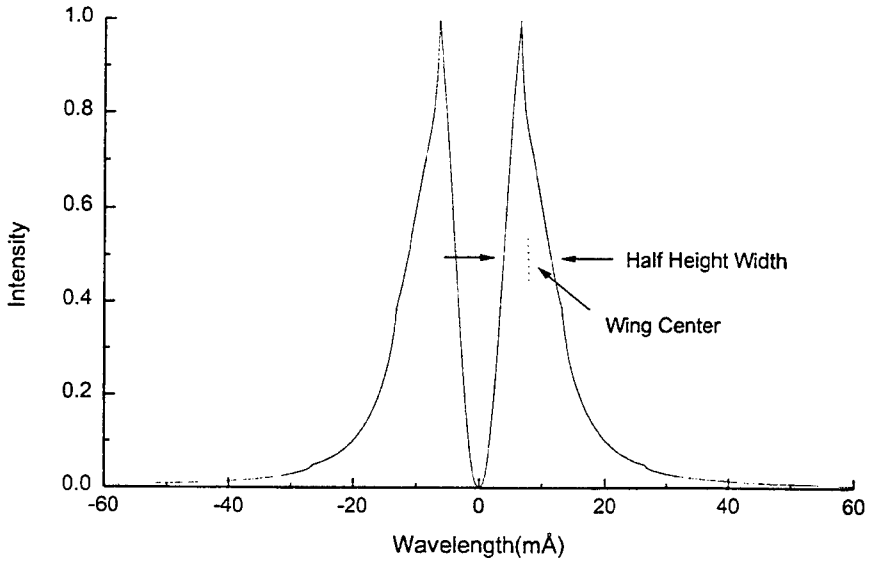

(a) Holtsmark profile for Lyman γ

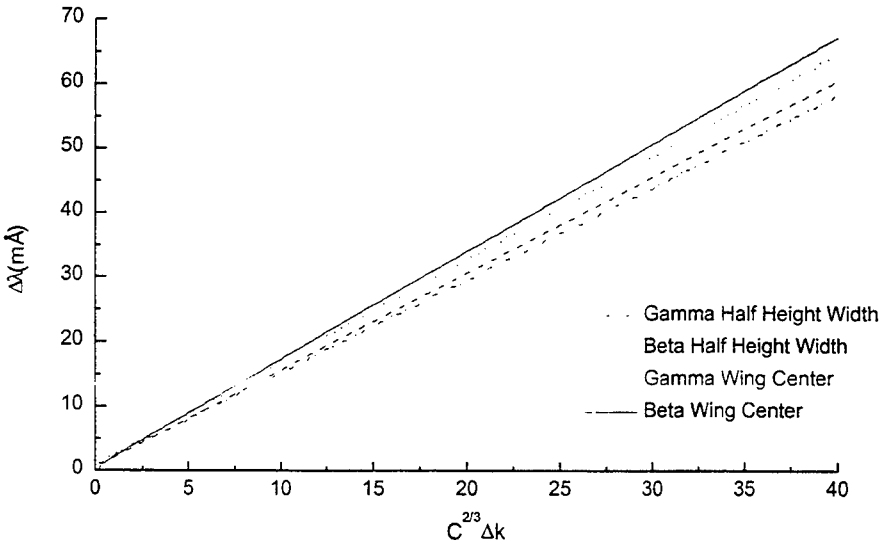

(b) Wing center and half height of the Holtsmark profiles . $C^{2/3}\Delta k$.

Figure 2-2. Holtsmark profiles as a function of $C^{2/3}\Delta k$.

(a) Relative motion of the atom and perturbing particle is quasi-classical, so that one can use the concept of trajectories.

(b) The trajectory is rectilinear.

(c) Interactions with the nearest perturbing particle play the principle role in the broadening.

With these assumptions, the resulting profile of an isolated line in the impact approximation is Lorentzian and the profile is given by

$$I(\omega) = \frac{\gamma}{2\pi} \frac{1}{(\omega - \Delta)^2 + \left(\frac{\gamma}{2}\right)^2}, \tag{2.18}$$

where

$\gamma = 2N\langle v\sigma' \rangle$, the width of the profile

$\Delta = N\langle v\sigma'' \rangle$, the shift of the profile [19,20]

σ', σ'' = cross sections associated with the width and shift.

Physically the broadening is predominantly due to the disruption of coherence of the emitted radiation, so that the radiation from the atom is broken up into wave packets each with internal frequency ω_0. The Fourier analysis of the wave packets produced leads to broadening. Under the impact approximation, the width of the resulting line γ is given by the electron impact width

$$\gamma_e = N_e v_e \sigma_w \ln \Lambda, \tag{2.19}$$

where

$\sigma_w = \pi\rho_w^2$, the effective optical cross section of the atom

The ln Λ term comes from the limits of the impact parameter in determining the cross section.[21] The electron impact width in terms of plasma parameters is given by

$$\gamma_e \approx \frac{n^4\hbar^2}{Z^2 m_e{}^2 v_{Te}} N_e \ln \frac{T_e}{n^2 \hbar \omega_{pe}}, \tag{2.20}$$

where

$$v_{Te} = \sqrt{T_e / m_e}\ .$$

For Al ($Z = 13$) with an electron temperature of 1 keV,

$$\gamma_e = 3.7 \text{ x } 10^{12}\, n^4\, s^{-1}. \tag{2.21}$$

The resulting HWHM of the broadening for the Lyman β, γ and δ lines corresponding to n = 3. 4 and 5, are 0.3, 0.8, and 2.0 mÅ respectively. Since this broadening is small compared to the other broadening mechanisms, we can ignore impact broadening by electrons in the model.

2.2.3 Oscillating Electric Fields (Waves).

We next consider the effect that oscillating electric fields have on an emitting ion.[22] The Hamiltonian for an atom in presence of an oscillatory electric field can be written

$$H = H_o + H', \tag{2.22}$$

where

H_o = the Hamiltonian of the unperturbed H-like atom

$H' = ZeE_0 \cos(\omega t)$, the contribution from a monochromatic oscillatory electric field.

From Schrödinger's equation

$$\Psi \frac{\partial \Psi}{\partial t} = (\hat{H}_0 + eZE_0 \cos(\omega t))\Psi\,. \tag{2.23}$$

We look for a solution of the form

$$\Psi_\gamma = \sum_{n,k} e^{-\gamma t} b_{nk} \Psi_n\,,$$

where

$e^{-\gamma t}$ = the time dependent coefficient
b_{nk} = Fourier coefficients
ψ_n = the hydrogenic wave functions.

Inserting this expression into Eq. (2.23) and using the orthogonality of the hydrogenic wave functions we obtain

$$(\gamma - E_n - k\omega)b_{nk} = V_{nn}\left(b_{n,k-1} + b_{n,k+1}\right), \tag{2.24}$$

where

$$V_{nn} = \langle \psi_n | \frac{ezE_0}{2} | \psi_n \rangle . \tag{2.25}$$

We consider two cases for the solution of this equation. First, if γ is different from E_n, then $(\gamma - E_n)$ will be large compared to the perturbation potentials V_{nn} and $b_{nk} = 0$. When $\gamma = E_n$, the term on the left of Eq. (2.24) will no longer be small compared to the perturbation potentials and

$$-k\omega b_{nk} = V_{nn}\left(b_{n,k-1} + b_{n,k+1}\right). \tag{2.26}$$

The coefficients b_{nk} then satisfy the same recursion relations as for Bessel functions, namely,

$$\frac{2k}{x} J_k(x) = J_{k+1}(x) + J_{k-1}(x), \tag{2.27}$$

so the solution to the problem is given by

$$\gamma_n = E_n, \text{ and } b_{nk} = J_k\left(\frac{2V_{nn}}{\omega}\right), \tag{2.28}$$

with the wave functions becoming

$$\Psi_n = e^{-iE_n t} \sum_{k=-\infty}^{k=\infty} e^{i\omega kt} J_k\left(\frac{2V_{nn}}{\omega}\right)\psi_n . \tag{2.29}$$

The profile of the line is calculated from the wave function by

$$I_{nm} \propto \left| \frac{1}{2\pi\tau} \int_{-\tau/2}^{\tau/2} \exp(-it\Delta\omega)\langle \Psi_n(x,t)|d(x)|\Psi_m(x,t)\rangle dt \right|^2 , \tag{2.30}$$

where $d(x) = e\vec{r}$ is the dipole operator.[5,23] Working out the dipole expression first, we have

$$\langle \Psi_n |d(x)| \Psi_m \rangle = e^{i(E_n - E_m)t} \sum_{k=-\infty}^{k=\infty} J_k\left(\frac{2V_{nn}}{\omega}\right) e^{-i\omega kt} \langle \psi_n |d(x) \cdot$$

$$\cdot \sum_{j=-\infty}^{j=\infty} J_j\left(\frac{2V_{mm}}{\omega}\right) e^{i\omega jt} |\psi_m\rangle . \tag{2.31}$$

Inserting this expression into the integral given by Eq. (2.30) and integrating over all time

$$\lim_{\tau\to\infty} \frac{1}{2\pi\tau} \int_{-\tau/2}^{\tau/2} e^{-it[\Delta\omega - (E_n - E_m + (j-k)\omega)]} \sum_{k=-\infty}^{k=\infty} \sum_{j=-\infty}^{j=\infty} J_k\left(\frac{2V_{nn}}{\omega}\right) J_j\left(\frac{2V_{mm}}{\omega}\right) \langle \psi_n |d(x)| \psi_m \rangle d\tau$$

$$= \frac{1}{2\pi} \sum_{k=-\infty}^{k=\infty} \sum_{j=-\infty}^{j=\infty} J_k\left(\frac{2V_{nn}}{\omega}\right) J_j\left(\frac{2V_{mm}}{\omega}\right) \langle \psi_n |d(x)| \psi_m \rangle \delta\left[\Delta\omega - (E_n - E_m + (j-k)\omega)\right]. \tag{2.32}$$

The line profile is then given by

$$I_{nm} \propto \left| \sum_{k=-\infty}^{k=\infty} \sum_{j=-\infty}^{j=\infty} J_k\left(\frac{2V_{nn}}{\omega}\right) J_j\left(\frac{2V_{mm}}{\omega}\right) \langle \psi_n |d(x)| \psi_m \rangle \right|^2 \delta\left[\Delta\omega - (E_n - E_m + (j-k)\omega)\right]$$

$$= \sum_{k=-\infty}^{k=\infty} \left| \sum_{j=-\infty}^{j=\infty} J_k\left(\frac{2V_{nn}}{\omega}\right) J_j\left(\frac{2V_{mm}}{\omega}\right) \langle \psi_n | d(x) | \psi_m \rangle \right|^2 \delta\left[\Delta\omega - (E_n - E_m + (j-k)\omega)\right]. \quad (2.33)$$

Making the substitution $p = k - j$, the profile can be rewritten

$$I_{nm} \propto \sum_{p=-\infty}^{p=\infty} \left| \sum_{j=-\infty}^{j=\infty} J_{j+p}\left(\frac{2V_{nn}}{\omega}\right) J_j\left(\frac{2V_{mm}}{\omega}\right) \langle \psi_n | d(x) | \psi_m \rangle \right|^2 \delta\left[\Delta\omega - (E_n - E_m - p\omega)\right]. \quad (2.34)$$

Using the following relationship for Bessel functions

$$J_n(x-y) = \sum_{k=-\infty}^{k=\infty} J_{k+n}(x) J_k(y), \text{ for } n = 0, \pm 1, \pm 2, \ldots, \quad (2.35)$$

the integral simplifies to

$$I_{nm}(\Delta\omega) \propto \left| \langle \psi_n | d(x) | \psi_m \rangle \right|^2 \sum_{p=-\infty}^{p=\infty} \left| J_p\left(\frac{2V_{nn}}{\omega} - \frac{2V_{mm}}{\omega}\right) \right|^2 \delta\left[\Delta\omega - (E_n - E_m - p\omega)\right], \quad (2.36)$$

where

$$V_{nn} = \langle \psi_n | \frac{ezE_0}{2} | \psi_n \rangle = \frac{1}{2} \frac{3\hbar E_0}{2Zem_e} n(n_1 - n_2). \quad (2.37)$$

Taking the relative frequency change to $E_m - E_n$, we have the expression for broadening by monochromatic electric fields,

$$I_{nm}(\Delta\omega) \propto \left| \langle \psi_n | d(x) | \psi_m \rangle \right|^2 \sum_{p=-\infty}^{p=\infty} J_p^2(\Delta k \xi E_0) \delta\left[\Delta\omega + p\omega\right], \quad (2.38)$$

where we have defined $\xi = \frac{3\hbar}{2\omega Zem_e}$. This calculation shows that under the action of an oscillating field, a line is split into a large number of satellite lines located at $\Delta\omega = p\omega$, with the amplitude of each satellite given by $J_p^2(\Delta k \xi E_0)$. We refer to $|p|$ as the satellite

number, since $p = 0$ corresponds the center of the line, $p = \pm 1$ to the first satellite located at $\pm\omega$, etc.

2.2.3.1 Superposition of Electric Fields. In the plasma, radiating ions will encounter a large number of waves with random phase. The resulting electric field *E(t)* encountered by the ions will be the sum of all of these waves, that is,

$$E(t) = \sum_{j=1}^{N} E_j \cos(\omega t + \varphi_j). \tag{2.39}$$

We can rewrite *E(t)* in terms of an effective electric field E_0 and phase factor φ as

$$E(t) = E_0 \cos(\omega t + \varphi), \tag{2.40}$$

where

$$E_0 = \left[\left(\sum_{j=1}^{N} E_j \cos\varphi_j \right)^2 + \left(\sum_{j=1}^{N} E_j \sin\varphi_j \right)^2 \right]^{1/2} \tag{2.41}$$

and

$$\tan\varphi = \frac{\sum_{j=1}^{N} E_j \sin\varphi_j}{\sum_{j=1}^{N} E_j \cos\varphi_j}. \tag{2.42}$$

With φ_j distributed uniformly on the interval $(0,2\pi)$, and $N >> 1$, the probability of finding the electric field E_0 will be given by the Rayleigh distribution[24]

$$W(E_o) = \left(\frac{2E_o}{\overline{E_o}^2} \right) e^{-E_0^2 / \overline{E_0}^2} \tag{2.43}$$

where

$$\overline{E}_o = \left(\sum_j E_j^2 \right)^{1/2} . \tag{2.44}$$

In most plasmas, Langmuir oscillations develop anisotropically.[2] With the axial symmetry of the device, it is expected that the value of the electric field parallel to the current $\overline{E}_{0//}$ will be different from the value of the electric field perpendicular to the current $\overline{E}_{o\perp}$. The probability $p(\theta)$ of finding the resulting electric field vector $\vec{E}_0$ in an interval $d\theta$ around θ will then correspond to an ellipsoid given by

$$p(\theta)d\theta \propto \frac{\sqrt{\cos^2\theta + z^4 \sin^2\theta}\sin\theta d\theta}{\left(\cos^2\theta + z^2\sin^2\theta\right)^2}, \tag{2.45}$$

where

$$z = \overline{E}_{o//} \,/\, \overline{E}_{o\perp} = a \,/\, b, \tag{2.46}$$

where a is along the direction of the current, and b is perpendicular to the direction of the current, as illustrated in Figure 2-3. We can then obtain the profile for the ion being subject to a large number of waves with different phase by applying the Rayleigh distribution to Eq. (2.38)

$$\bar{I}_{nm} = < I_{nm} >_{E_0} \propto \left| \langle \psi_n | d(x) | \psi_m \rangle \right|^2 \sum_{p=-\infty}^{p=\infty} \left\langle J_p^2(\xi E_0 \Delta k) \right\rangle_{E_0} \delta[\Delta\omega + p\omega], \tag{2.47}$$

where

$$\left\langle J_p^2(\xi E_0 \Delta k) \right\rangle_{E_0} = \int_0^\infty J_p^2(\xi E_0 \Delta k) \frac{2E_0}{\overline{E}_0^2} e^{-\frac{2E_0^2}{\overline{E}_0^2}} dE_0 . \tag{2.48}$$

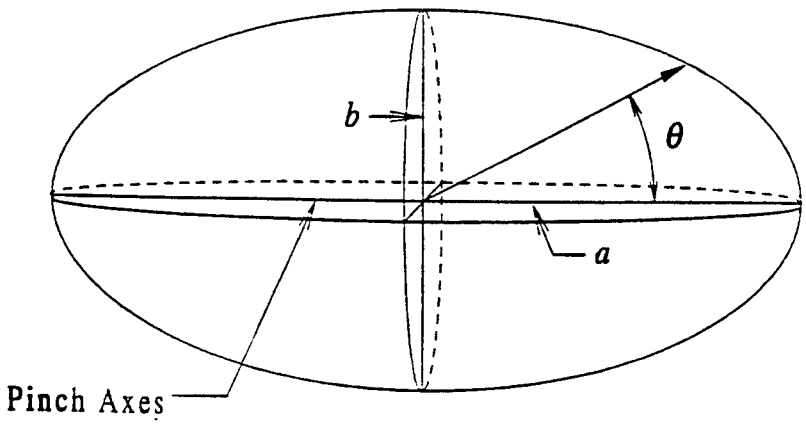

Figure 2-3. Distribution of electric fields.

Letting $x = \xi E_0 \Delta k$ we can write

$$\bar{I}_{nm} = \int_0^\infty J_p^2(x) \frac{2x}{\left(\xi \bar{E}_0 \Delta k\right)^2} e^{-\frac{x^2}{\left(\xi \bar{E}_0 \Delta k\right)^2}} dx$$

$$= \frac{1}{\tilde{\varepsilon}} \int_0^\infty J_p^2(x) e^{-\frac{x^2}{2\tilde{\varepsilon}}} x dx \tag{2.49}$$

$$= I_p(\tilde{\varepsilon}) e^{-\tilde{\varepsilon}}, \tag{2.50}$$

where

$$\tilde{\varepsilon}_k = \frac{\left(\xi \bar{E}_0 \Delta k\right)^2}{2} = \frac{(\varepsilon \Delta k)^2}{2}. \tag{2.51}$$

The parameter ε in the model corresponds to the value of the electric field strength of the waves and is given by

$$\varepsilon = \frac{3\hbar \bar{E}_0}{2em_e \omega_{pe} Z}. \tag{2.52}$$

As discussed in Section 2.1, the source of oscillating electric fields in the Phoenix plasma is assumed to be Langmuir waves, so ω has been replaced by the plasma frequency

$$\omega_{pe} = \sqrt{\frac{4\pi N_e e^2}{m_e}}. \tag{2.53}$$

The line profile for a single plasma frequency corresponding to the plasma wavelength

$$\lambda_p = \frac{{\lambda_0}^2}{2\pi c} \omega_{pe} \tag{2.54}$$

will then be given, apart from the dipole term, by [1]

$$I(\Delta\lambda) = \sum_{p=-\infty}^{p=\infty} I_{|p|}(\tilde{\varepsilon})\, e^{-\tilde{\varepsilon}}\, \delta(\Delta\lambda - p\lambda_p). \tag{2.55}$$

For $\tilde{\varepsilon}_k >> 1$, the envelope of the satellites is Gaussian (Figure 2-4) with a width

$$\Delta\lambda_{HWHM}(\text{cm}) \approx \frac{[\lambda_0(cm)]^2 a_0 e^3 \varepsilon C^{1/2} \Delta k}{2\pi c\hbar^2} \sqrt{4\pi(1.56\cdot 10^{22} cm^{-3}) m_e}\,, \tag{2.56}$$

which when simplified and put in terms of mÅ becomes

$$\Delta\lambda_{HWHM}(m\text{Å}) \approx 3.72\cdot 10^{-7} (\lambda_0(m\text{Å}))^2\, \varepsilon C^{1/2} \Delta k\,. \tag{2.57}$$

For L_β with $\varepsilon C^{1/2}\Delta k = 1$, this results in a HWHM of 13.6 mÅ.

2.2.3.2 Power Spectrum of ω_{pe}. Due to collisional damping and variations in density, there will be a distribution of oscillating electric field frequencies. The model includes this by using a Lorentz distribution for the plasma frequencies, that is,

$$L(\Delta\omega, g) = \frac{g\omega_{pe}}{2\pi} \frac{1}{\Delta\omega^2 + \left(\frac{g\omega_{pe}}{2}\right)^2}, \tag{2.58}$$

where the corresponding HWHM of this distribution is

$$\delta = \frac{g\omega_{pe}}{2} = \frac{g}{2}\sqrt{\frac{4\pi e^2 (1.56\cdot 10^{22} cm^{-3}) C}{m_e}}\,, \tag{2.59}$$

or

$$\delta(rad/s) = 3.5 \text{ x } 10^{15} g\, C^{1/2}\,. \tag{2.60}$$

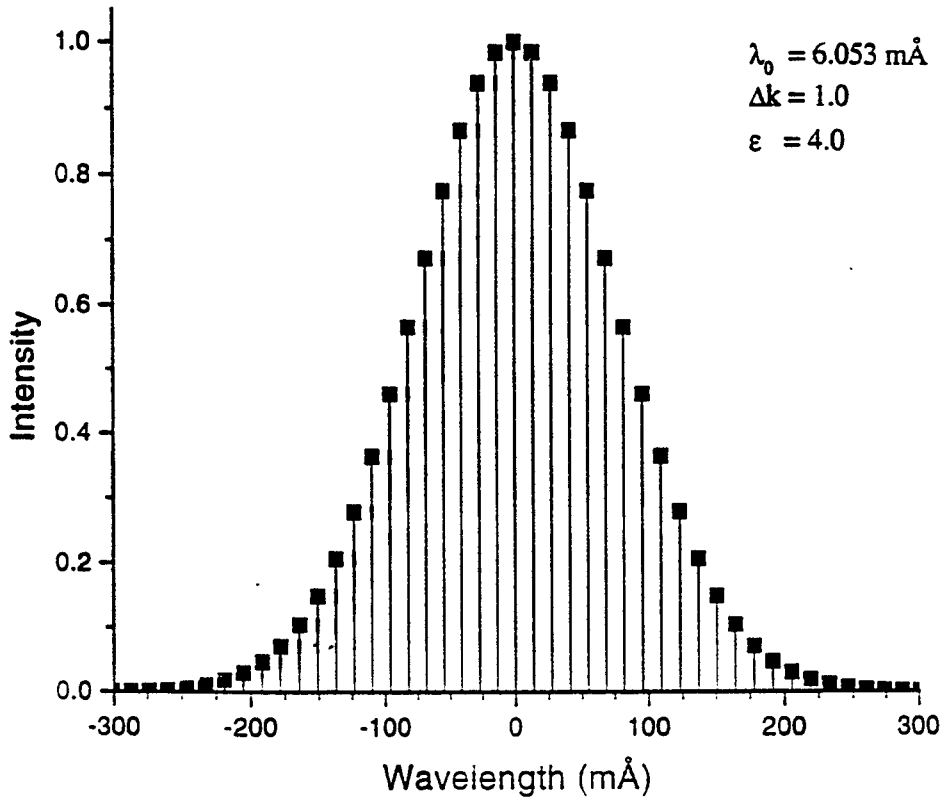

Figure 2-4. Splitting of a line due to an oscillating electric field.

The parameter g characterizes the width of the power spectrum of electric field oscillations.

The line profile due to the oscillating electric fields with this distribution of applied frequencies is

$$I(\Delta\lambda) = \sum_{p=-\infty}^{p=\infty} I_{i,p}(\tilde{\varepsilon}) L(\Delta\lambda - p\lambda_p, |p|g). \tag{2.61}$$

The width of the Lorenz profiles depend upon the satellite number $|p|$. As $|p|$ increases, the width of the Lorentz profiles also increase.

2.2.3 SELF ABSORPTION.

Radiation emitted by ions must make it out of the plasma before it can be detected by a spectrograph. Photons that are emitted by the ion may be absorbed by other ions before they escape the plasma. The newly excited atoms from these photons can re-emit the photon or lose the energy by collisional de-excitation resulting in less photons escaping the plasma than were emitted. Radiation from the line center will most strongly be absorbed, since at line center, where there are many atoms emitting, there are a large number of atoms in the correct state to absorb a photon. As a result, self absorption reduces the line center more than the wings. In the model we use the standard expression for self absorption,[25]

$$I(\Delta\lambda) = \frac{I_{\max}}{t}\left(1 - e^{-\frac{tI_a(\Delta\lambda)}{I_{\max}}}\right), \tag{2.62}$$

where

t = the optical depth of the spectral line at the maximum of the profile $I_a(\Delta\lambda)$.

2.2.4 ZEEMAN BROADENING.

We must also consider the possibility that Zeeman splitting is the principal broadening mechanism in the plasma.[10-12] The difference in the Zeeman splitting of the levels could explain the line dependent differences in the observed profiles. We consider this possibility by determining the magnetic fields required to produce broadening on the order of the observed lines.

For strong fields, the change in frequency associated with the Zeeman splitting of an atomic level will be given by

$$\Delta\omega \cong \frac{\mu_b B(T)}{\hbar}, \tag{2.63}$$

which corresponds to a change in wavelength of[14]

$$\Delta\lambda(m) = \frac{\lambda_0^2}{2\pi c}\Delta\omega = \frac{\lambda_0^2 \mu_b B(T)}{2\pi c\hbar}. \tag{2.64}$$

Inserting the appropriate constants and converting to Gaussian units we arrive at an expression for the shift in wavelength of a line for a given wavelength λ_0 and magnetic field B, namely,

$$\Delta\lambda(\text{mÅ}) \cong 4.63 \times 10^{-10} \left[\lambda_0(\text{Å})\right]^2 B(G). \tag{2.65}$$

To produce the width of the observed profiles for the Lyman series, which are on the order of 30 mÅ, a magnetic field of 2.0 gigagauss (GG) would be required. This would result in a ratio of the magnetic to kinetic energy density of 100 for a plasma temperature of $T \approx 1$ keV. From the best available models of z-pinches, this ratio will rarely exceed unity. Physically, the current tends to filament around the pinch resulting in low magnetic fields inside the pinch. Zeeman splitting cannot be the principle broadening mechanism for the profiles.

2.3. COMPLETE LINESHAPE FOR THE PHOENIX PLASMA SOURCE.

The spectral profile for the Phoenix plasma source without self absorption is calculated by convoluting the Doppler profile Eq. (2.5), the Holtzmark profile Eq. (2.14), and the oscillating electric field profile Eq. (2.61). By using the results of the convolution of a Doppler, Holtzmark, and Lorentzian profile, as derived in Appendix A,

$$D(\Delta\lambda, \alpha, \beta, \delta) = \frac{\beta^2}{\pi} \int_0^\infty y e^{-y^{3/2} - \left(\frac{\beta y}{2\alpha}\right)^2 - y\beta\delta} \left[\Delta\lambda \sin(\beta\Delta\lambda y) + \delta\cos(\beta\Delta\lambda y) + \frac{\beta y}{2\alpha^2}\cos(\beta\Delta\lambda y)\right] dy, \tag{2.66}$$

the profile for each Stark component without self absorption will be given by

$$I(\Delta\lambda) = \sum_{p=-\infty}^{\infty} I_{|p|} e^{-\tilde{\varepsilon}} D\left(\Delta\lambda - p\lambda_p, \alpha, \beta, |p|g\right). \tag{2.67}$$

The final profile is calculated by summing up the profiles for each Stark component and applying the expression for self absorption.

2.4. SUMMARY OF PLASMA PARAMETERS.

We have presented here a model which attempts to take into account all of the broadening mechanisms present in dense plasmas, such as produced on the Phoenix device. The parameters introduced for the model are: *b, C, z,* ε, *g* and *t*. Each parameter gives some information about the plasma.

The parameter *b* is a measure of the velocity of the bulk motion of the plasma. It will make its main contribution in the center of the line. For the central component of L_γ and L_ε it will be the only broadening mechanism.

The parameter *C* is a measure of the density of the plasma. This parameter effects the line shape through all forms of Stark broadening. The Stark broadening by ions will make large contributions to the wings of the line since the Holtzmark profiles fall off slower than Gauss and Lorentz profiles. *C* also determines the frequency of the oscillating electric fields through the plasma frequency and *C* makes a small contribution the width of the envelope of the oscillating electric field profile.

The parameter *z* is a measure of the degree of anisotropy of the oscillating electric fields. A value of $z = 1$ corresponds an equal probability of finding the direction of propagation in all directions. For $z > 1$, the probability of finding the propagation along the pinch axis is higher than perpendicular to the pinch axis.

The parameter ε measures the magnitude of the oscillating electric fields. This field strength variable determines the width of envelope of the satellite lines under the action oscillating electric fields.

The parameter g is a measure of the width of the power spectrum of the oscillations in the plasma. Since the frequency of the oscillations depends on density, this value also gives some measure of density fluctuations.

And finally, the parameter t is the optical depth at the center of the line profiles. This is a measure of the absorption of the radiation before it makes it out of the plasma.

SECTION 3
EXPERIMENTAL APPARATUS

3.1 PHOENIX DEVICE.

Phoenix PRS is a pulsed power z-pinch device used for producing radiation in the soft x-ray region. A diagram of the machine is shown in Figure 3-1. The two primary components of the machine are the pulser and the load. The pulser generates a fast rise time power pulse to deliver to the load, which typically consists of a wire array or a gas puffed into the apparatus.

The schematic circuit diagrams of the Phoenix machine are shown in Figure 3-2.[26] The analysis of the power flow in this device is quite complex. To simplify the problem, the machine is often modeled in terms of an equivalent circuit as in Figure 3-3. By knowing how the machine couples to the load, the reflected power from the load can be minimized for optimal performance. For the data in this dissertation, the load consisted of sixteen 2 cm aluminum wires, 0.8 mil in diameter, arranged in a circular array of diameter 2.6 cm (Figure 3-4). The machine typically delivers a current of 4 Ma to the load and produces 10-50 kJ of energy in the Lyman radiation of aluminum in this configuration.

3.2 DIAGNOSTICS.

The diagnostics used to study the plasma produced by Phoenix were a PIN diode detector, a diamond PCD, a flat crystal spectrometer, a pinhole camera and two bent

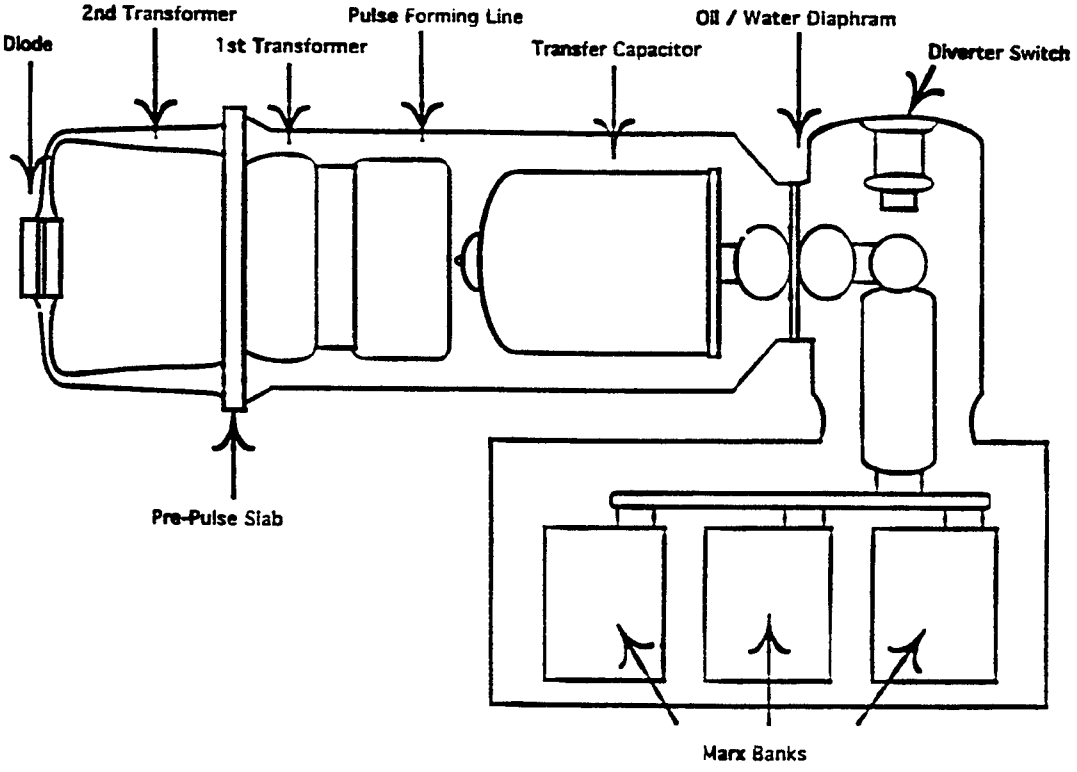

Figure 3-1. Phoenix advanced radiation source.

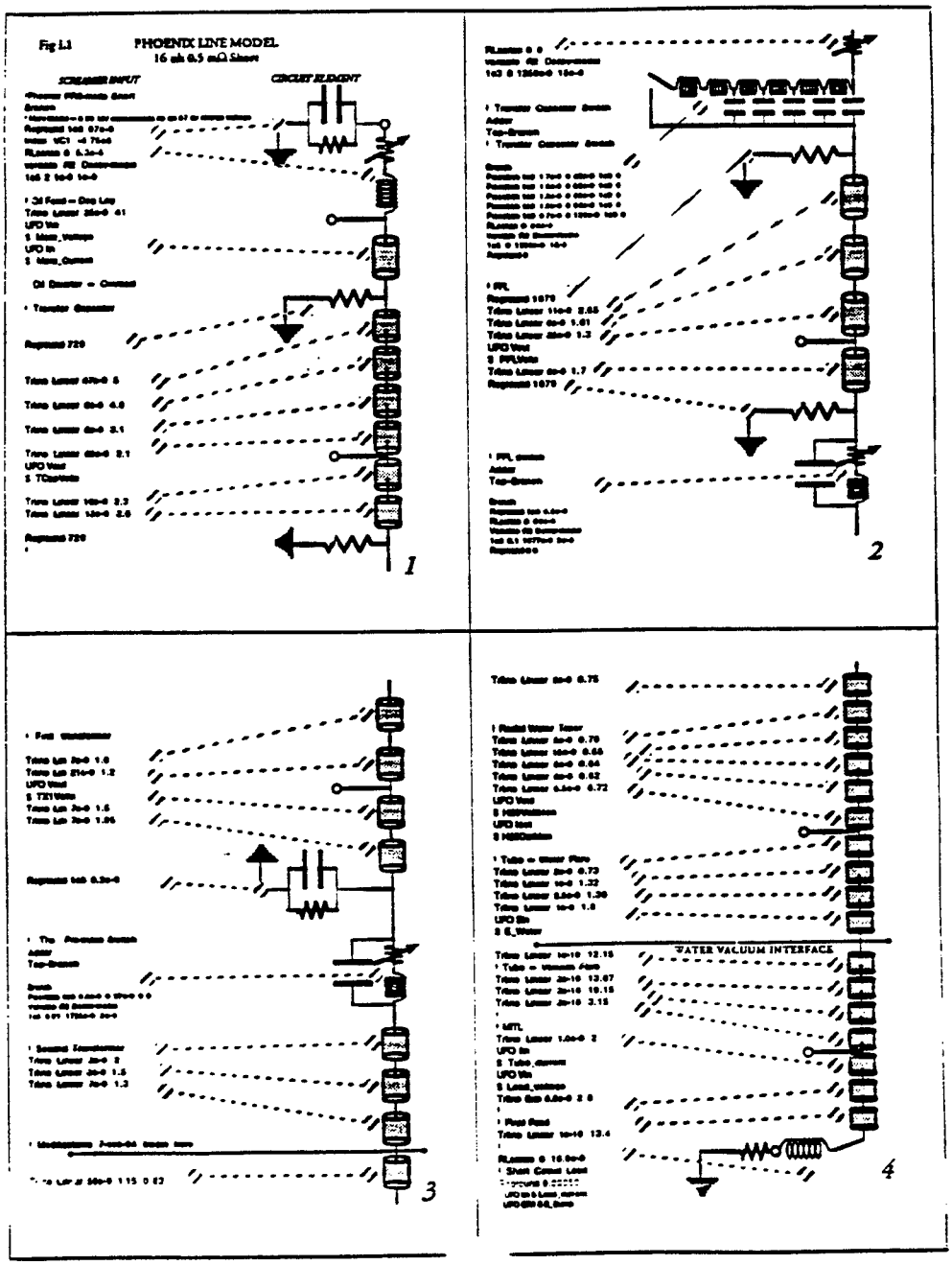

Figure 3-2. Schematic diagram of the Phoenix pulsed radiation source.

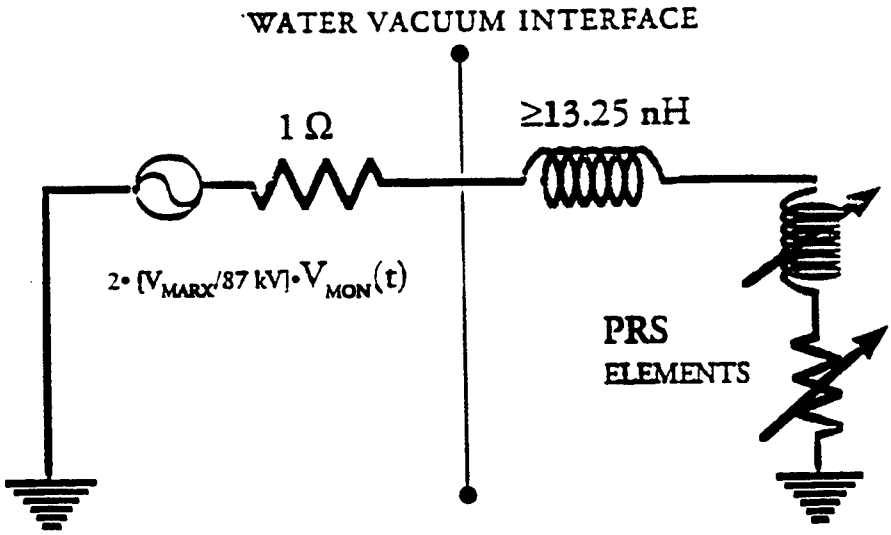

Firuge 3-3. Equivalent circuit for the Phoenix pulsed radiation source.

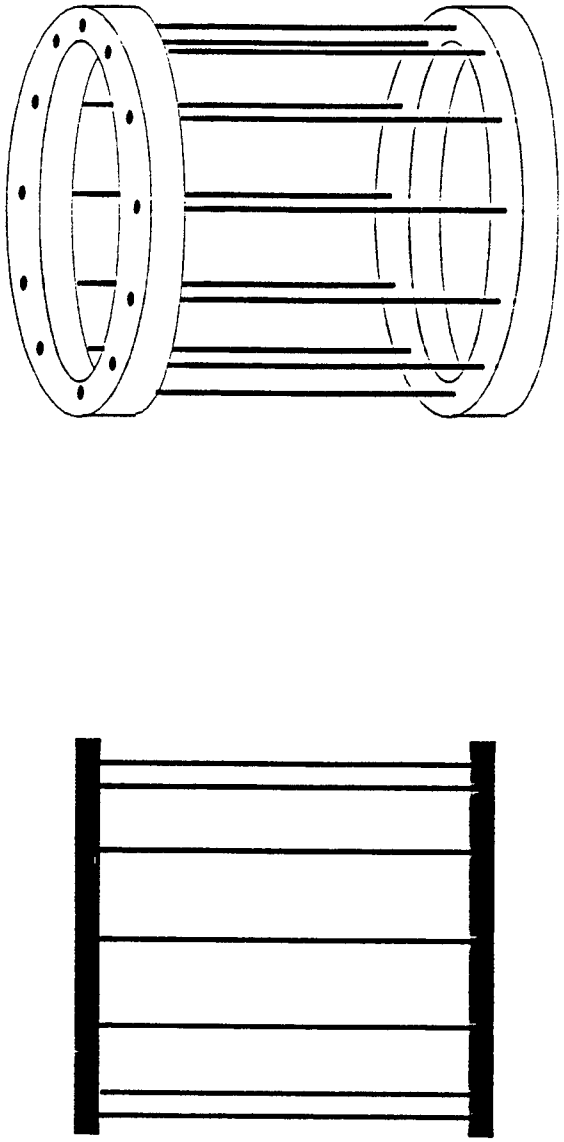

Figure 3-4. Aluminum wire load.

crystal spectrographs of the Johann type. The location of the diagnostics on the Phoenix spool are shown in Figure 3-5.

3.2.1 X Ray Detectors.

The radiation pulse from the Phoenix device was monitored using a diamond photoconductive detector (PCD) and a Quantrad PIN diode. The detectors give the intensity of the radiation as a function of time for the radiation event. The total energy can be obtained from the integration of the signals obtained from these devices. The diamond PCD consists of a thin diamond crystal and the PIN diode consists of an ultra high purity silicon (nearly Intrinsic) wafer, with one side doped with a P-layer and the other side doped with an N-layer leading to the so called PIN diode structure. Both detectors are operated by applying a bias voltage across the active material. When an x ray undergoes a collision with an electron, an electron-hole pair is created, and the electrons resulting from these collisions are swept out by the bias voltage. The PIN diode is operated with a negative bias voltage and has a sensitivity about 1000 times greater than the diamond PCD.

The response curves for these devices are shown in Figure 3-6. The response curve of the diamond PCD was provided by the manufacturer at Los Alamos National Laboratory. The response curve for the PIN diode was calculated using a formula supplied by the manufacturer (Quantrad).

Since we are interested in the most energetic x rays, corresponding to the highest ionization state of the atoms, filters were placed in front of the detectors to strongly

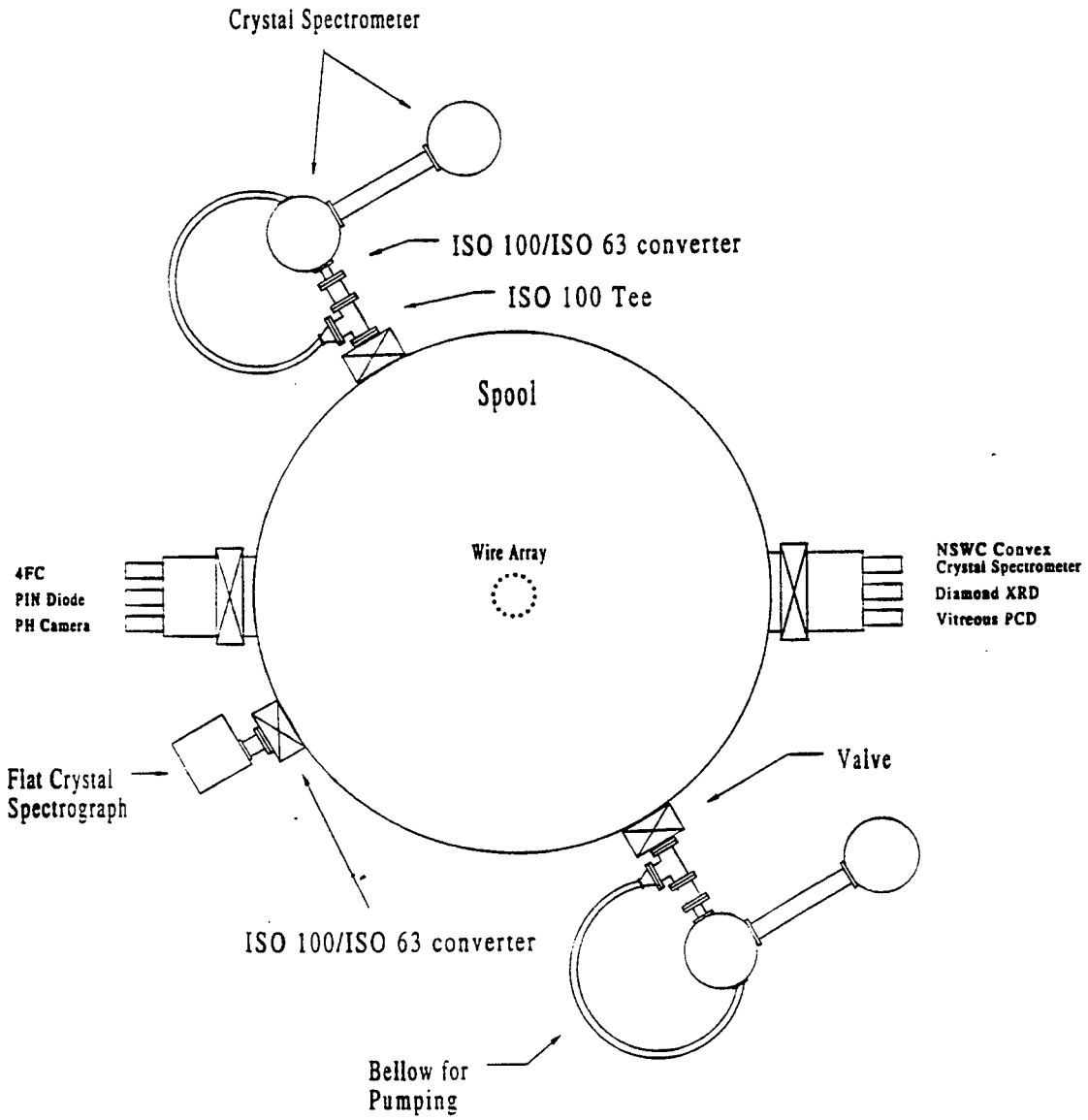

Figure 3-5. Location of diagnostics on the spool.

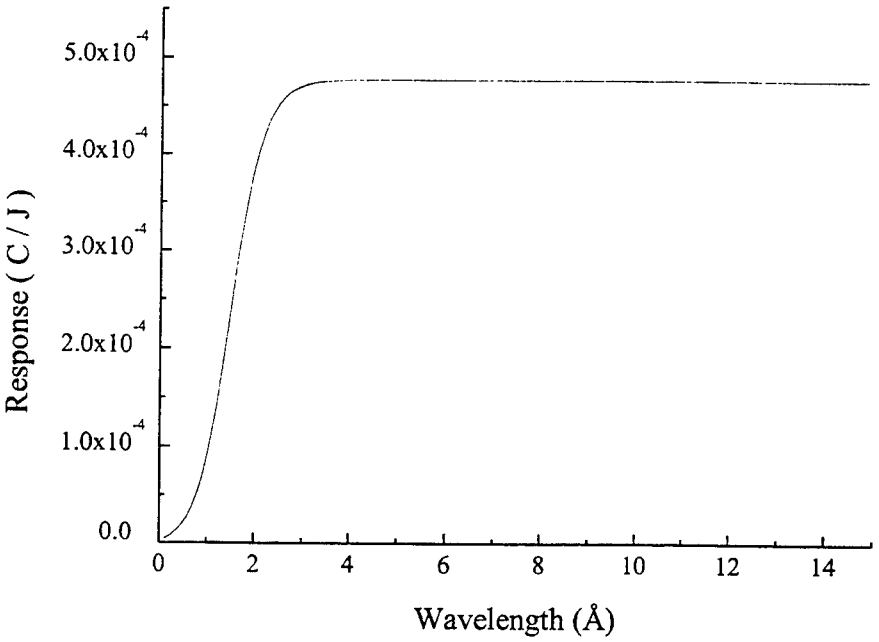

(a) Response of the diamond PCD detector

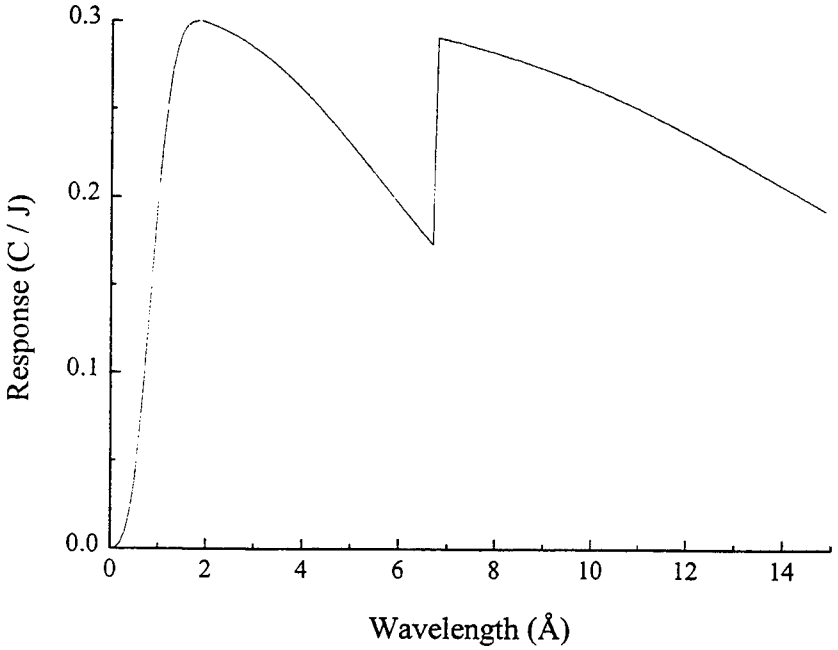

(b) Response of the PIN diode detector

Figure 3-6. Response curves for the diamond PCD detector and the PIN diode detector.

attenuate the longer wavelengths. The filters also served to prevent debris from damaging the detectors and to prevent the detectors from becoming saturated. The filters used with the diamond PCD detector were 0.3 mil Kapton, 0.16 mil Kimfoil, and 3000 Å aluminum. A 400 μ m diameter pinhole in a 2-mil stainless steel substrate was used with the PIN diode to prevent the detector from becoming saturated. The pinhole was mounted in a 2 mm diameter hole placed on a 8 mm thick brass disk and covered with a 5-mil Be foil as shown in Figure 3-7.

The absorption curves for the filters used in the detectors are shown in Figure 3-8. The mass absorption coefficients for the filters were computed using the empirical formula given by Victoreen

$$\frac{\mu}{\rho} = C\lambda^3 - D\lambda^4 + \frac{\sigma_{K-N} NZ}{A} \tag{3.1}$$

with λ the wavelength, σ_{K-N} the Klein-Nishina cross section, N Avogadros number, Z the atomic number, and A the atomic Weight.[27] The Klein-Nishina cross section is given by

$$\sigma_{K-N} = 2\pi \frac{e^4}{m^2 c^4}\left[\frac{1+\alpha}{\alpha^2}\left\{\frac{2(1+\alpha)}{2\alpha+1} - \frac{1}{\alpha}\ln(1+2\alpha)\right\} + \frac{1}{2\alpha}\ln(1+2\alpha) - \frac{1+3\alpha}{(1+2\alpha)^2}\right], \tag{3.2}$$

where $\alpha = h\nu/mc^2$. Since the actual measured values of the mass absorption coefficients are intermittent in the wavelength regions of interest, between 5 Å and 20 Å, it was necessary to use the empirical formula given by Eq. (3.1). The measured absorption coefficients were fit to find C and D.[28] Since the absorption coefficients change

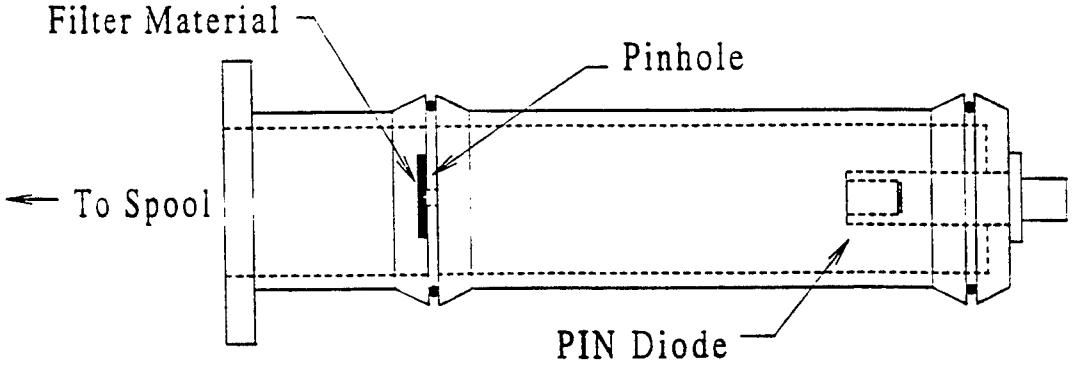

(a) PIN diode detector.

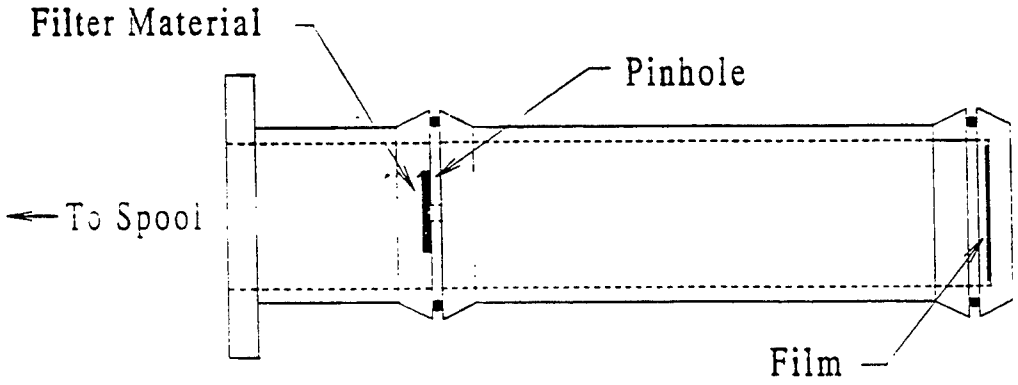

(b) Pinhole camera.

Figure 3-7. Arrangement for PIN diode and pinhole camera.

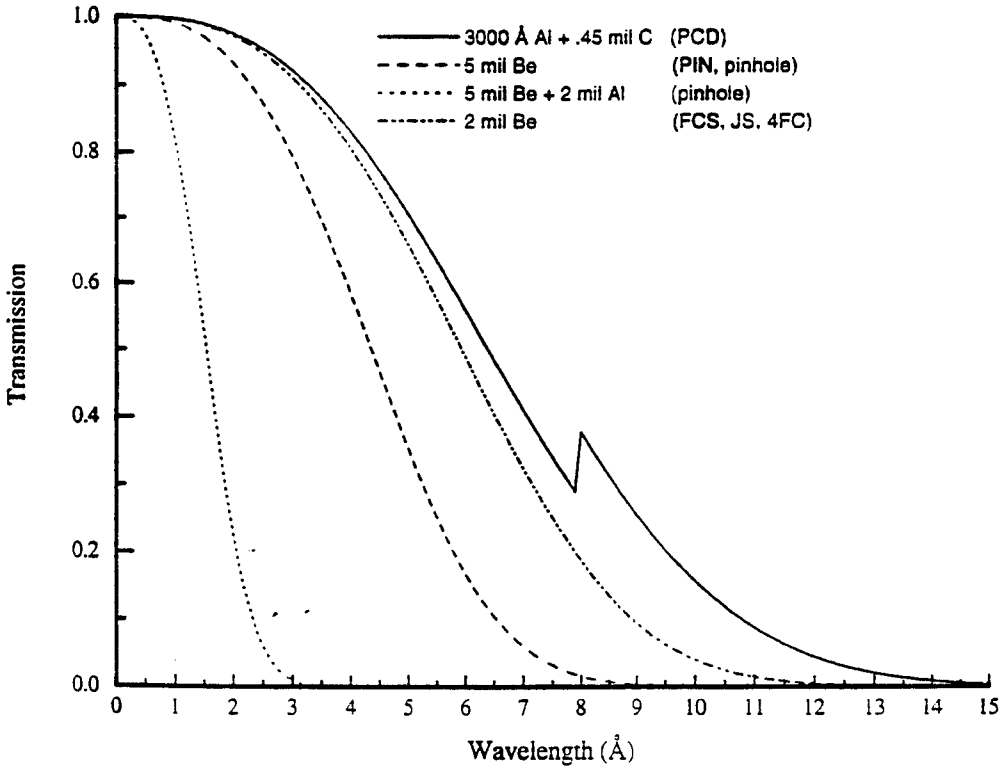

Figure 3-8. X ray absorption curves.

abruptly at the absorption edges of the atom, different values for C and D were computed for the different regions of the spectrum. The total response of the detectors was computed from the product of the response of the detectors with their filters as shown in Figure 3-9. The respective distances of the Diamond PCD and the PIN Diode from the wire array were 2.92 m, and 1.69 m.

3.2.2 Pinhole Camera.

A pinhole camera as shown in Figure 3-7 was utilized to get time integrated images of the x rays emitted from the plasma. The pinhole pictures measure the spatial distribution of the x-ray intensity in the source. Two configurations of the camera were used, but for both configurations the distance from the source to the pinhole was 169 cm. For shots 1118-1125, the film was placed 50 cm from a 400 μm pinhole resulting in a magnification of 0.3. The filters used for this set of shots consisted of 2 mil Al with 5 mil Be. For shots 1126-1129, the film was placed 69 cm from a 25 μm pinhole resulting in a magnification of 0.4. The filters for these shots consisted only of 5 mil Be. KodakBiomax MR film was used because of its high sensitivity and clear background emulsion. The absorption curves for the pinhole filters are given in Figure 3-8.

3.2.3 Four Frame Camera.

A four frame camera was used to determine the size of the pinch events and to observe the temporal evolution of the plasma. Time resolved imaging is necessary to determine the minimum plasma column size, since in time integrated imaging the final size of the pinch is masked by images from other parts of the plasma at other times. The major

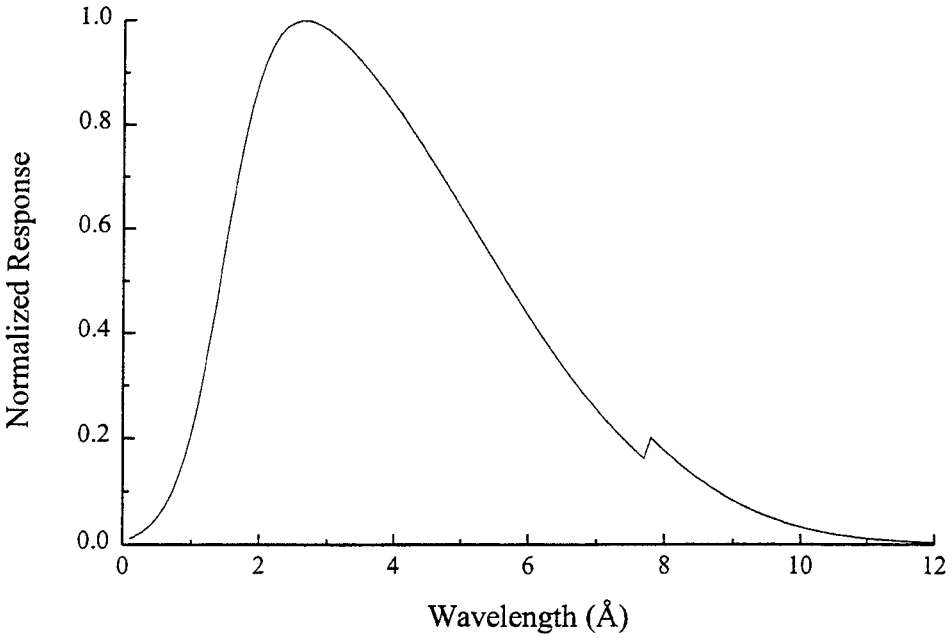

(a) Diamond PCD response with 2 mil Kapton and 3000 Å Al.

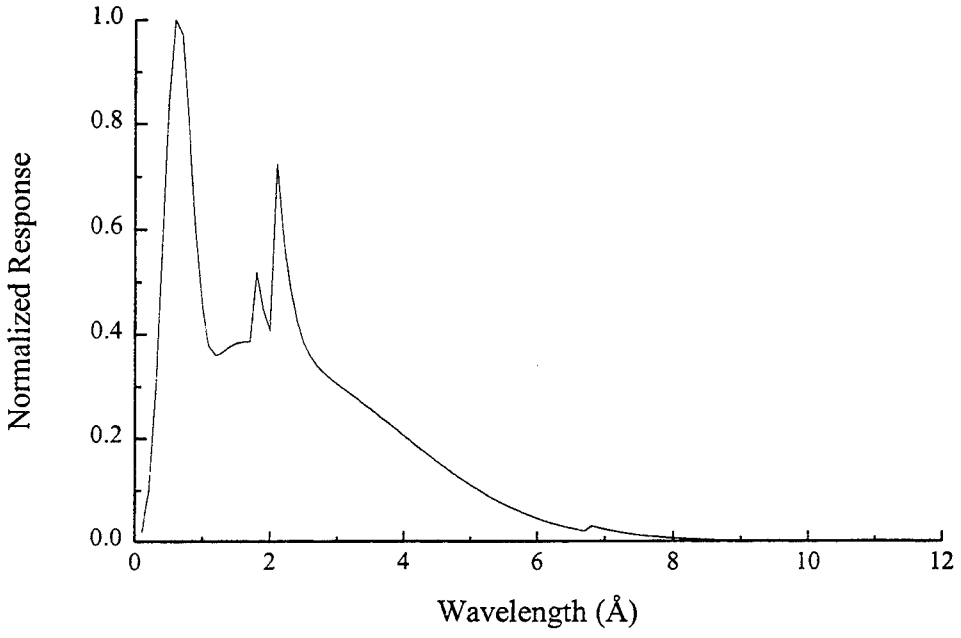

(b) PIN diode response with 5 mil Be.

Figure 3-9. Comparison of PCD detector response curve versus PIN diode.

components of the four frame camera are an MCP, a phosphor screen, and a fiber optic array as illustrated in Figure 3-10.[29] The MCP consists of 10-100 μm diameter glass capillary tubes stacked side to side. When a voltage is applied across the ends of the tubes, the tubes perform as do photomultiplier tubes, shown in Figure 3-10. The resulting cascade of electrons impact a phosphor screen where they cause the phosphor to emit photons in the visible region of the spectrum. Since the lifetime of the phosphor is long, typically 40-80 ns, an image can be obtained on standard film.

The "on/off" state of the MCP is controlled by the voltage applied across it. If a voltage pulse is applied to the MCP, the camera is ON only for the duration of this pulse, since the gain of the device is negligible when no voltage is applied, and it is approximately 10^6 when the optimal voltage is applied. In the 4FC the MPC is cut into four sections which are electrically isolated from one another allowing the four sections of the camera to operated individually as shown in Figure 3-11. Applying short voltage pulses, typically 1 to 10 ns, to each section of the camera sets the exposure time for each frame. The pulses sent to each section of the camera are delayed by 1 to 30 ns between frames resulting in framing of the camera. For the experiments performed at Phoenix, the frames were opened for 5 ns with a 5 ns delay between frames.

Figure 3-11 shows the setup used to image a plasma with the 4FC. Pinholes are placed in front of each section of the 4FC to produce images on the corresponding sections of the MCP. For the experiment, the distance from the pinhole to the source was 170 cm and the distance from the pinhole to the film was 22 cm, resulting in a

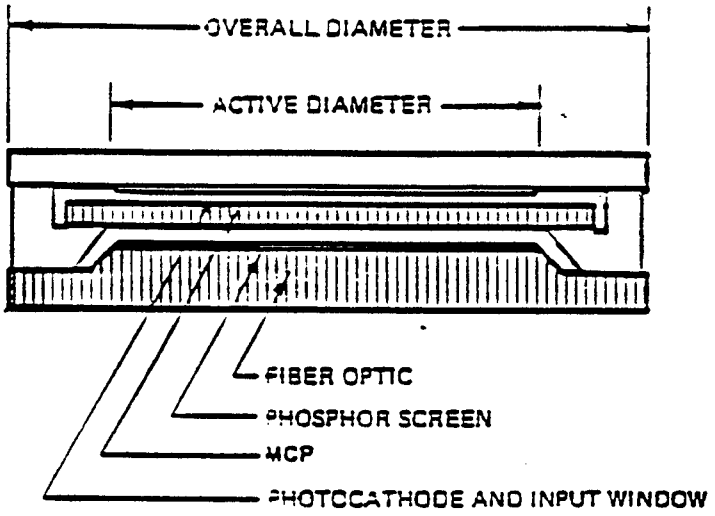

(a) Side view of an MCP.

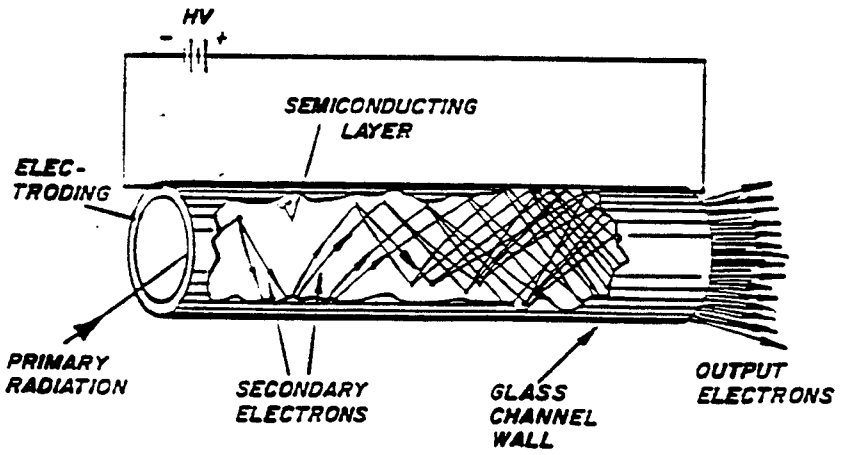

(b) Capillary tube of an MCP showing cascading electrons.

Figure 3-10. Details of an MCP.

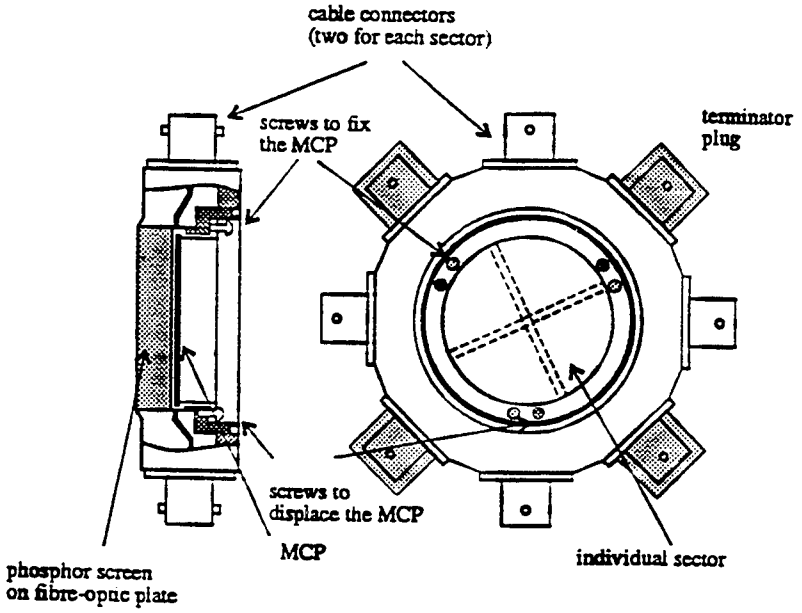

(a) Four frame camera schematic.

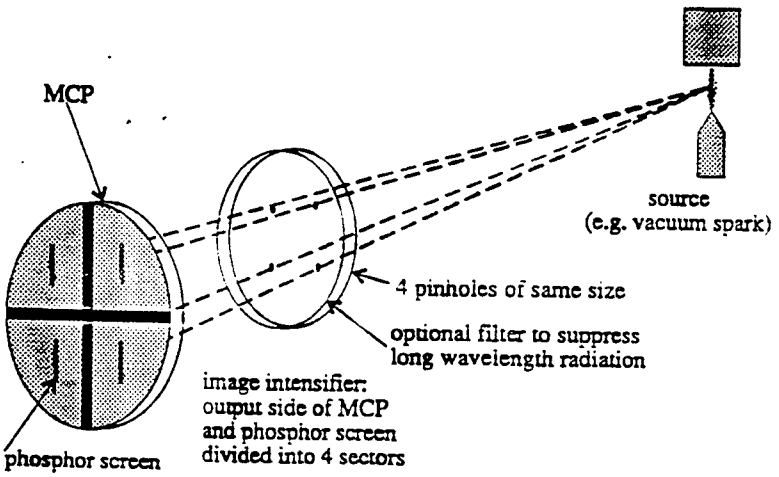

(b) Pinhole configuration for 4FC.

Figure 3-11. Details of four frame camera.

magnification of 0.13. Pinholes of 100 μm and 400 μm were used to ensure that enough intensity was reaching the camera in the short time that the cameras were on. With such large pinholes compared to the wavelength, the resolution of the camera was limited by the size of the pinholes.

An important aspect to the operation of the 4FC is the timing of the camera. Ideally the camera should start framing just before the pinch event occurs so that the formation of the pinch can be observed. Figure 3-12 shows the timing scheme used to open the camera at the correct time. The timing begins when a signal from a V-dot probe, a voltage monitor which detects the pulse in the machine 250 ns prior to the pinch, triggers the delay generator. The delay generator delays the pulse about 200 ns and triggers the four frame camera pulser. The pulser sends high voltage pulses to the four frames of the camera with respective delays to each frame. The pulse returning from the first frame is then sent to the control room. The radiation from the machine is monitored using the PIN diode, described in Section 3.2.1, and this signal is correlated to the pulse which returned from the 4FC. Adjustments of relative timing are made using a Stanford Research Systems model DG535 delay generator to allow for proper placement of the 4FC triggering in the radiation pulse.

3.2.4 Spectrographs.

3.2.4.1 Flat Crystal Spectrograph. The flat crystal spectrograph was employed to look at lines in the Lyman series of Al XIII. In particular the spectrograph was designed to detect the L_γ, L_δ and L_ε lines. The data obtained from this spectrometer was used to

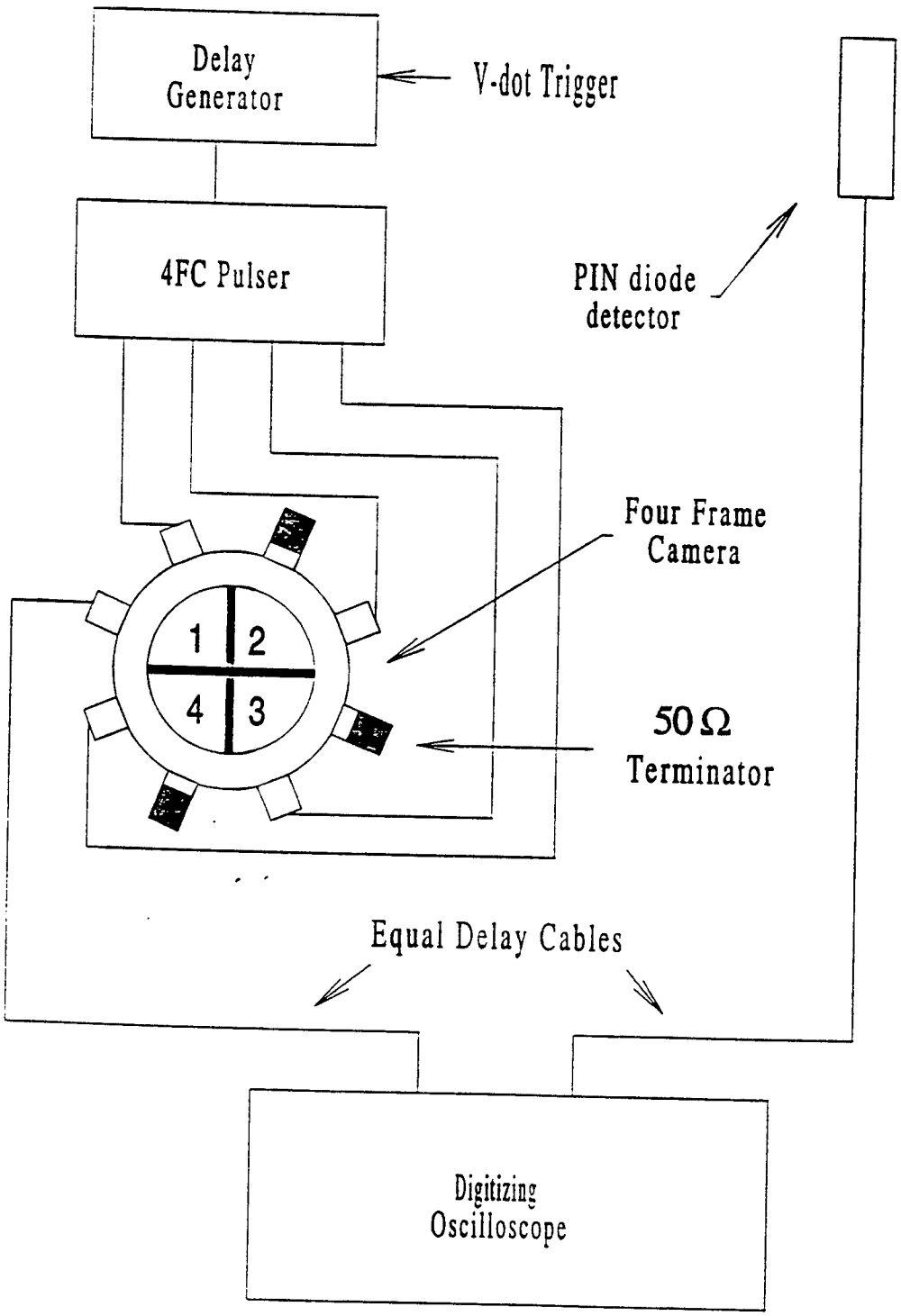

Figure 3-12. Four Frame Camera Timing.

check the results of the bent crystal spectrographs and give additional information about parameters in the plasma. The Auburn flat crystal spectrometer shown in Figure 3-13(a) uses two flat crystals instead of one, since it is a modification of a previous diagnostic. Two Quartz $10\underline{1}0$ crystals of 3.12 cm were used in the Auburn spectrograph. The crystals were set for an angle of $\alpha \approx 42.5^{\circ}$. The source to crystal distance was U = 100 cm and the crystal to film distance was V = 10 cm. This configuration results in a detectable wavelength region of 5.61 Å to 5.89 Å which encompasses the L_{γ}, L_{δ}, and L_{ε} lines having central wavelengths of 5.739 Å, 5.605 Å, and 5.534 Å respectively. From geometrical considerations, the wavelength as a function of position was calculated for the spectrograph (Appendix B). The dispersion is linear for these spectrograph parameters and the value of the dispersion calculated was 5.8 mÅ/mm. The angle α could be set for each shot to within 0.5°, however, vibrations in the machine contributed to fluctuations in α from shot to shot. A more accurate value of α was later calculated from the spectra using the relative positions of two known lines. A 5 cm long, 1 mm wide slit was placed between the source and crystal located 12 cm from the crystal. The slit was oriented along the direction of dispersion of the crystal as shown in Figure 3-13. A 2-mil Be foil was placed over the slit to filter out longer wavelengths and prevent saturation of the film.

The resolution of flat crystal spectrometers is generally limited by the quality of the crystal used and the spatial extension of the source.[30,31] The quality of the crystal affects

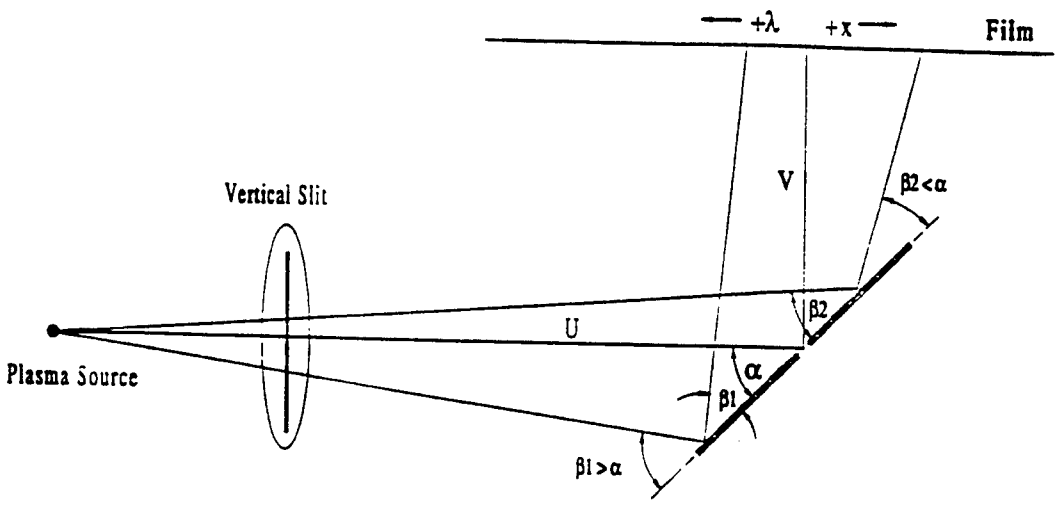

(a) Auburn flat crystal spectrometer.

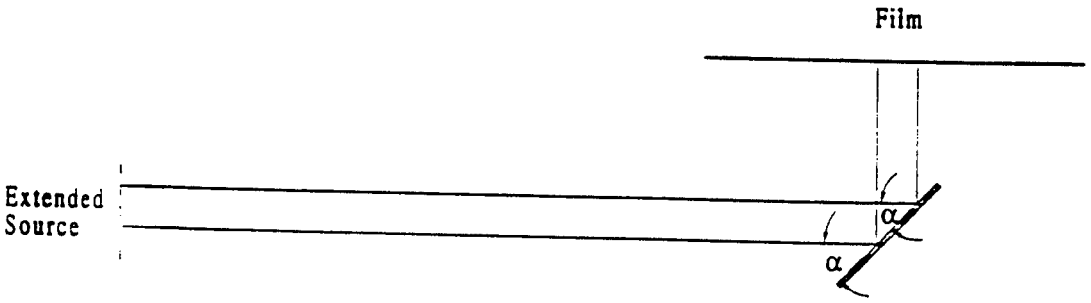

(b) Instrumental broadening due to geometry.

Figure 3-13. Schematic of flat crystal spectrometer.

the resolution through the variation of the 2d spacing in the crystal and through the surface structure. The 2d value for real crystals will vary slightly due to imperfections in the crystals. This variation of the 2d value broadens the spectra on the detector. Using the resolving power for quartz $10\underline{1}0$ of $\lambda / \Delta\lambda = 7.54 \times 10^3$, the resulting resolution is 2 mÅ for the Auburn flat crystal spectrograph. The effect of the spatial distribution of the source on the resolution arises from the geometry of the spectrograph. For a flat crystal spectrograph this broadening can be quite large depending upon the size of the source. This is illustrated in Figure 3-13. We consider two points in the source separated by a distance *h* in the direction of dispersion of the crystal, and we look at two parallel rays from different parts of the source that have the same wavelength and satisfy the Bragg angle α. The rays from these two points with the same wavelengths will strike different places on the film. This results in the broadening of the line. There are a number of ways for two rays of the same wavelength from different parts of the plasma to strike the crystal at the same Bragg angle. The sum of these effects can be calculated using ray tracing. The geometry of the Auburn flat crystal spectrometer gives a displacement of 1 mm on the film when there is a displacement of 1 mm in the source. From the previously calculated dispersion of 5.8 mÅ/mm, this means that for every mm that the source is extended along the direction of dispersion of the crystals, the line is broadened by 5.8 mÅ. For this reason the spectrograph was oriented so that the smaller dimension of the plasma was along the dispersion direction of the crystals. As we will see in the

next section, curved crystal spectrometers in the Johann configuration do not always have a large broadening due to the geometry.

3.2.4.2 Bent Crystal Spectrographs. The primary diagnostics used for measuring the polarization lineshapes in the plasma were two bent crystal spectrometers mounted in the Johann configuration (Figure D-1). These two spectrometers were used to obtain high resolution line profiles of the L_β and L_γ lines of Al XIII in two states of polarization. On each shot both spectrometers monitored the same line, either L_β or L_γ.

Both Johann spectrographs used a quartz $10\underline{1}0$ crystal bent to a radius of curvature of 1-m. A 5 cm long, 1 mm wide slit was placed between the source and crystal, 11 cm from the crystal. The slit was oriented parallel to the plane of the spectrograph and a 2-mil Be filter (Figure 3-8) was placed over the slit.

The crystals were oriented so that the plane of polarization of one of the spectrometers was parallel to the bulk current in the plasma, and the plane of polarization of the other was perpendicular to the bulk current in the plasma as illustrated in Figure 3-14. The details of how x rays are polarized by crystals under Bragg reflection are given in Appendix C. The difference in these two configurations results in one crystal being illuminated by a point source along the dispersion of the crystal and the other being illuminated by a line source. To see how the orientation of the source would affect the observed profiles, we performed ray tracing for the Johann spectrometers. The details of the ray tracing calculations for the Johann spectrometers is given in Appendix D.

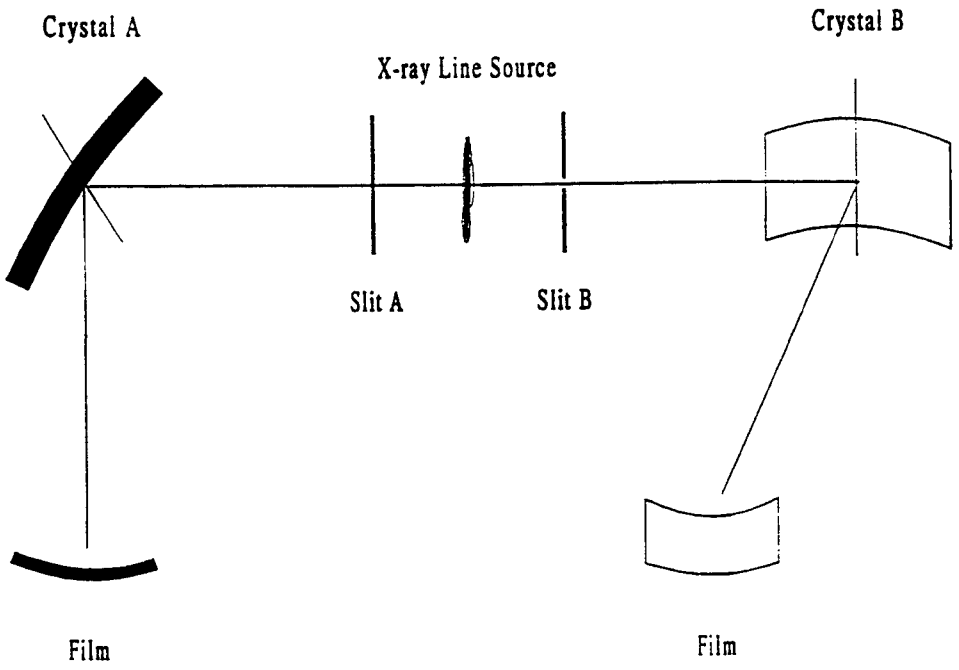

Figure 3-14. Orientation of Johann spectrographs.

3.2.4.2.1 Ray Tracing Results for the Bent Crystal Spectrographs. For the ray tracing calculations, the source to crystal distances tested were 1.5 m and 3.0 m. These two distances were chosen based upon required intensities at the film, and this was done for two crystal lengths of 2.5 cm and 7.5 cm. The input sources for the calculations were a point source and a 2 cm long line source. Ray tracing was performed for wavelengths of interest for the Phoenix experiments of 6.053 Å and 5.739 Å corresponding to the L_β and L_γ lines of Al XIII. Gaussian profiles with constant radiance centered at these wavelengths were input with different half widths for the sources to test the limitations of the spectrographs in various configurations. For a well designed spectrograph, the output spectra should reconstruct the profile in the source.

Before ray tracing was performed using Gaussian profiles in the source, the resolution and detectable wavelength of the test configurations were found. The resolution determines the minimum difference in wavelength that can be resolved by the spectrometer and the detectable wavelength region determines the maximum width of lines that can be observed.

The resolution of the spectrographs for the sources are determined by ray tracing a single wavelength for every point in the source.[31] By putting in an infinitely narrow line at a single wavelength and observing the width of the output line we determined the broadening due to the instrument. The results of these calculations for the L_β and L_γ lines of Al XIII are shown in Figure 3-15. The resolving power for the point source,

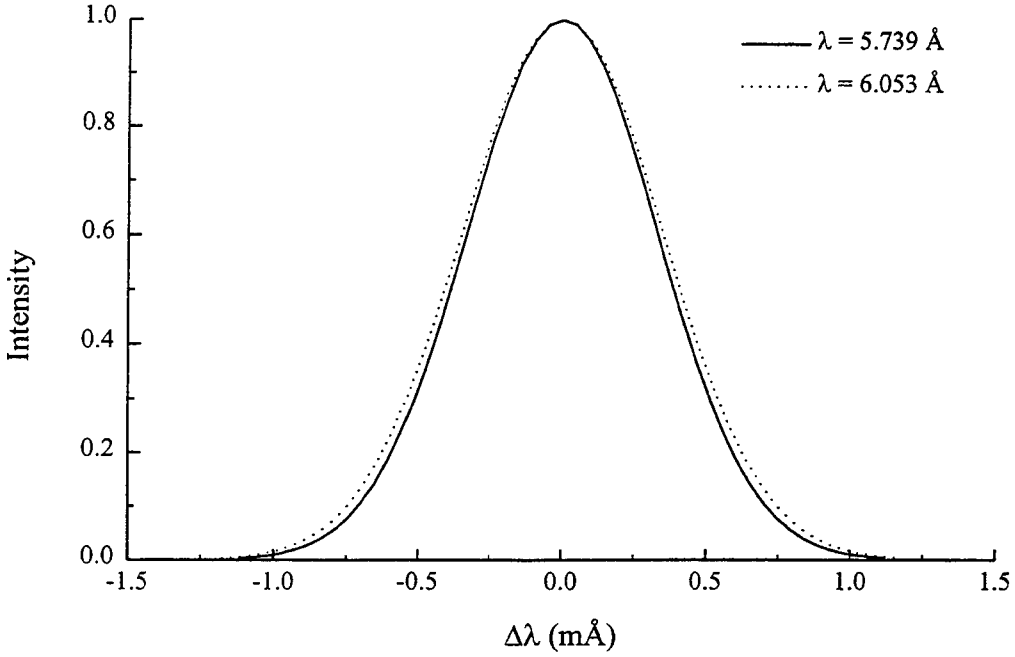

(a) Resolving power for a point source

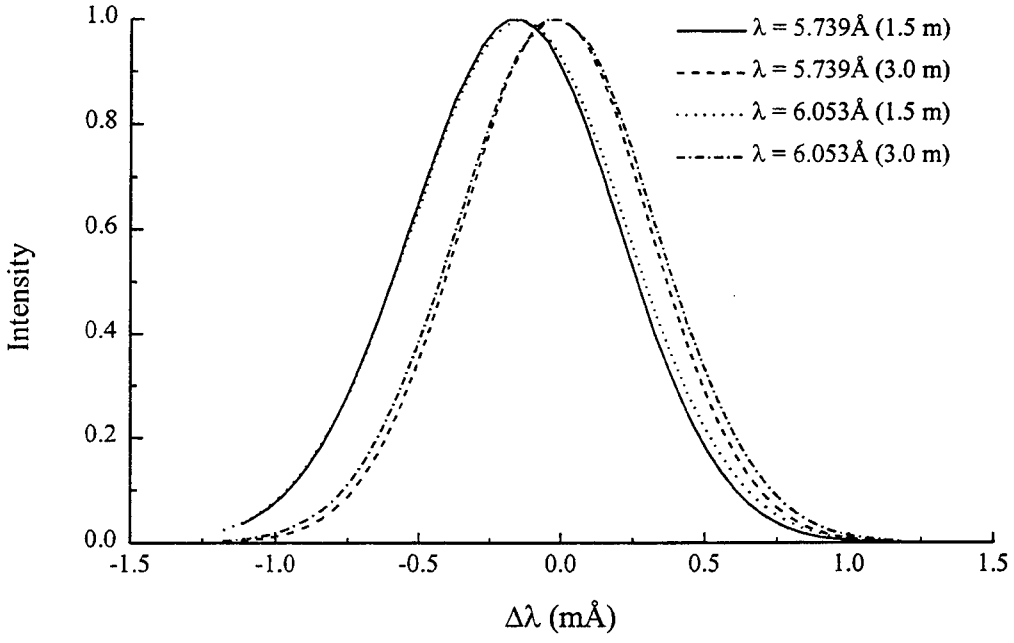

(b) 2 cm line source

Figure 3-15. Intensity versus wavelength for point and extended sources

shown in Figure 3-15, obtained from this ray tracing technique is approximately 0.82 mÅ for L_β and 0.77 mÅ for L_γ, independent of the source to crystal distance. For the line source, the resolution depends on both the wavelength and distance of the crystal from the source as shown in Figure 3-15. For L_β, the resolving power for the line source is approximately 0.89 mÅ at a distance of 1.5 m and 0.82 mÅ at 3.0 m. For L_γ, the resolving power for the line source is approximately 0.86 mÅ at 1.5 m and 0.78 mÅ at 3.0 m. In the Johann configuration, the primary factors effecting the resolution are the diameter of the Rowland circle and the quality of the crystal.

The detectable wavelength region of the spectrographs were found by calculating the angle that the rays from the source points make with the ends of the crystal and then converting these angles to wavelength through Bragg's law. The detectable wavelength regions for the L_β and L_γ lines for three points on a line source are plotted for crystal lengths of 2.5 cm in Figure 3-16 and 7.5 cm in Figure 3-17. The difference in the detectable wavelength region due to the geometry is illustrated by these plots. For the L_β line and L_γ line, the detectable wavelengths regions are approximately the same because the geometry of the spectrograph does not change much between these lines. In designing a spectrograph, the detectable wavelength should be greater than twice as large as the half width of the observed line in order to observe the wings of the profiles. Since the largest lines expected for the Phoenix experiment are on the order of 50 mÅ FWHM, a crystal

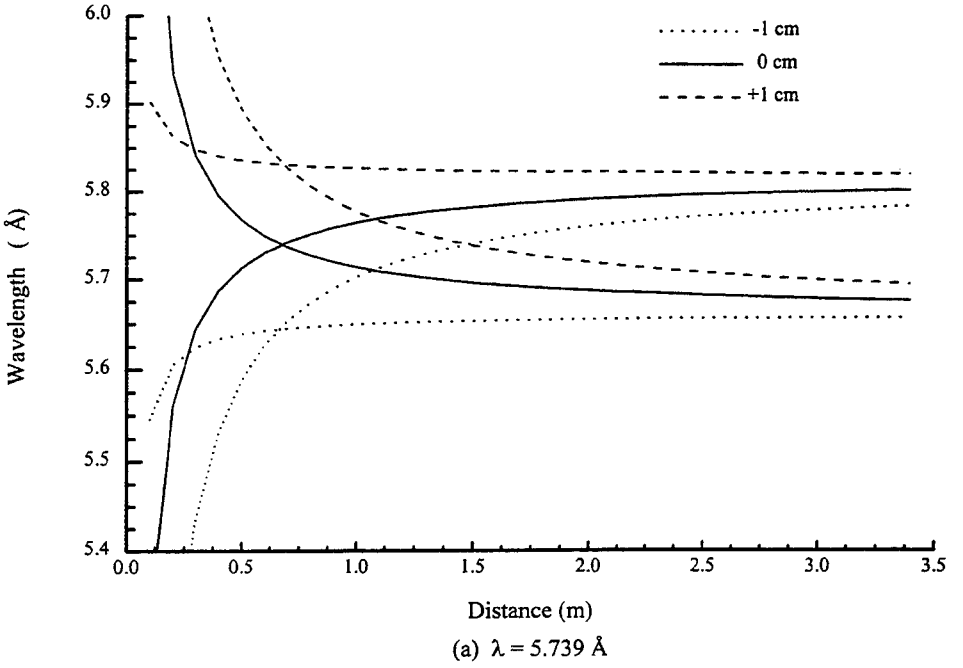

(a) $\lambda = 5.739$ Å

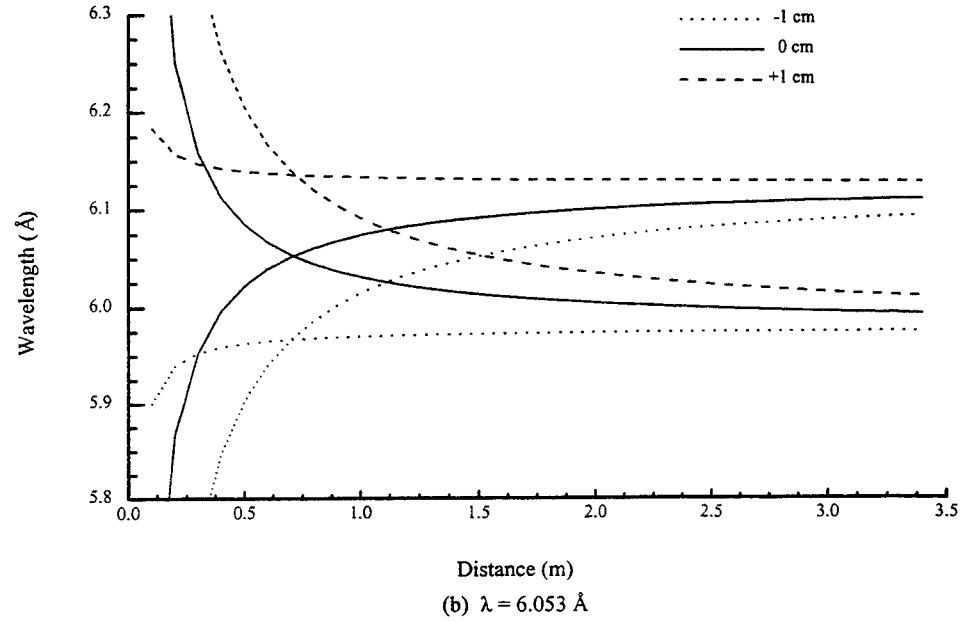

(b) $\lambda = 6.053$ Å

Figure 3-16. Detectable wavelength region for a Johann spectrometer with a 2.5 cm crystal.

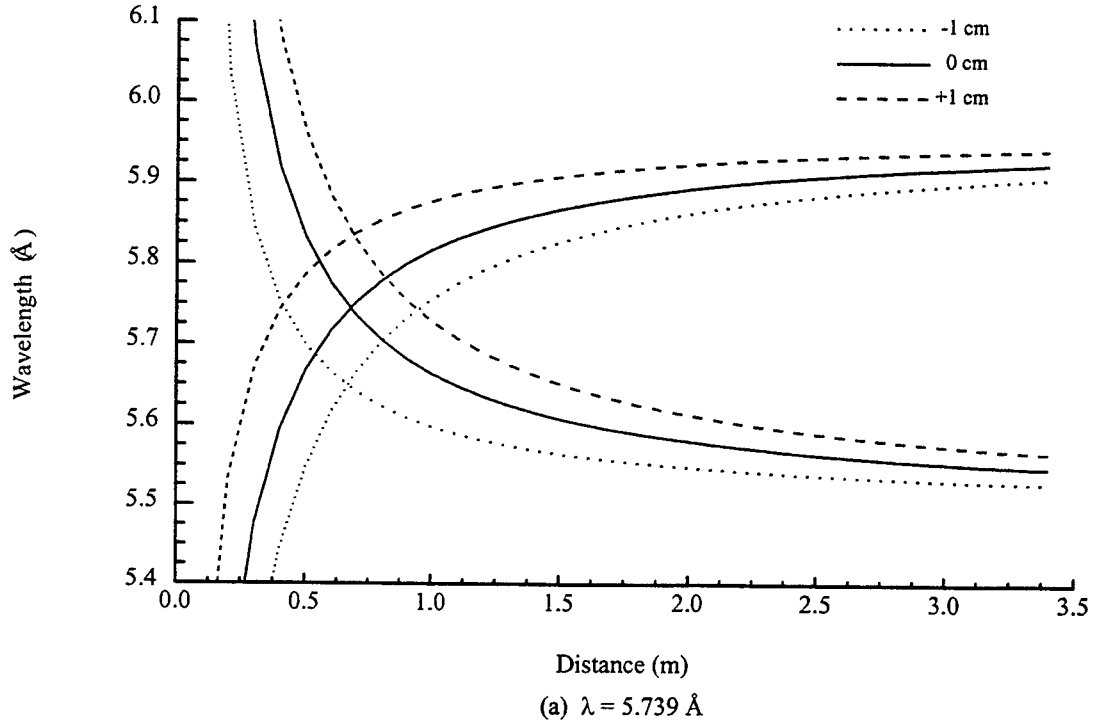

(a) $\lambda = 5.739$ Å

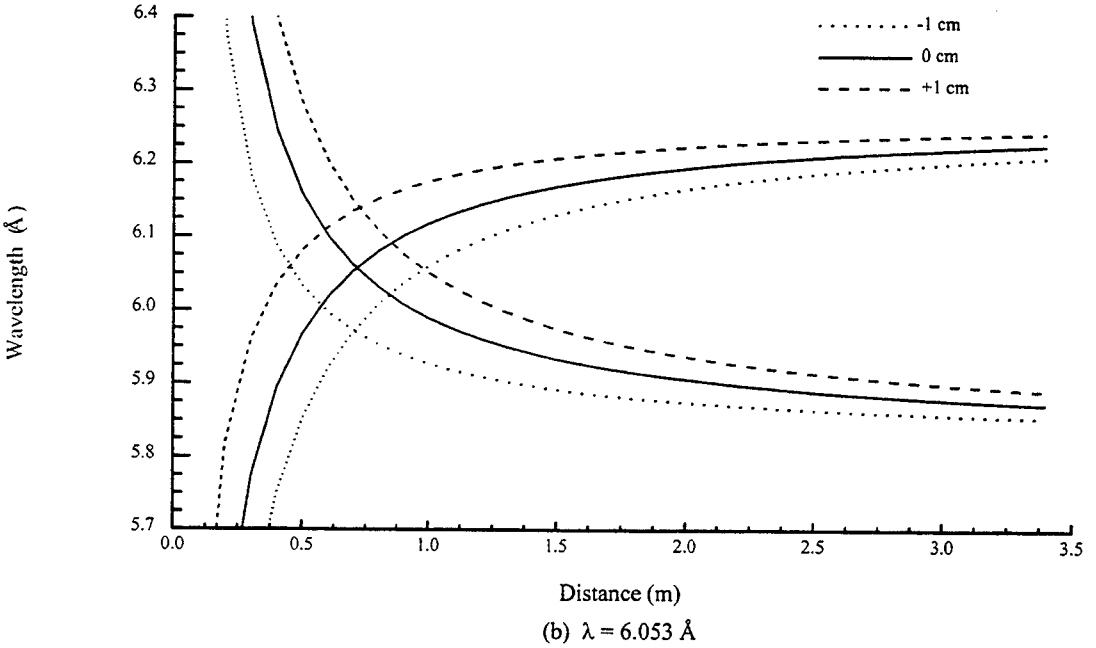

(b) $\lambda = 6.053$ Å

Figure 3-17. Detectable wavelength region for a Johann spectrometer with a 7.5 cm crystal.

length of 2.5 cm is not sufficient. The plots of detectable wavelength show that the 7.5 cm crystal should be used for the experiments on Phoenix.

Test Gaussian spectral profiles were then input for the point and line sources and the output profiles of the spectrographs were compared to the input profiles. Gaussian profiles of from 20 mÅ to 150 mÅ FWHM were traced for the test configurations. The output lines for a given input half width are shown in Figures 3-18 through 3-21 for the 2.5 cm and 7.5 cm crystals. The results for the L_γ line are not presented because they do not vary much from the results for the L_β line. These plots show that for a line of half width of 50 mÅ, the profile for both a point and 2 cm line will be correctly measured by the spectrograph if the 7.5 cm crystal is used.

The data gained from these calculations was used to design a spectrometer which would perform properly for Phoenix plasma source. The three factors of primary concern for designing the spectrograph were the source to crystal distance, the crystal length and resolution. The distance of the source to the spectrometer was important for achieving the correct intensity at the film. From the graphs of Figure 3-16 and 3-17 we see that the detectable wavelength region is proportional to the size of the crystal and the source to crystal distance. The usual procedure is to choose the diameter of the Rowland circle required to get the desired resolution, find the distance which gives the correct intensity and then use a crystal of the appropriate size. If this approach fails then the diameter of the Rowland circle must be changed to resolve the problem. From the ray tracing it was

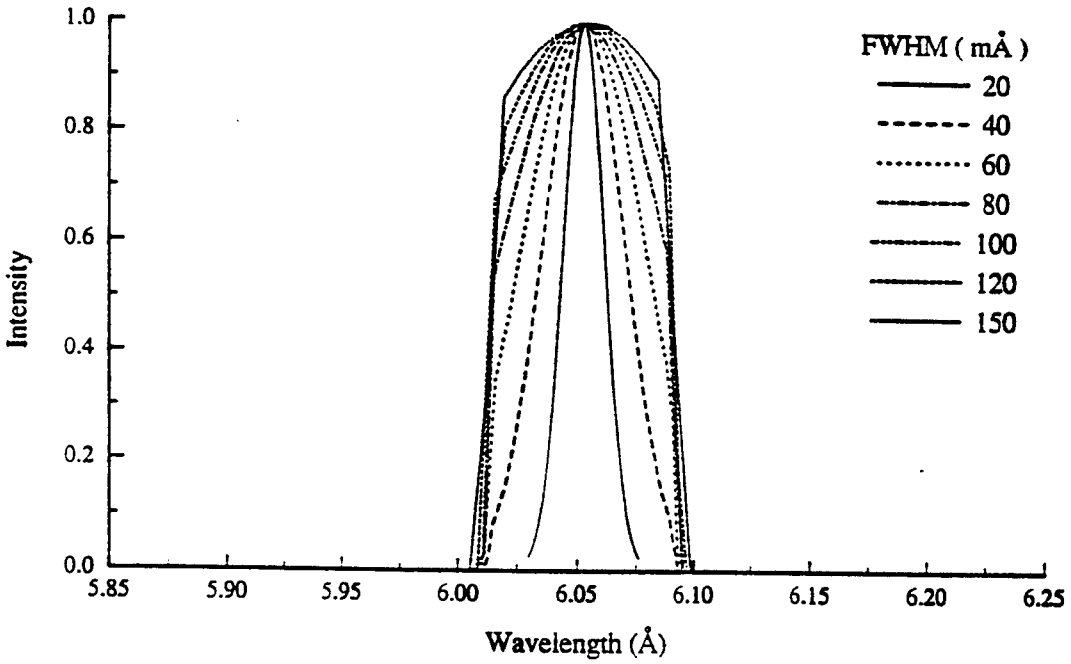

(a) Point source.

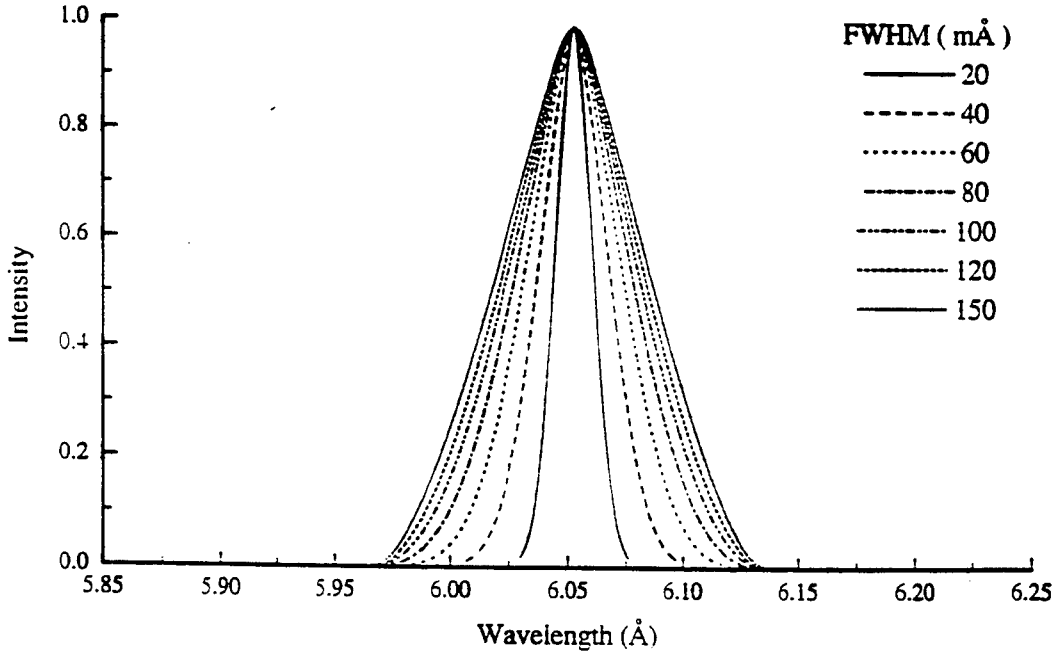

(b) 2 cm line source.

Figure 3-18. Ray Tracing for L_β with a source to crystal distance of 1.5 m and a crystal length of 2.5 cm.

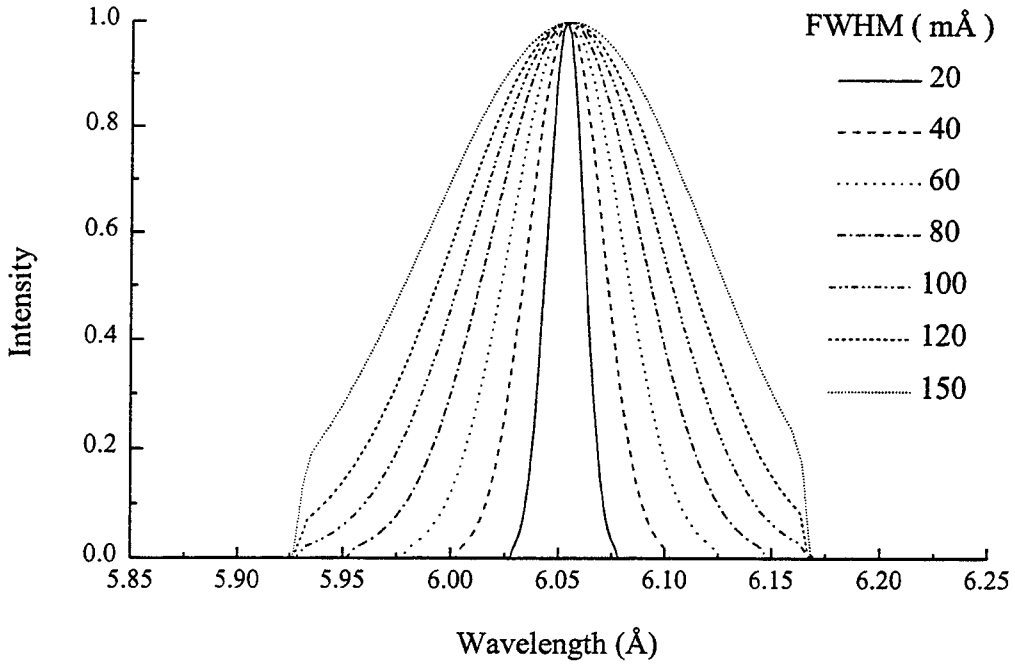

(a) 7.5 cm for a point source

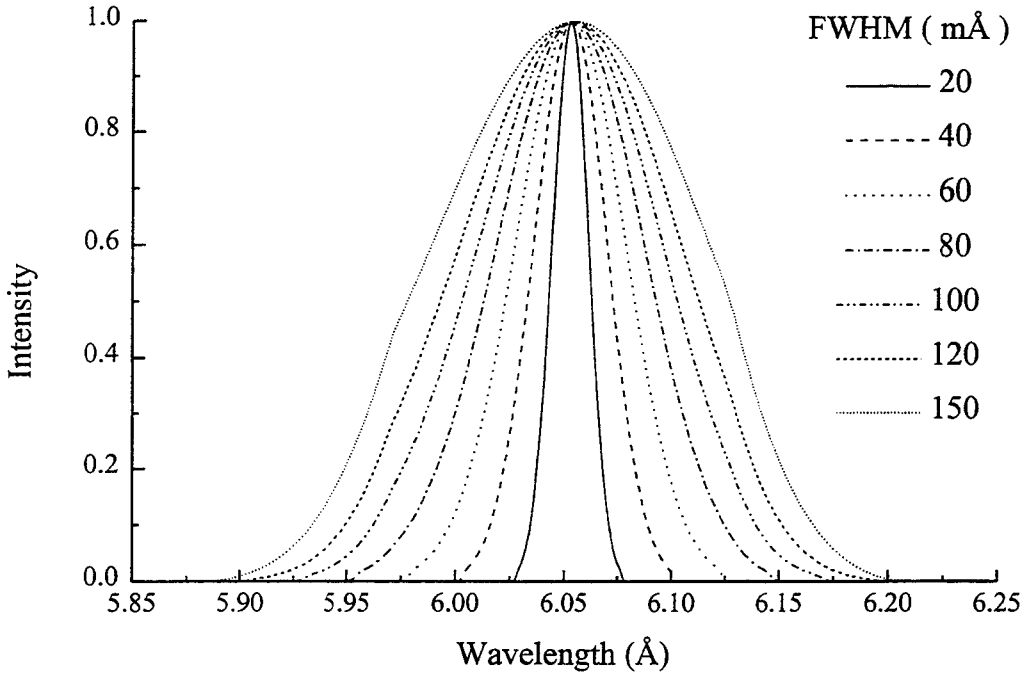

(b) 2 cm line source

Figure 3-19. Ray Tracing for L_β with a source to crystal distance of 1.5 m and a crystal length.

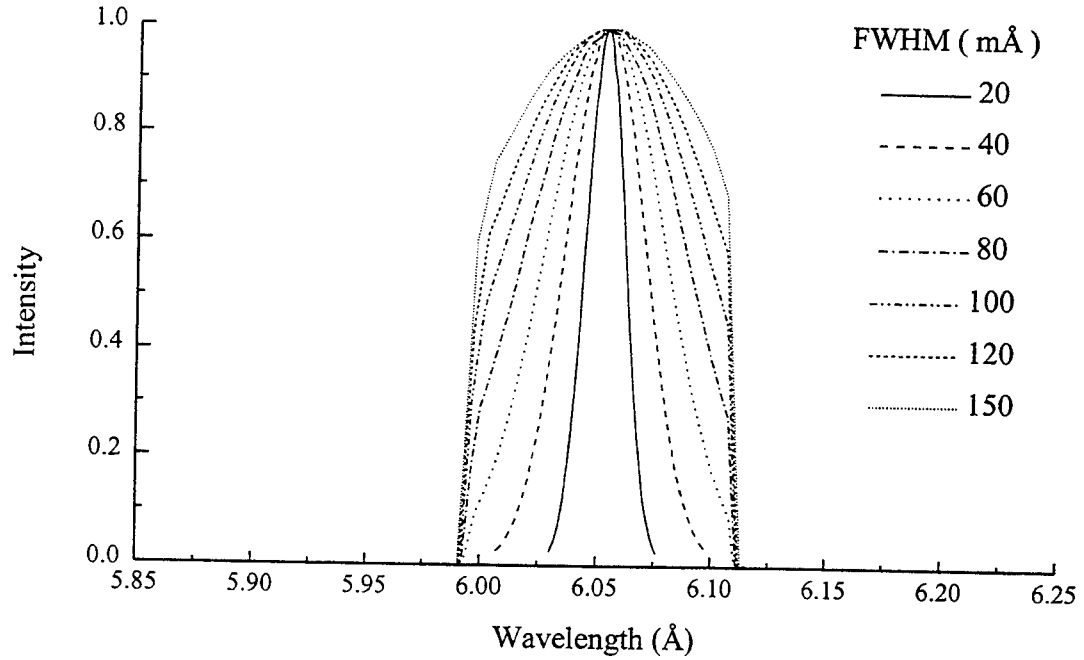

a)

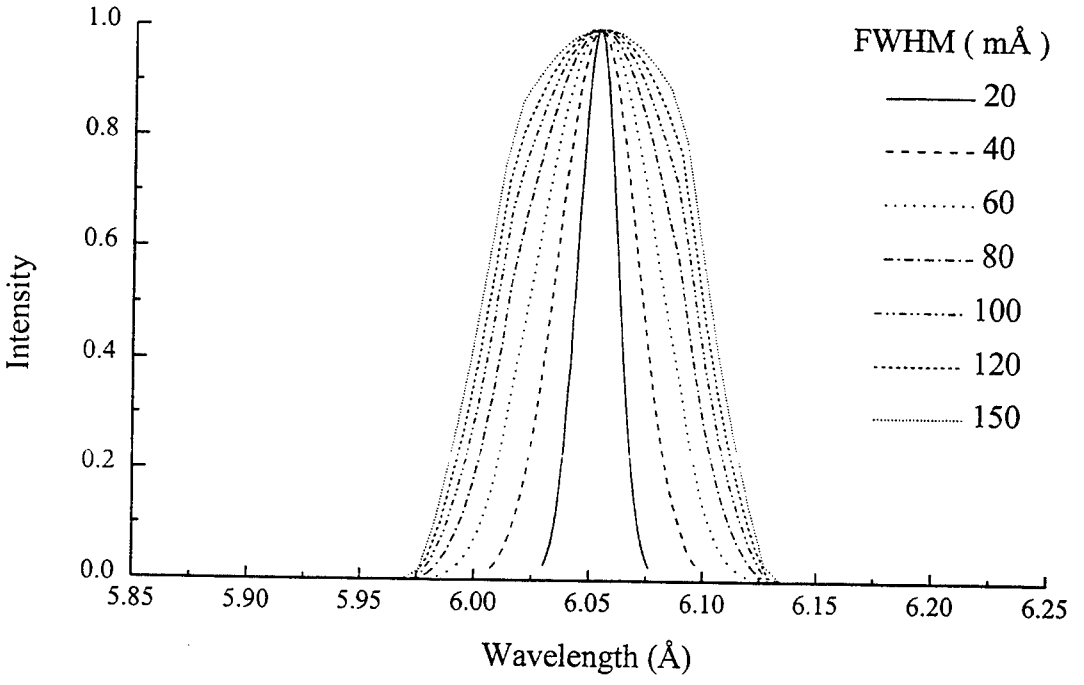

b)

Figure 3-20. Ray Tracing for L_β with a source to crystal distance of 3.0 m and a crystal length of 2.5.

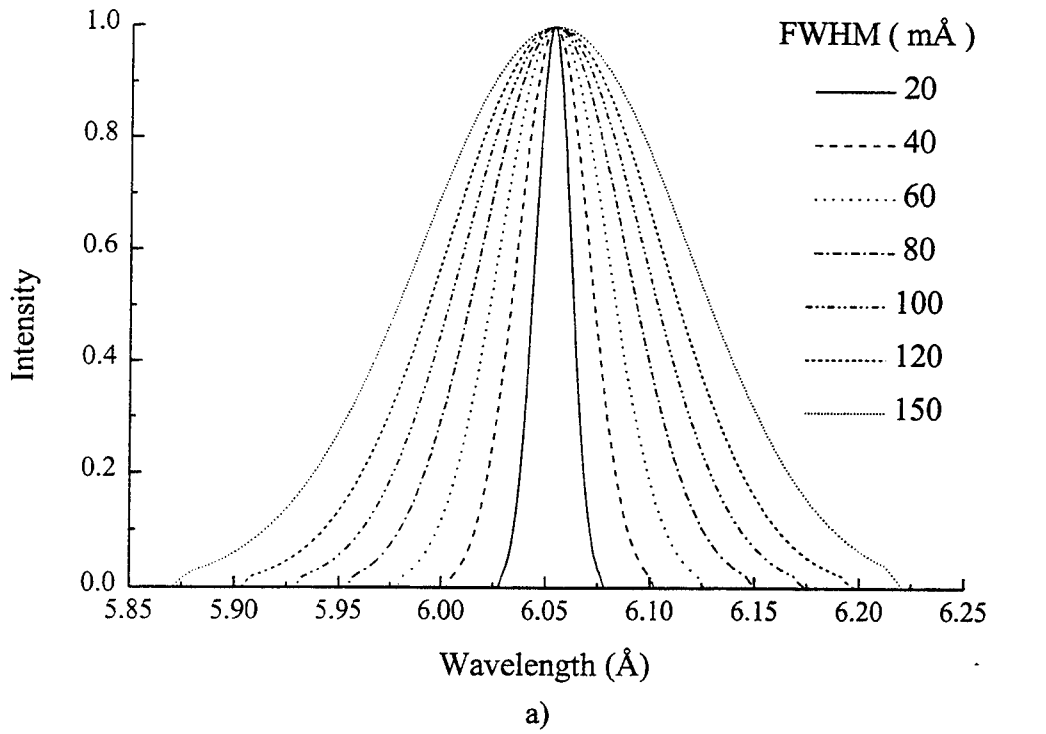

a)

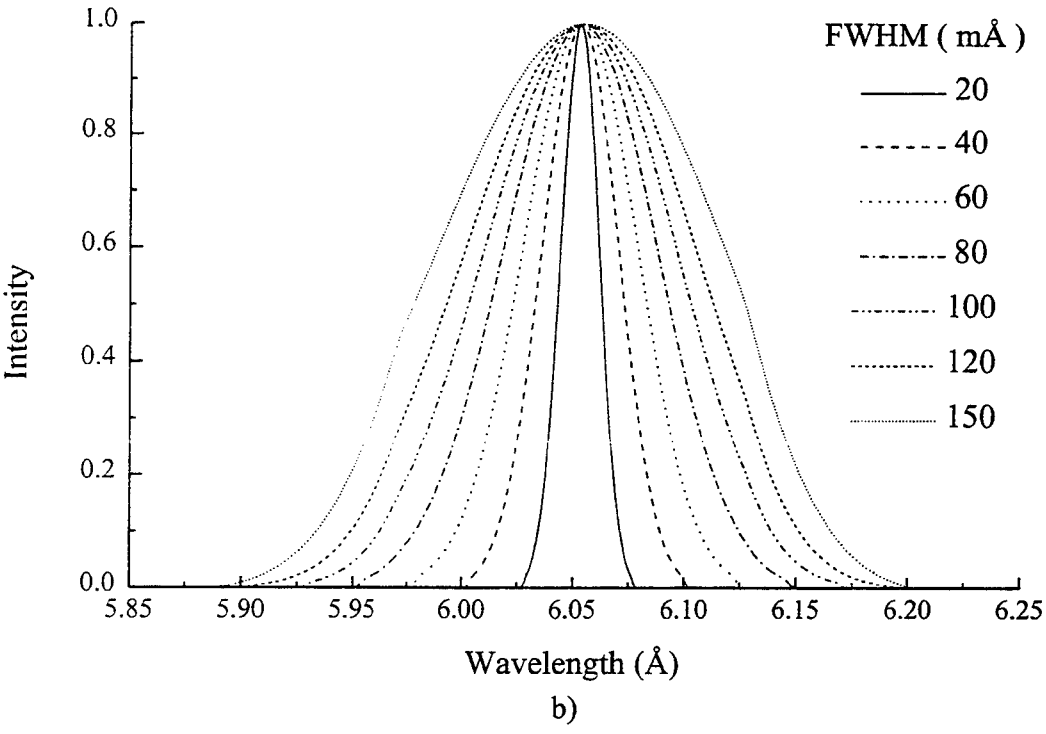

b)

Figure 3-21. Ray Tracing for L_β with a source to crystal distance of 3.0 m and a crystal length of 7.5 cm.

determined that the best configuration for the Phoenix machine was a crystal length of 7.5 cm, and a source distance of 1.5 m.

SECTION 4
EXPERIMENTAL RESULTS

4.1 RADIATION DETECTOR RESULTS.

The radiation detectors provided information about the time evolution of the radiation from the plasma. Typical signals obtained from the Si PIN diode and diamond PCD are shown in Figure 4-1. Temporally the detectors are in agreement about the time of arrival of the radiation pulse, however, the intensity seen on the two detectors shows a considerable difference in the tail of the pulse. The PIN diode detector has a larger signal after the primary pulse. The difference in the signals from the two detectors cannot be explained by the filters and response curves of the detectors alone (Section 2.1). According to the calculations for the response of the detectors, the Si PIN diode will have a lower wavelength cutoff than the diamond PCD. This would suggest that the PIN diode should have a shorter pulse, since the lower wavelengths should occur for a smaller duration. This difference in the two signals can only be accounted for by the sensitivity of the Si PIN diode to visible light, for the epoxy used to seal the Be foils was found to be partially transparent for high intensities of light.

The other useful information provided by these detectors is the power output in the radiation. The total energy of the radiation pulse for each shot was calculated by integrating the signal from the PCD detector. The total energy in the radiation, for all

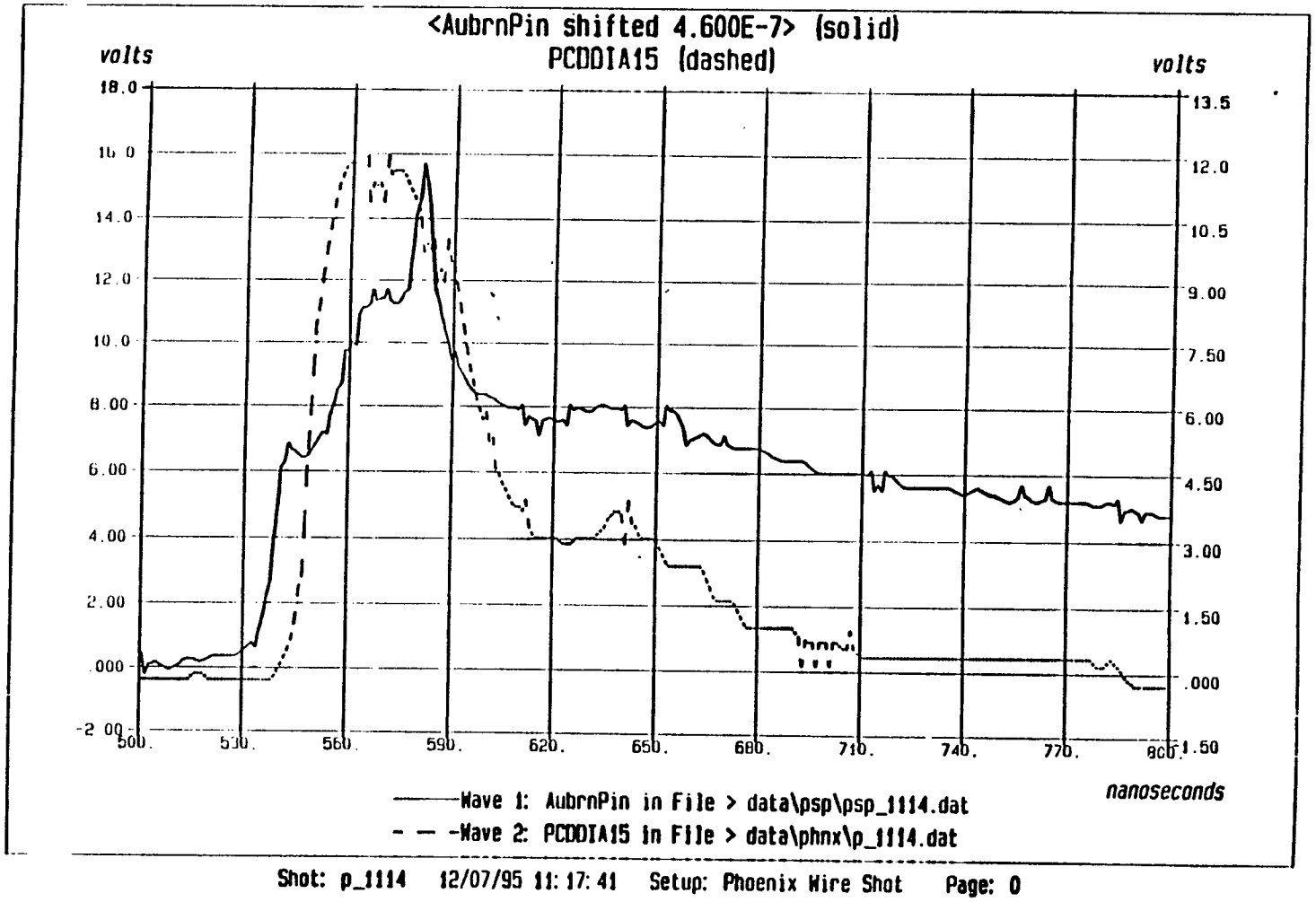

Figure 4-1. PCD and PIN diode detector signals.

wavelengths below 10 Å, from the PCD is given for each shot in Table 4-1, along with the peak machine current.

Table 4-1. Peak current and total energy output of the phoenix device.

Phoenix Shot Number	Peak Current (MA)	Total Output Energy (kJ)
1109	3.3	14.5
1110	2.9	10.5
1111	3.5	19.4
1112	3.4	16.6
1113	3.3	16.0
1114	3.5	20.9
1115	3.4	15.7
1116	3.5	19.7
1117	3.6	16.7
1118	3.5	23.3
1119	3.4	17.2
1120	3.4	19.0
1121	3.4	15.8
1122	3.5	15.2
1123	3.4	17.6
1124	3.4	14.5
1125	3.5	19.9
1126	3.5	20.2
1127	3.5	21.2
1128	3.5	21.8
1129	3.5	19.6

Table 4-1 shows that there is not much variation of the peak current even though the radiation output varies from shot to shot. It is conceivable that the variation in the output radiation results from the fact that the wires do not explode the same on every shot. The variation in the geometry of the initial plasma produced by the exploding wires may lead to differences in the quality of the pinches.

4.2. Pinhole Camera Results.

The pinhole pictures obtained at the Phoenix PRS are shown in Figure 4-2. The image on the left is a digitized scan of the film. Image processing was used to enhance the contrast of these pictures to try and reveal more structure. The two pictures to the right of the original scanned image have increasing contrast going to the right. The difference in appearance between shot numbers 1118 - 1125 and numbers 1126 - 1129 is due to the difference in the pinholes used and the distance of the film from the pinhole as discussed in Section 2.2. To get more accurate information about structures in the pinches, an EDP densitometer was used to obtain contours of the images.

For shot numbers 1118 - 1125 the densitometer was used with a 6.7 μm aperture and an EDP magnification of 20. Figure 4-3 shows the resulting contour image for shot number 1119. From this scan, the length of the hottest part of the plasma from the pinhole picture corresponds to 1.5 cm. The size of the most dense structure in the pinch is approximately 350 - 500 μm, but since this corresponds to the size of the pinhole used of 400 μm, it is clear that the picture is limited by the resolution of the camera. In anticipation of these results, shot numbers 1126 - 1129 were taken with a smaller pinholes of diameter 25 μm. For the scans of these pictures a 3.4 μm aperture was used with an EDP magnification of 20. The resulting contour for shot number 1126 is shown in Figure 4-3. The length of the hottest part of the plasma from this pinhole picture corresponds to 1.8 cm. These scans do not show the structure that was apparent in the scans for shot numbers 1118 - 1125 . Since film saturation was suspected to be a possible explanation for the lack of

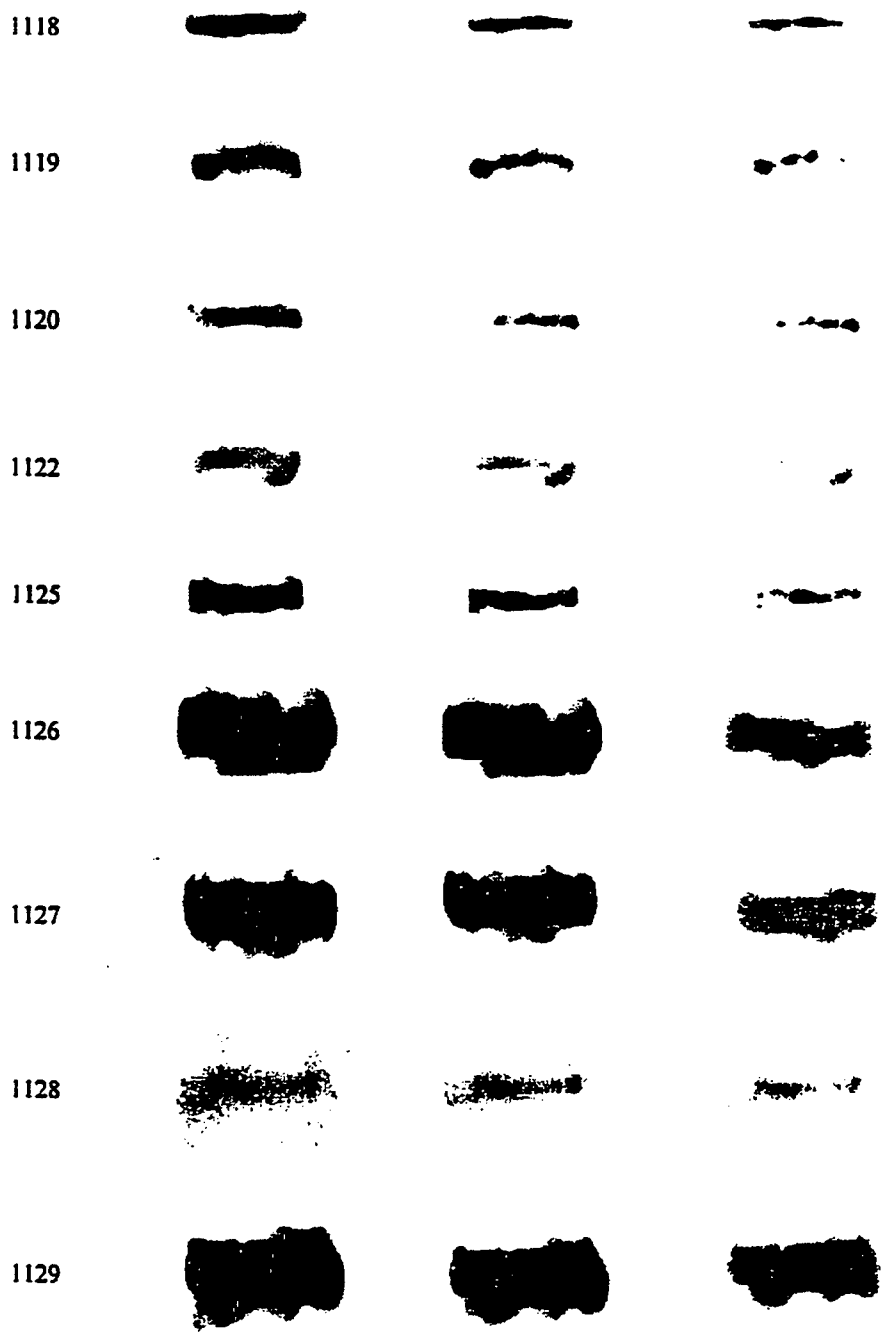

Figure 4-2. Pinhole camera pictures.

(a) Shot number 1119

(b) Shot number 1126

Figure 4-3. EDP scans of pinhole pictures.

structure, the opacity of the film was checked. The maximum opacity of the film was found to be 2.2 which corresponds to a region of saturation on the film (Appendix E). It was therefore not possible to use this data to determine the size of the "hot spots". The best that we could get from the pinhole data was that the size of the "hot spots" were smaller than 400 μm.

4.3 Four Frame Camera Results.

The pictures obtained using the four frame camera are shown in Figure 4-4. Scans of the pictures were taken using the EDP densitometer. Figure 4-5 shows a sample of the results for frame 3 of shot 1127 at 50x EDP magnification. The size of the most dense region for this shot is approximately 500 μm, corresponding to the size of the pinhole. These results verify that a 400 μm pinhole is too large to resolve the structure of the pinches. Insufficient resolution was found to be a problem in all of the shots. For shot number 1129 a 100 μm pinhole was used to try and improve the results. The image appears to have lower resolution than the pictures obtained with the 400 μm pinholes. Since only one shot with this size pinhole was obtained it is difficult to interpret the data. The image could be poor because of the camera resolution, or the pinch could have been caught in expansion. These results suggest that in order to obtain better results it is necessary to use smaller pinholes. The use of smaller pinholes must be accompanied by moving the camera closer to the plasma so that the total radiation to the film can be maintained. The resolution of the four frame camera pictures do not give sufficient resolution to determine the final size of the pinch.

1123

1125

1127

1128

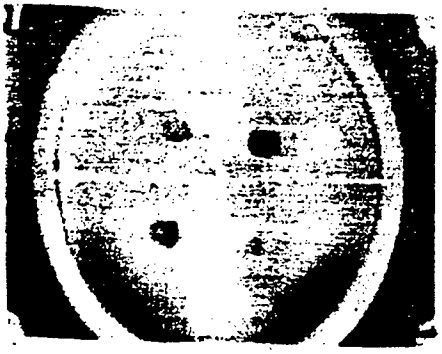

1129

Figure 4-4. Four frame camera pictures.

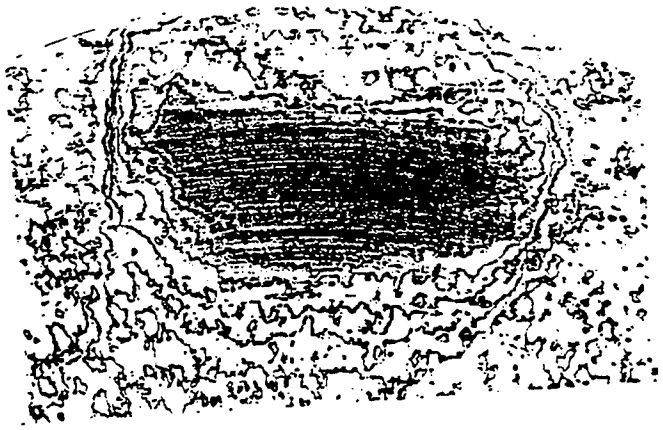

Figure 4-5. EDP densitometer scan of frame 3 of shot number 1129 at 6.5X magnification.

4.4 Plasma Parameters from Johann Spectrometer Profiles.

The spectra used in this analysis were scanned using a Joyce Loebl scanning densitometer (Appendix F). Between 4 and 6 scans across the central region of the spectra were made and averaged with 0.5 mm spacing between scans. This was done to reduce the noise due to the graininess of the film. The Biomax MR film used for the Johann and flat crystal spectrograph was calibrated to find the region of linear response (Appendix E) to ensure that film saturation was not a problem.

All of the spectra obtained from the Phoenix source were examined to determine which shots represented good useable data. When the spectrometers are aligned properly the spectra should appear centered on the film both horizontally and vertically. Horizontal displacement indicates that the film is rotated off of the Rowland circle of the crystal, resulting in defocusing. Vertical displacement on the film indicates that the x rays are in a plane which is tilted with respect to the plane of the spectrometer. Since the 1 m diameter of the Rowland circle used is large, vertical displacements of a few centimeters on the film could not lead to significant differences in the geometry. The aberrations produced by this displacement are discussed by Jones, Paschen, and Nicholson.[30] A secondary problem with the displacement of spectra on the film was that if the film was too far displaced, the middle of the line did not appear on the film. Spectra were chosen which were centered both horizontally and vertically within 1 cm on the film. Figures 4-6 and 4-7 shows the location of the extremes of the spectra on the film horizontally and vertically.

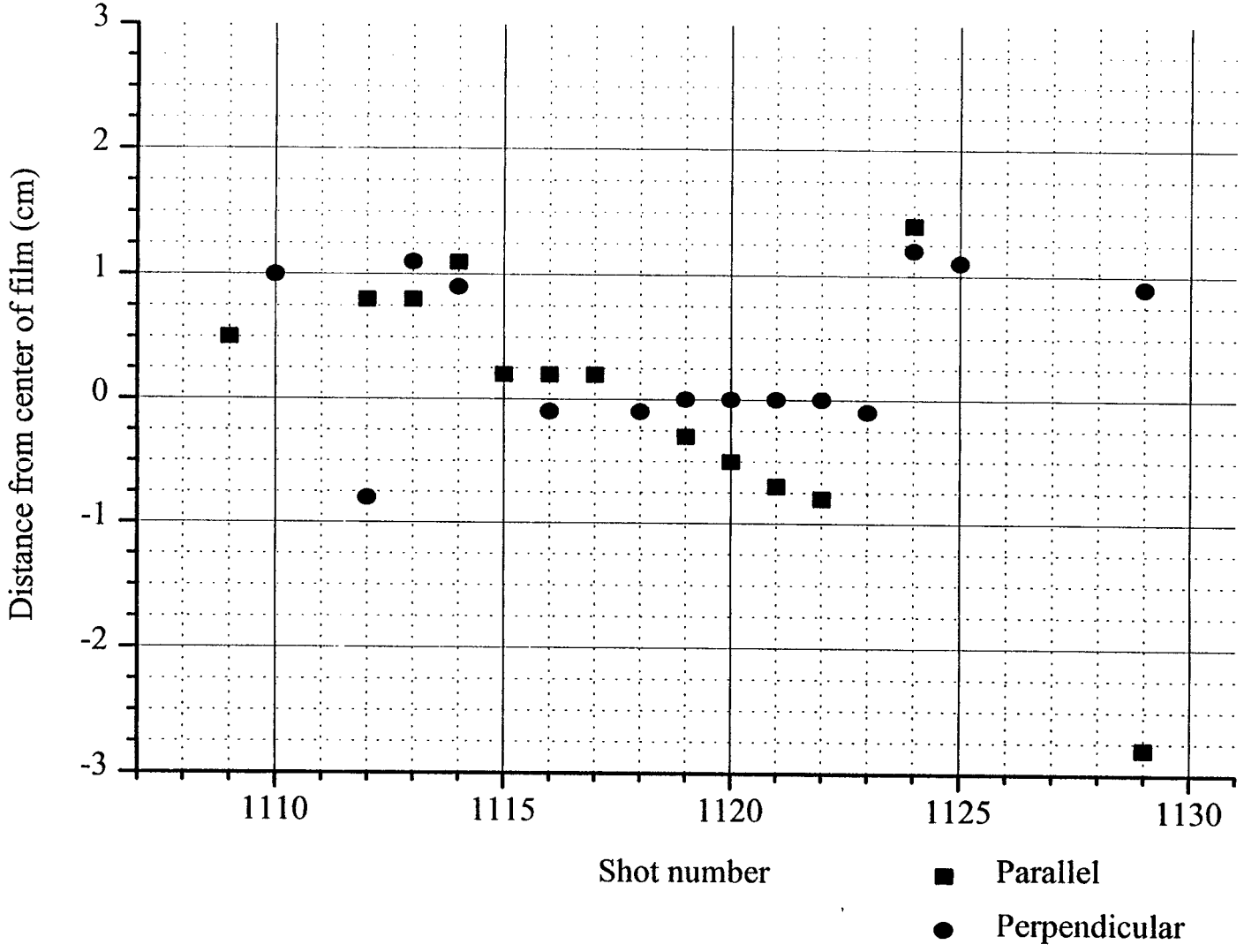

Figure 4-6. Horizontal position of spectra on film.

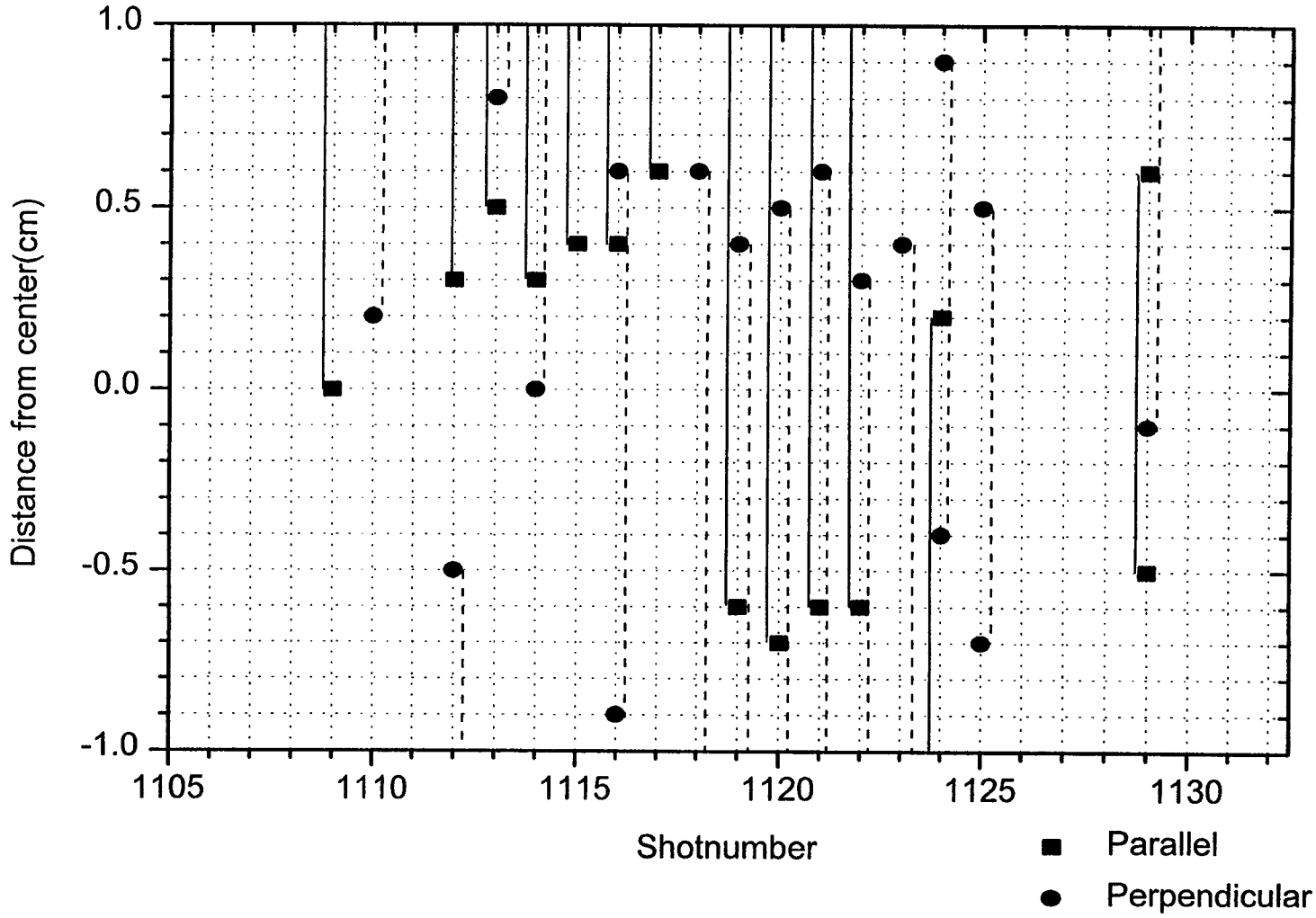

Figure 4-7. Vertical Extremes of spectra on film.

Eleven "good" spectra were obtained for the L_β line. For the parallel configuration the shot numbers were 1119 - 1122 and for the perpendicular configuration the shot numbers were 1116, and 1118 - 1123. Three "good" spectra were also obtained for L_γ. One was obtained on shot 1124 for the parallel configuration and two were obtained on shots 1124 and 1125 for the perpendicular configuration.

Figure 4-8 (a) and (b) show the typical spectra obtained for the L_β and L_γ lines on the Phoenix PRS. The L_β spectra has two Al XII lines on the red wing of the line. For this reason the blue wing of L_β was used for analysis. The spectra for L_γ shows L_γ, L_δ and L_ε in addition to a Si XIII line. The silicon line resulted from the use of silicon oil to clean the machine. Since these lines occur on the blue side of the line, the red side of the L_γ line was used for analysis.

Figure 4-9 shows the blue side of the L_β lines and Figure 4-10 shows the red wings of the L_γ lines for the data that was analyzed. The data for the shots, where two states of polarization were obtained, show differences in half widths between the two states of polarization, with the exception of shot number 1124. Since the center of the line profiles are strongly determined by density and less by the oscillating electric fields, the differences in the line profiles indicate that the spectrometers were looking at regions with different densities. The fact that the spectrometers might have seen different densities in the plasma is reasonable if we consider the difference in geometry of the spectrographs. For the spectrograph in the parallel configuration, a scan perpendicular tothe dispersion on the film corresponds to viewing different regions of the plasma along

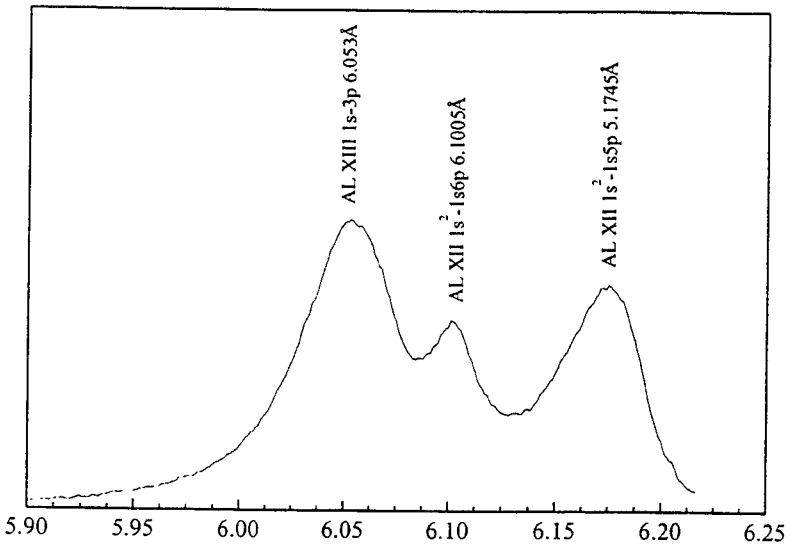

(a) L_β spectra for shot number 1122 parallel

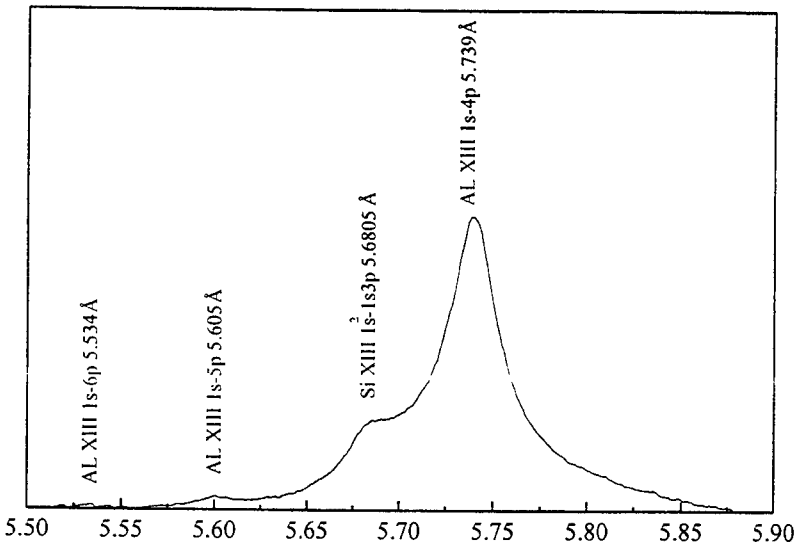

(b) L_γ spectra for shot number 1124 parallel

Figure 4-8. Spectra obtained on the Phoenix PRS.

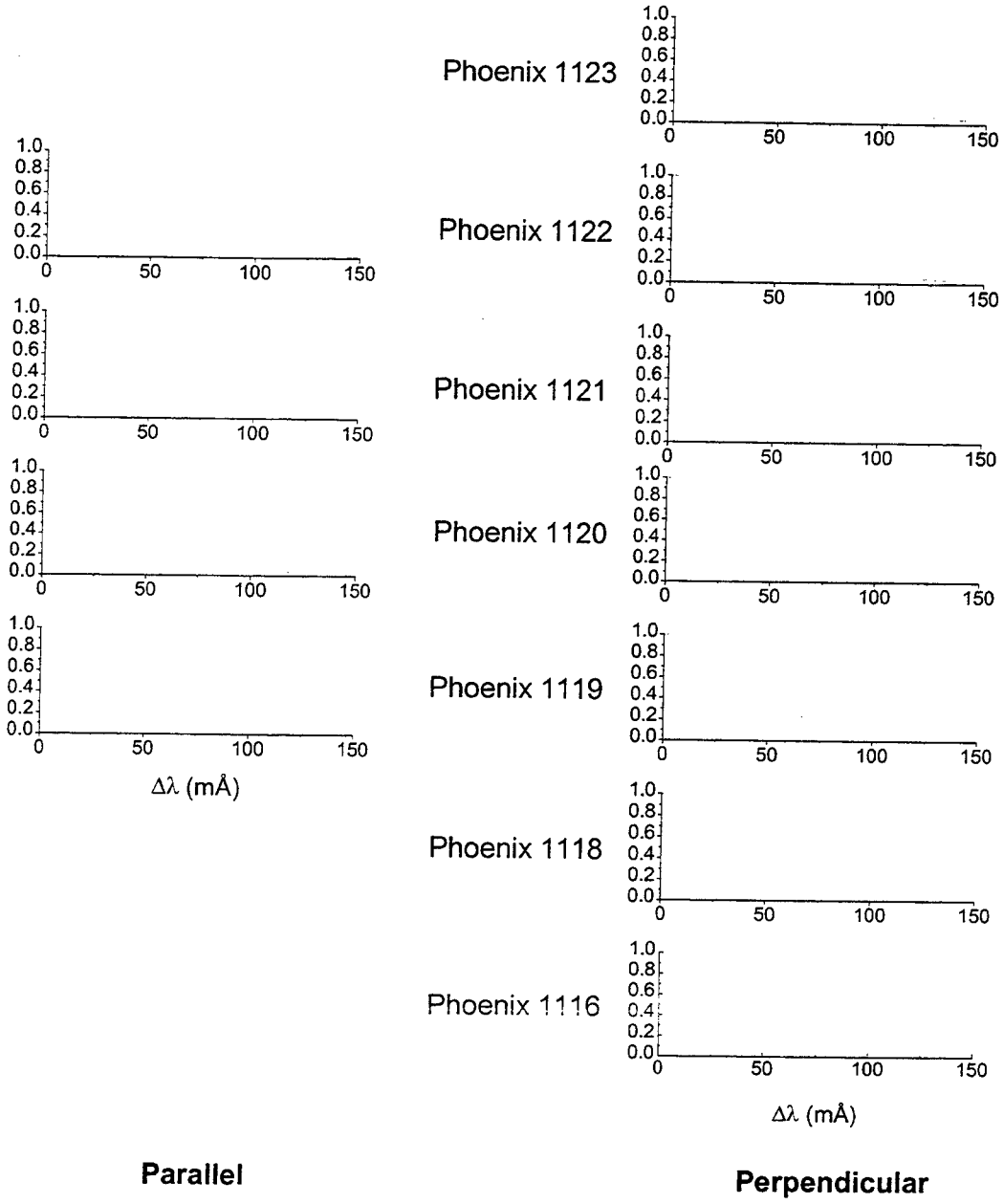

Figure 4-9. Blue wing of L_β lines.

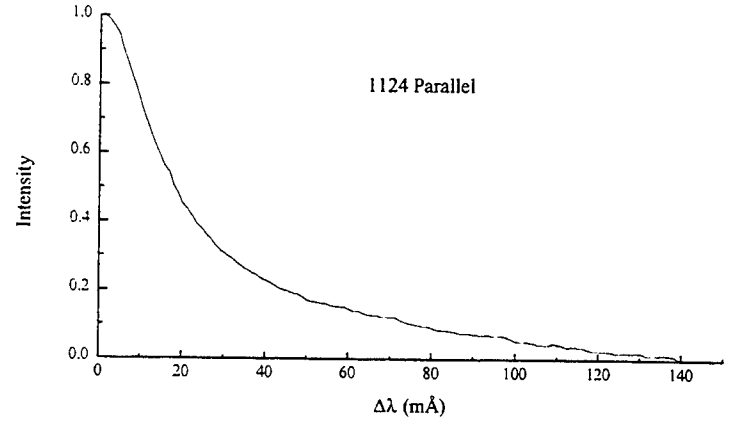

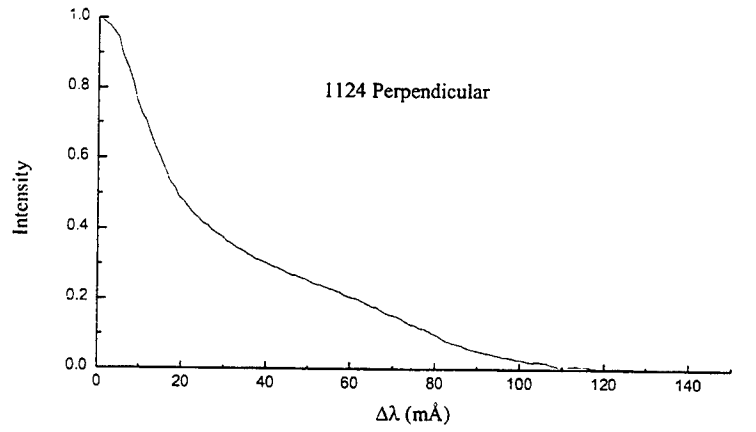

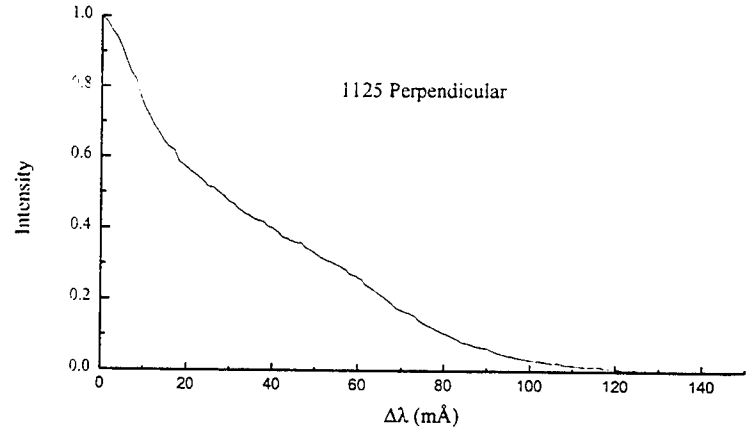

Figure 4-10. Red wing of L_γ lines.

the length. For the perpendicular spectrograph, a scan perpendicular to the dispersion corresponds to a scan across the width of the plasma. Due to the nature of the elongated source, at best one can expect to view regions with similar average densities.

Once the spectra for the blue wing of L_β and the red wing of L_γ was obtained for the "good" shots, the model parameters that produced these lines could be found. Since there are six parameters in the model this corresponds to a six dimensional search. Each parameter can vary over a range of approximately 5, so it would take approximately 10^{10} searches to cover the entire range to a resolution of 0.1. To avoid having to search the entire range, a six dimensional Sobol quasi-random sequence was employed.[32] A Sobol sequence generates numbers in an *n* dimensional space such that each additional point added is further in the space from previous points. As more of the sequence is produced, the space is searched to a finer scale. This is best illustrated by looking at the numbers generated for a two dimensional Sobol sequence. Figure 4-11 shows the two dimensional Sobol sequence up to 1024 points.

A program was written to find the parameters which matched the experimental lines. Eleven points were taken from each of the experimental profiles to be compared to the profiles generated by the model. The scheme was to take a set of parameters generated by the Sobol sequence, produce the profile at these points, and then compare them to all sets of experimental data for the line. If all 11 points in the experimental profile matched, to within a set tolerance, the parameters were recorded as a solution for the experimental

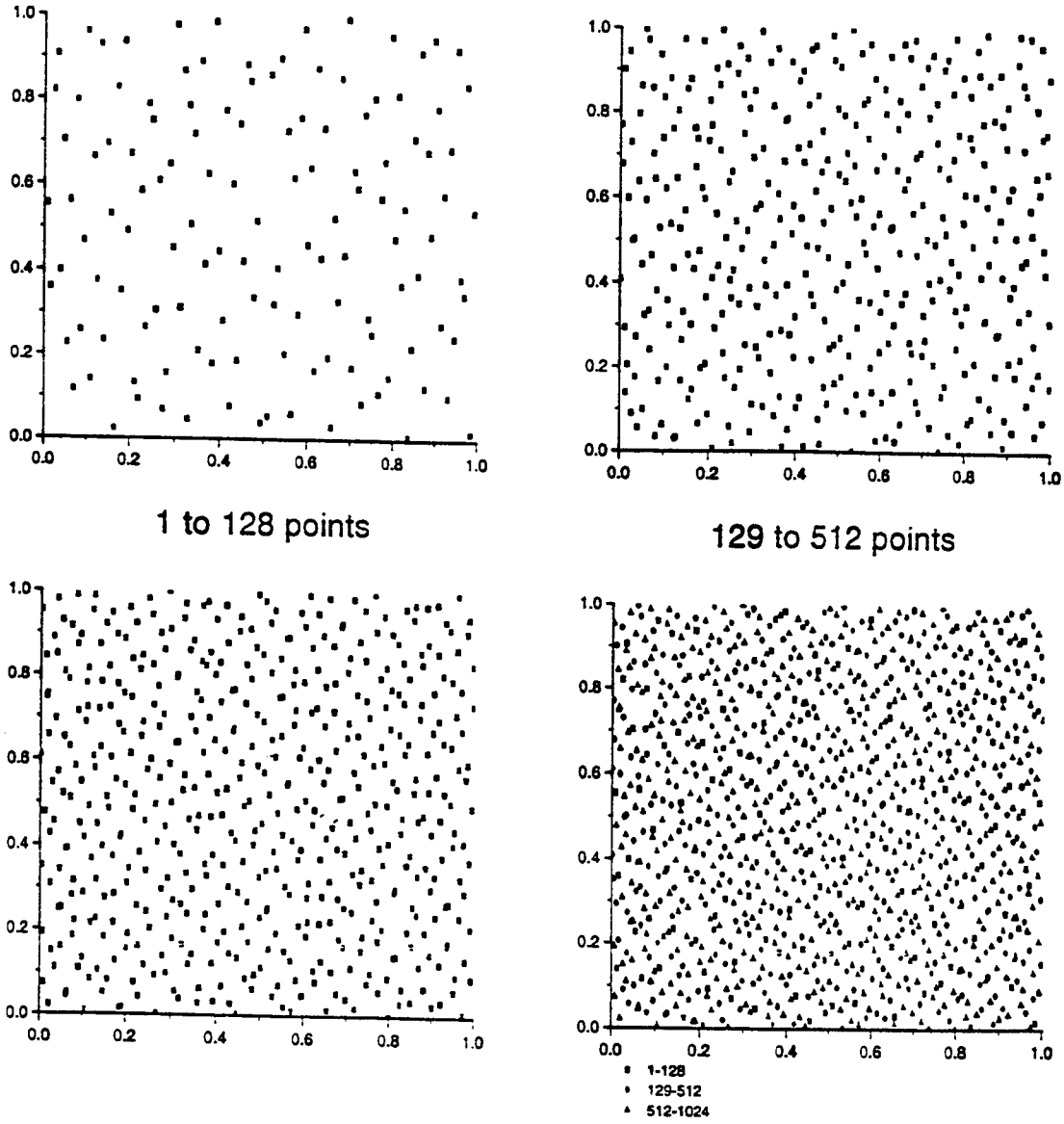

Figure 4 11. Two dimensional Sobol sequence.

data. This was done for a number of possible baselines to ensure that the results were not a function of a particular baseline choice.

For the L_β and L_γ lines, 11 different baselines were tested. In Figure 4-9 and 4-10 the baselines were estimated from where the wings of the lines died out. This represents a best initial guess of the baselines. The height of these lines were normalized to unity and baselines were adjusted in terms of a percentage of this height. Raising the baseline by 10%, for example, corresponded to subtracting 0.1 from the best guess profile and renormalizing the line. Baselines ranging from raising the baseline 20% to lowering the baseline by 30% were tested by increments of 2.5% for the L_β and L_γ lines.

The range of model parameters tested ranged from 2.0×10^{-4} to 7.0. For L_β, 25,000 searches were performed and for L_γ 100,000 searches were performed. The number of searches was based on the number of solutions that were produced. Figure 4-12 shows a sample of the results from the search of the L_β line for shot number 1118 in the perpendicular configuration and Figure 4-13 shows the results from the search of the L_γ line for shot number 1124 in the parallel configuration. Figure 4-14(a) and 4-14(b) have the fits of the produced profiles to the experimental profiles for these shots. These searches illustrate that there are many sets of parameters which can reproduce the experimental data. A list of the range of each parameter, where solutions have been found, is summarized in Table 4-2 for the L_β line and Table 4-3 for the L_γ line.

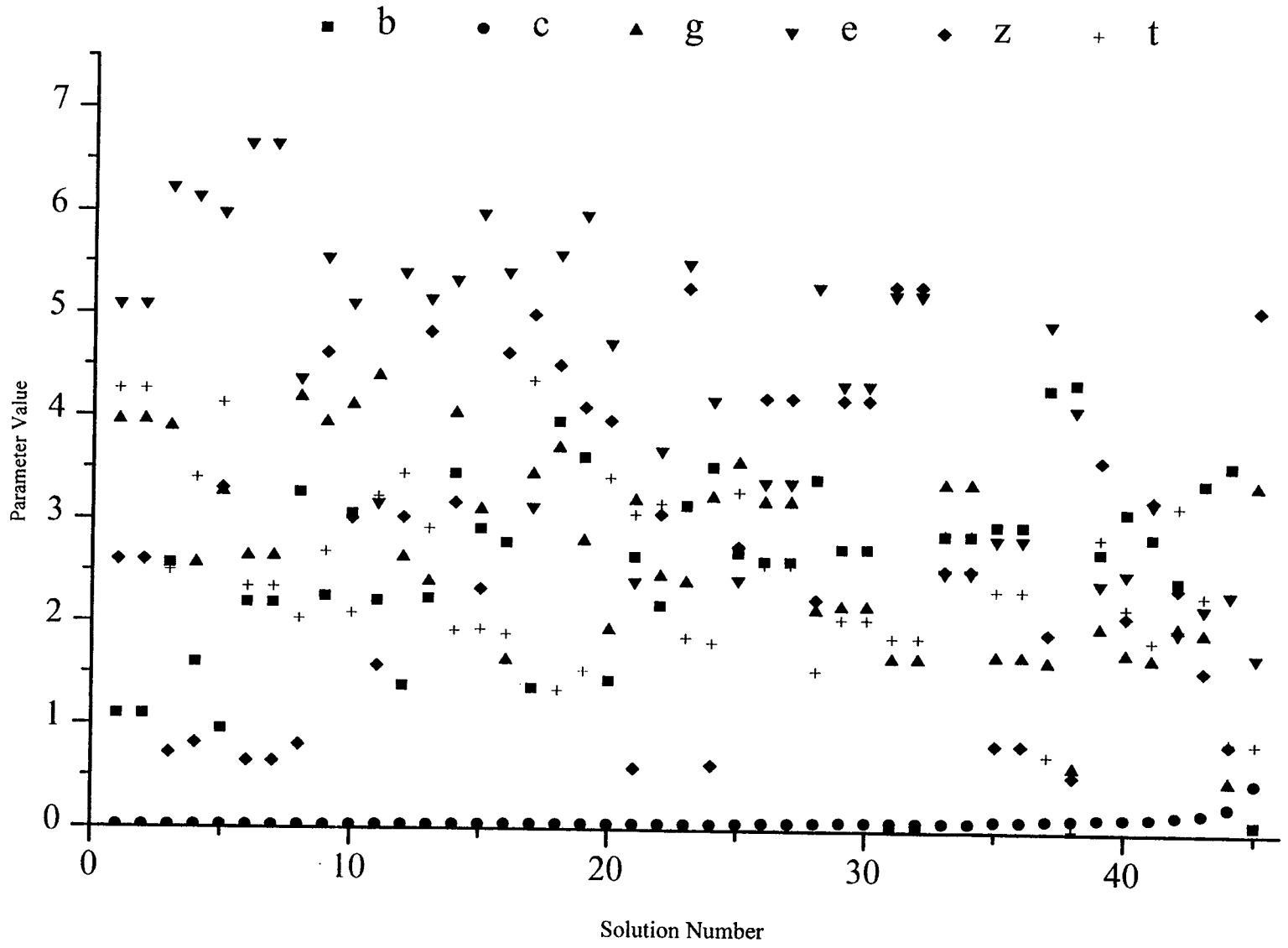

Figure 4-12. Search results for L_β shot number 1118 perpendicular for all baselines.

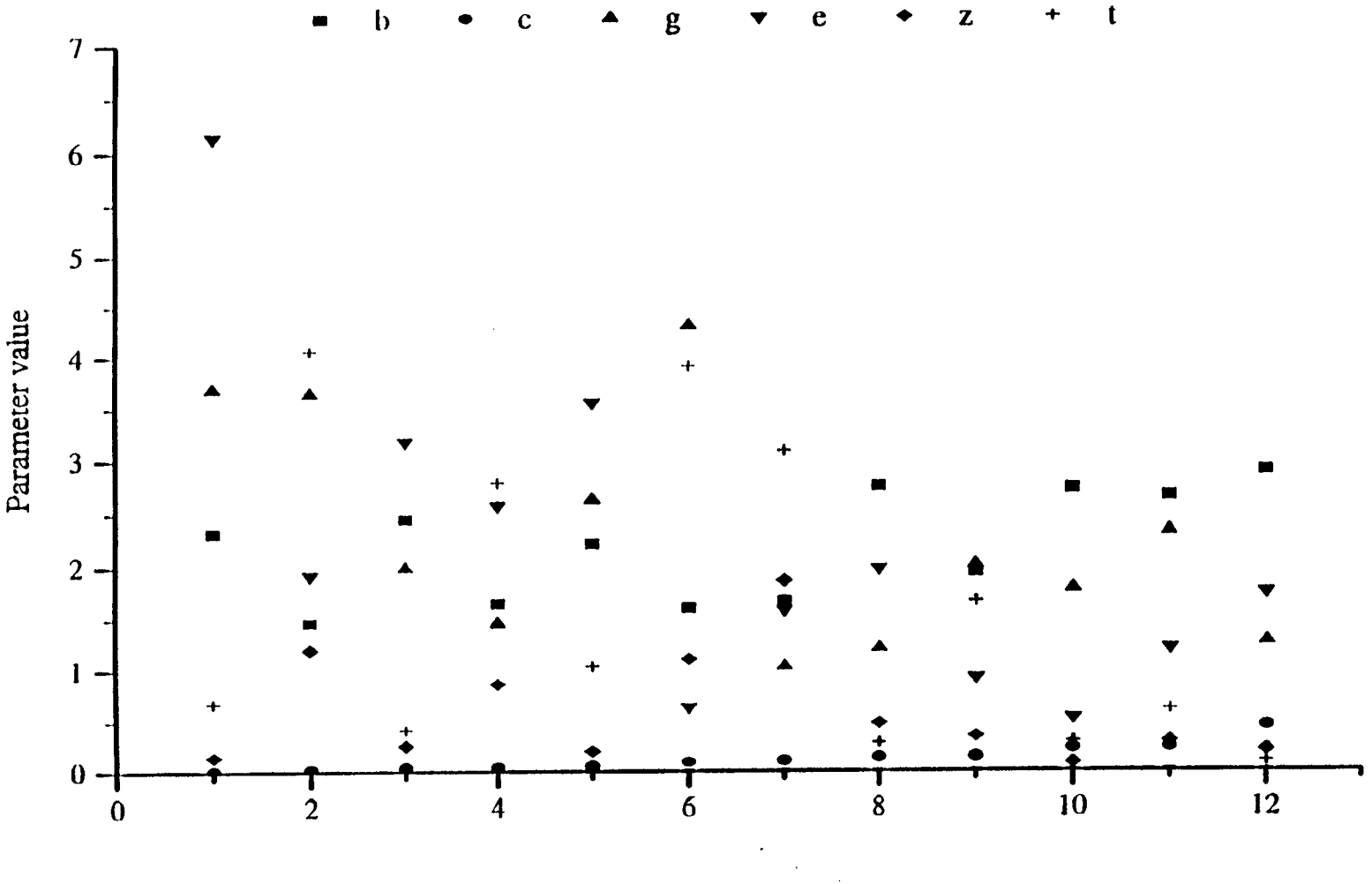

Figure 4-13. Search results for L_γ shot number 1124 parallel for all baselines.

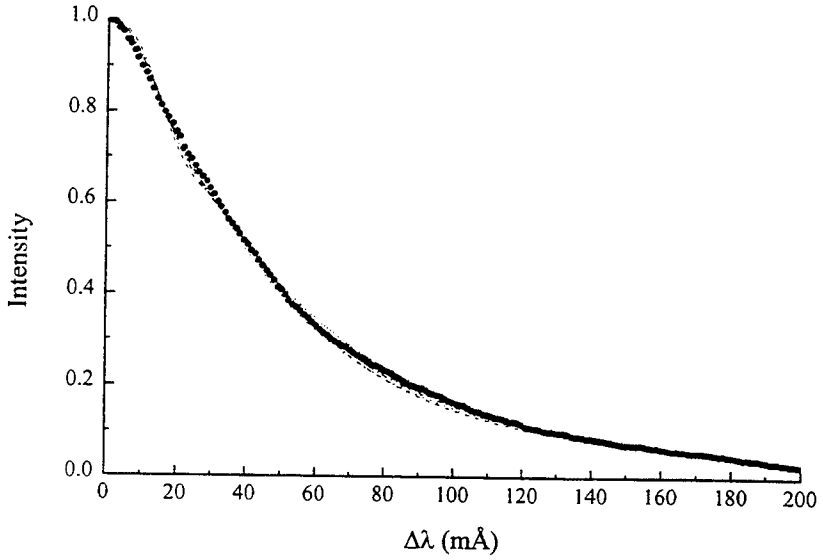

(a) L_β for shot number 1116 perpendicular

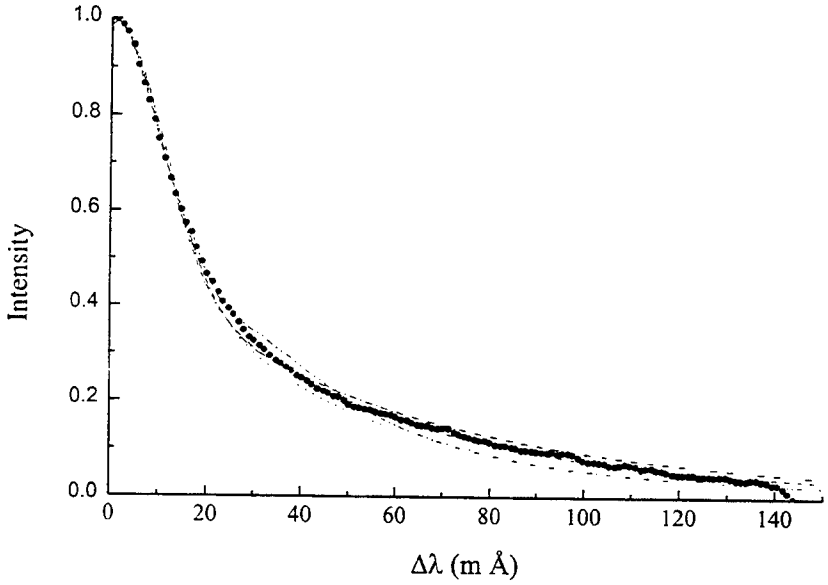

(b) L_γ for shot number 1124 parallel

Figure 4-14. Fit to the experimental profiles.

Table 4-2. Range of parameters for Lyman β which fit the experimental profiles.

	b	*C*	*g*	ε	*z*	*t*
16P	1.1 - 2.8	.02 - .18	1.4 - 3.7	1.4 - 5.3	.16 - 5.4	1.3 - 2.2
18P	0.9 - 4.4	.02 -.26	0.5 -.44	1.9 - 6.6	0.5 - 5.3	0.7 - 4.4
19L	2.2 - 3.9	.02 -.15	1.1 - 4.2	1.2 - 6.9	0.2 - 5.0	.02 - 1.6
19P	1.2 - 3.3	.02 -.11	1.2 - 4.4	2.4 - 6.6	0.2 - 5.3	1.5 - 3.8
20L	0.9 - 3.1	.02 -.33	1.1 - 3.3	1.2 - 6.0	0.8 - 5.0	0.2 - 3.4
20P	1.0 - 2.9	.03 -.22	1.2 - 4.4	1.8 - 6.8	0.2 - 5.4	1.8 - 3.9
21L	3.0 - 3.5	.02 -.04	2.2 - 4.1	4.2 - 6.4	0.7 - 4.7	0.2 - 0.8
21P	1.3 - 3.3	.02 -.15	0.8 - 4.2	2.7 - 6.8	0.6 - 5.3	1.1 - 2.8
22L	1.0 - 3.6	.004 -.49	0.5 - 4.5	1.1 - 6.2	0.6 - 5.1	.03 - 3.0
22P	2.1 - 3.3	.03 -.33	0.9 - 3.3	0.9 - 5.6	0.1 - 4.9	0.6 - 3.0
23P	1.7 - 3.9	.01 -.47	0.9 - 4.5	1.3 - 6.9	0.1 - 5.4	0.3 - 3.1

Table 4-3. Range of parameters for Lyman γ which fit the experimental profiles.

	b	*C*	*g*	ε	*z*	*t*
24L	1.5 - 2.9	.01 -.5	1.0 - 4.3	0.5 - 6.1	0.1 - 1.9	0.1 - 4.0
24P	1.3 - 2.2	.01 - 0.2	0.4 - 4.2	0.6 - 6.7	.05 - 2.2	0.2 - 4.4
25P	1.3 - 2.4	.05 -.3	1.0 - 4.3	0.9 - 3.2	.03 -.22	0.6 - 4.07

It is clear from these results that a fit to one line does not produce a unique solution. Since there are effectively seven degrees of freedom, six parameters and one choice of baseline, less parameters or more constraints are needed to find unique parameters. In order to get an estimate of the key parameters from the L_β and L_γ lines, the searches were performed again using fewer of the parameters.

A reduced search for the L_β lines, with electric field anisotropy turned off, was performed to get an estimate of the plasma parameters b, C, g, ε, and t. We expect the lines to depend strongly on ε, since the lines appear to be predominantly broadened by the oscillating electric fields. This is illustrated by looking at the plots of log intensity vs. $\Delta\lambda$ for the L_β lines (Figure 4-15). These plots show a quasi-linear behavior indicative of a superposition of Gaussian profiles. The superposition of Gaussian profiles results from the sum of the envelopes of the Stark broadened components under the action of oscillating electric fields. The search performed with the reduced parameter set for all L_β lines lead to the parameters $b = 2.0 - 4.0$, $C = 0.02 - 0.4$, $g = 0.3 - 2.5$, $\varepsilon = 1.0 - 2.5$, and $t = 1 - 3$.

A reduced search for the gamma line was also performed. Since the L_γ line has a central component which is unaffected by Stark broadening, the center of the line is dominated by Doppler broadening. The oscillating electric field will dominate in the wing of the line where the Doppler profile of the central component dies out. For this reason, the wings of the gamma line were fitted with the reduced parameter set C, g, ε, and z. The parameter z was included to determine the anisotropy of the electric fields from shot number 1124 where the spectrometers are looking at a similar region of the plasma. Several sets of the reduced parameters were found to fit the wings of the lines. To reduce the number of solutions, we required that there be a reciprocal relationship for z in the perpendicular configuration to the parallel configuration for the spectrometers, since the meaning of a and b in z are swapped in the two configurations. The results for the

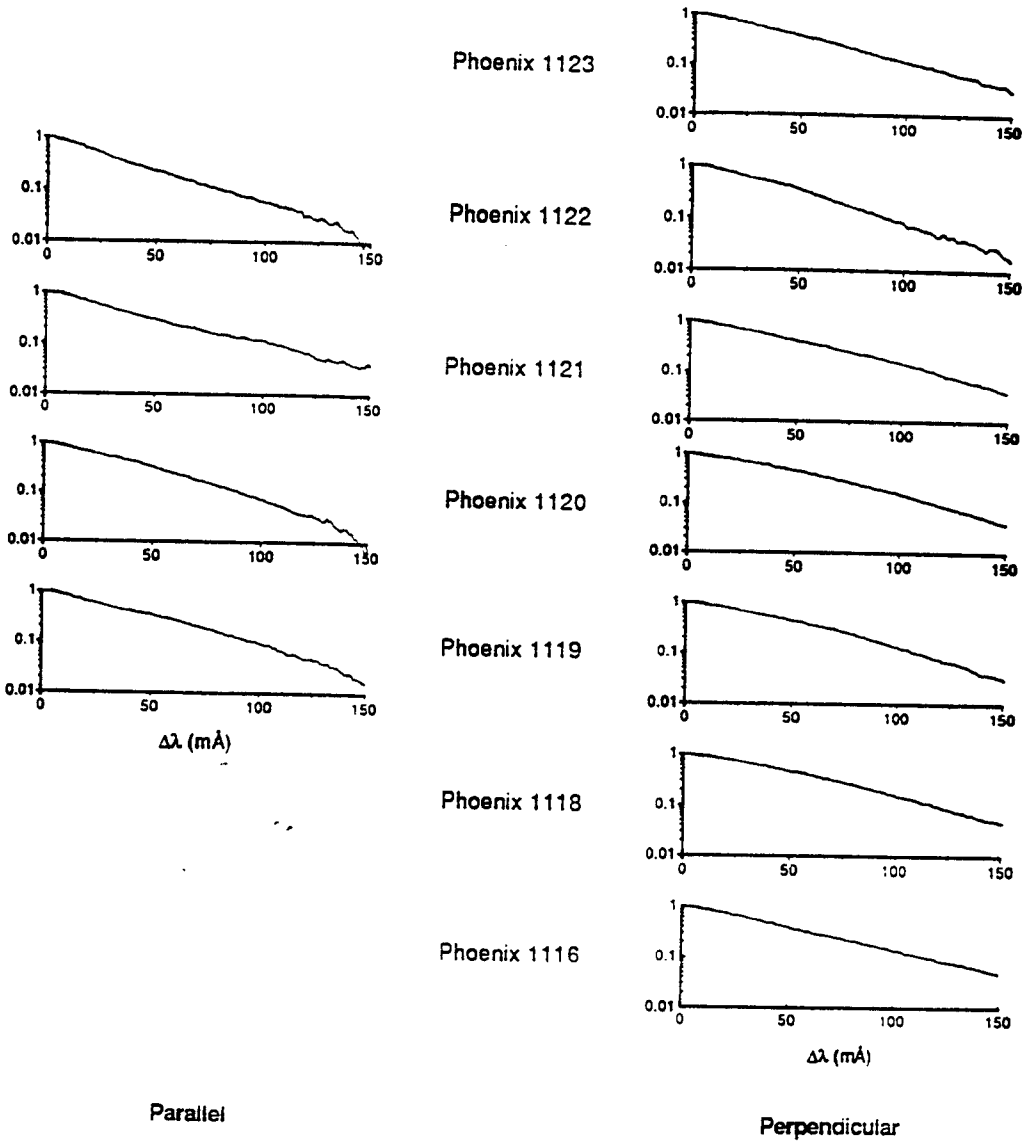

Figure 4-15. Plots of log intensity vs. $\Delta\lambda$ (mÅ) for the L_β lines.

reduced L_γ search of the wings were: $C = 0.02 - 0.20$, $g = 0.3 - 2.5$, $\varepsilon = 1 - 2.5$, $z = 1 - 5$. These results show agreement with the results obtained from the reduced search of the L_β lines.

The additional constraints needed in the full model can be provided by having the model fit multiple lines with the same parameters. The flat crystal spectrograph provided the data for which this was done.

4.5 Plasma Parameters from Flat Crystal Spectrometer Profiles.

Figure 4-16 shows the spectra obtained for the flat crystal spectrograph at the Phoenix PRS. The search for the model parameters which would reproduce the lines was carried out in the same manner as for the Johann spectrometer data. The additional constraint in the search was that the same parameters had to produce all of the lines in the spectra. However, opacity was only applied to the L_γ line, since opacity decreases rapidly along the spectral series. The central parts of the lines were used for the search, since there is an overlap in the wings of the lines of the flat crystal spectra. By fitting only the central part of the lines, many solutions were found. The criteria used to determine if the found profiles were acceptable was that the region of the overlapping lines between L_δ and L_ε had to match the experimental profile. The fits which contained the three lines L_γ, L_δ and L_ε were the only ones which led to a unique set of parameters and this resulted only for the baseline raised 5% from the best guess baselines given in Figure 4-16. The two spectra which contained these three lines were shot number 1116 and shot number 1120.

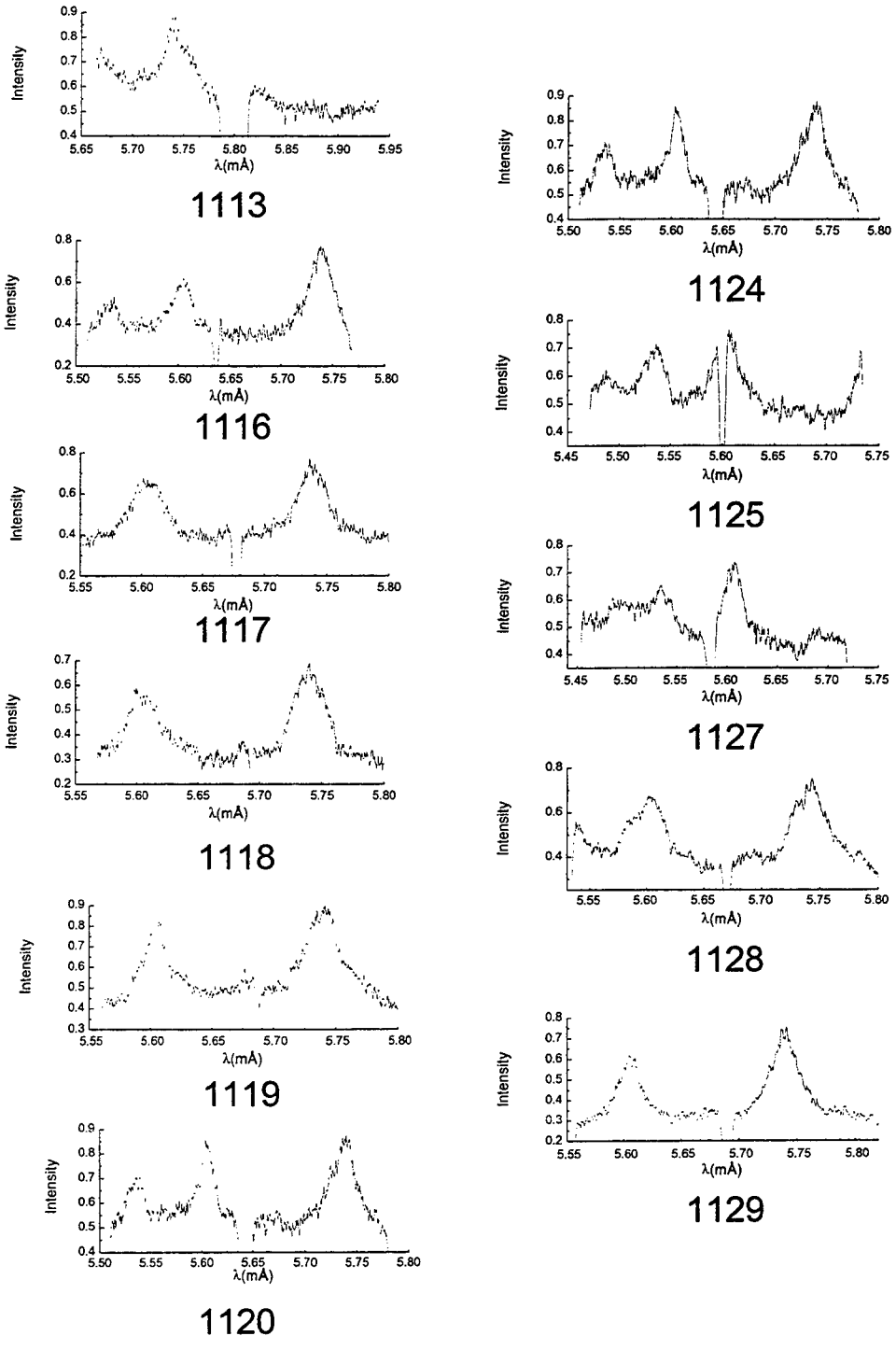

Figure 4-16. Flat crystal spectra.

A best fit for the model parameters in shot number 1116 was found to be b = 1.5 - 2.5, C = 0.01 - 0.4, g = 0.5 - 1.5, ε = 0.1 - 2.5, z = 1 - 4.5, and t = 0.7 - 1.8 and a best fit for the model parameters in shot number 1120 was found to be b = 0.9 - 2, C = 0.01 - 0.2, g = 0.7 - 2, ε = 0.05 - 1.7, z = 1- 5, and t = 1.5 - 4.5. The experimental spectra for shot number 1116 and 1120 are shown in Figure 4-17 (a) and (b) with one set of parameters which fit the spectra. From the fits of the L_β, L_γ and flat crystal profiles the parameters in the Phoenix source were consolidated.

4.6 Interpretation of the Plasma Parameters Found.

The parameter b was found to be approximately 1.0 - 2.5. This corresponds to a bulk plasma velocity of 3.0 - 7.5 x 10^7 cm / s. This result is reasonable since velocities of this order have been observed on many other similar z-pinch devices.[8]

The parameter C was found to have values from 0.01 to 0.40. This corresponds to a reasonable electron density of 0.3 - 6 x 10^{21} cm^{-3}.

The parameter g = 0.5 to 2.5 corresponds to a power spectrum with a width ranging from 0.25 ω_{pe} to 1.25 ω_{pe}. Values of g higher than 2.5 were excluded, since this corresponds to a width greater than the plasma frequency, and is not physical.

The value ε obtained from the Johann spectrometers for the L_β and L_γ profiles was 1 - 2.5 and the value of ε obtained from the flat crystal spectrograph for the L_γ, L_δ, and L_ε profiles was 0.05 - 2.5. The actual value of ε is probably somewhere between these two results in the range 1 - 2, since there is some uncertainty associated with each of these two results. The uncertainty in the results from the Johann spectrometers comes from

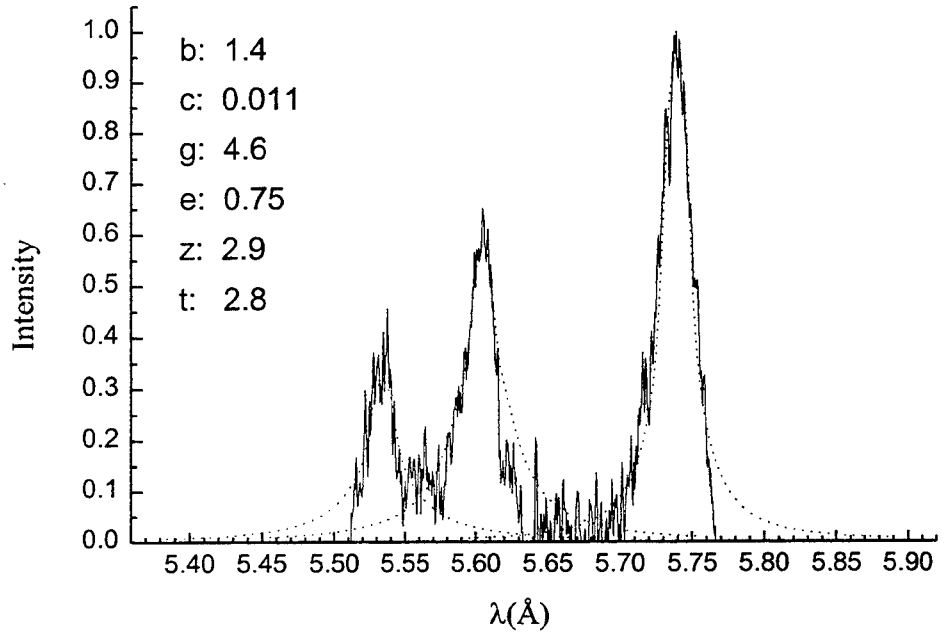

(a) Shot number 1116

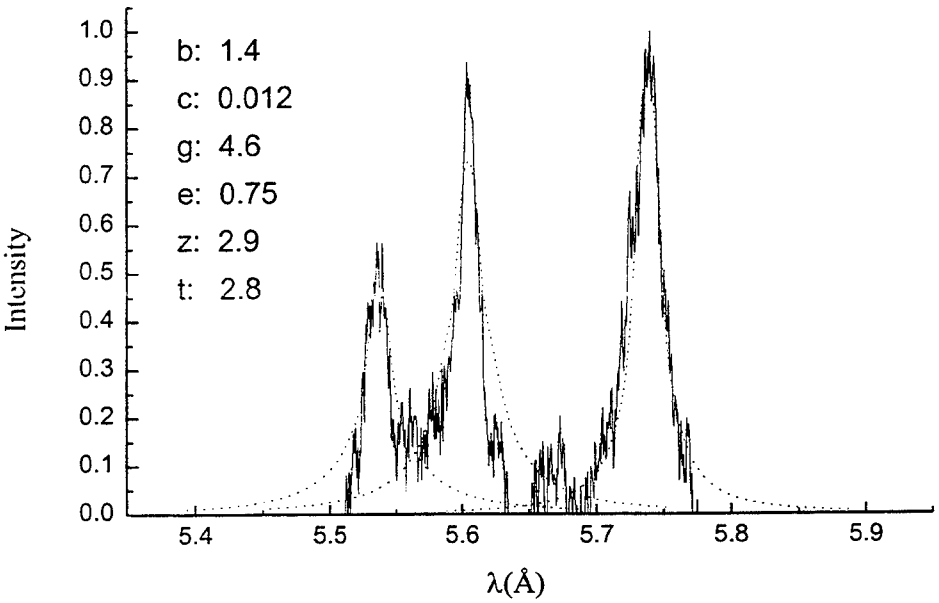

(b) Shot number 1120

Figure 4-17. Fit of flat crystal spectrometer data.

using a reduced parameter set to obtain an estimate of ε, while the uncertainty in the results from the flat crystal spectrometer comes from the inherent low resolution of the spectrometer. The values of ε = 1 - 2 and C = .01 - 0.4 correspond to an oscillatory electric field of $E_0 \approx 1$ - 9 GV / cm. These values for the oscillating electric fields are reasonable in terms of energy considerations. The energy density in the electric fields of $E_0^2 / 16\pi$ was compared to the thermal energy density $N_e T$ and the kinetic energy density $KE = (3N_i v_{ni}^2) / 2$ in the plasma. The energy density of the oscillations were found to be approximately 0.5 - 4 times that of the thermal energy density, by assuming an electron temperature from 500 keV to 1000 keV. The high end values of this ratio seem physically improbable. Because the waves have an energy density comparable to the thermal energy density, there is a strong Langmuir turbulence. The ratio of the energy density of the oscillations to the kinetic energy density varies from 0.01 to 0.3, indicating that the energy density balance was not violated.

The parameter z = 1 - 5 corresponds to an anisotropy of the electric field with the greatest field strength along the direction of the bulk current. This agrees with the theory which suggests that these anomalous electric fields are produced by runaway electrons in the discharge. The runaway electrons are expected to be predominantly along the direction of the bulk current.[34]

The parameter t showed a variation from 1 and 3 for the L_β line and 0.5 to 2 in the flat crystal results for the L_γ line. These are reasonable optical depths for the L_β and L_γ lines.

SECTION 5
DISCUSIONS AND CONCLUSIONS

By using several spectrometers we were able to measure the level and angular distribution of oscillating electric fields in a superdense plasma produced on the Phoenix device. Since the energy density in these fields is on the order of the thermal energy density, this suggests that these oscillations may lead to the instability which prevents the highest ionization states of higher Z elements from being reached in plasma radiation sources. Further experiments, using more sophisticated designs are necessary to determine the field values more accurately.

There are several improvements which can be made to measure the two states of polarization of a line profile. One of the problems encountered on the Phoenix experiment was that the two Johann spectrometers were not guaranteed to be looking at the same part of the plasma. This resulted from the extension of the source along the wires and the placement of the spectrometers on opposite sides of the source.

The difficulty of having an extended source is that the resulting spectra is an average over the length of the source. A point source is necessary to measure spectra in two states of polarization from a localized region of the plasma.

The problem associated with the location of the spectrometers could be resolved if both states of polarization could be extracted from the same line of sight to the plasma.

For a point source, such a spectrometer can be designed by using a thin flat crystal as a kind of beam splitter as shown in Figure 5-1. In the ideal case, if a crystal which leads to a Bragg angle of 45° can be found, for the desired wavelength, and can be made thin enough so that enough radiation can pass through, then a spectrometer which completely polarizes the x rays can be made. Figure C-3. shows the calculation of transmission and reflection of 6.053 Å, for two states of polarization at 45.3°, for thin crystals of N layers of quartz $10\underline{1}0$. These curves show that at 45° the π polarization is not reflected with any significant intensity. More importantly, the π component is transmitted without any difference than that for bulk material absorption. This means if we set the thin crystal A close to 45°, such that only the σ component is reflected, then we can use a second crystal B, also oriented at 45°, but in the opposite state of polarization, to Bragg reflect the π component that passed through the thin crystal A. In doing so, we then have extracted both components of polarization from the same line of sight. In practice however, it will not always be possible to find a crystal with the correct 2d value which can be cleaved thin enough to transmit sufficient radiation at the desired wavelength, especially for longer wavelengths where absorption coefficients are large.

Even if we cannot find a thin crystal A, which results in a Bragg angle at 45°, we can still measure the profiles in two states of polarization if we can find a thin enough crystal (A) where the Bragg angle results in a difference in the amount of radiation reflected for the π and σ components. From calculations of thin crystals, we know the amount of the π and σ components that will be reflected from the thin crystal into the first detector. The

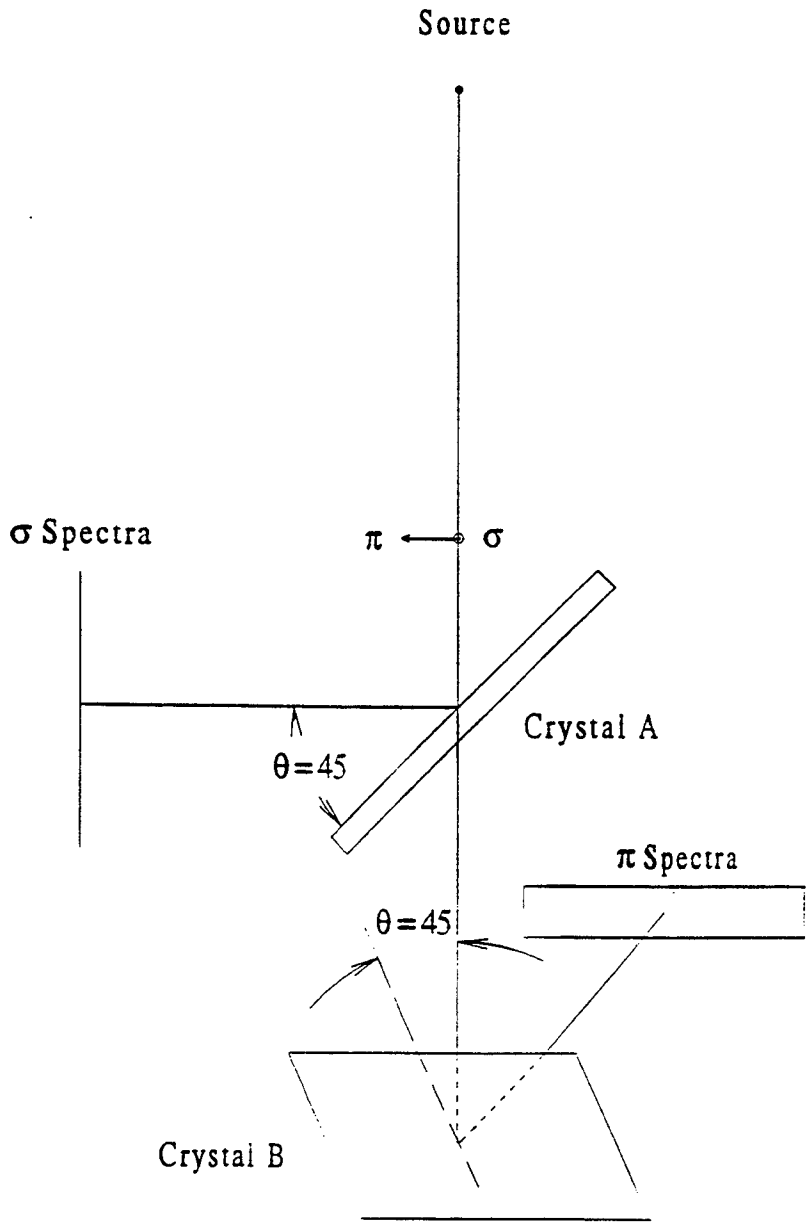

Figure 5-1. Single line of sight polarizing spectrometer

radiation passing through the crystal will still be unpolarized for the most part. The second crystal B must still have a Bragg angle close to 45° so that only one state of polarization makes it to the second detector. By knowing the relative ratio of reflected intensities for crystal A and having a spectra in one polarization, the σ and π spectra can be extracted.

In addition to improving the geometry of the spectrometers, it would also be desirable to have time resolved spectra. This could be achieved by using x-ray streak cameras for the detectors. The one disadvantage, however, of using streak cameras is the reduction of detector resolution. Still, spectral profiles at various stages of the pinch event would provide detailed information about the time evolution of the plasma.

It would also be desirable to have a high resolution spectrometer to look at the Lyman lines, instead of the flat crystal spectrometer used in this experiment. A Johann type spectrometer could be used in place of the flat crystal spectrometer. With a higher resolution spectra of the Lyman series, the parameters in the plasma could be determined with more accuracy.

In addition to the improvements made to the spectrometers, several improvements can be made to the other diagnostics used on the Phoenix source. Several improvements for measuring the size of pinch can be made on the pinhole camera. First, it is necessary to use smaller pinholes in the camera. This would bring the resolution up high enough so that the pinches could be resolved. In addition to using smaller pinholes it is also necessary to determine the optimum filters for the cameras. As we saw from the pinhole

pictures on the Phoenix experiment, if too little filtration was used, the pictures became saturated. Ideally the intensity of the source should be calibrated using known filter thicknesses. This would require being able to get an absolute optical density from a few pictures with known filters in place. A starting point for changing filters and pinhole sizes would then be established. It would also be ideal to use pinholes made out of a high *Z* material, like platinum, to prevent radiation from passing through the pinhole substrate. These improvements would lead to the best results for pinch size determination using a pinhole camera.

The suggested improvements on the regular pinhole camera can also be made to the four frame camera. In addition to using smaller pinholes and the appropriate filtration, the intensity at the camera has to be maintained, since each frame of the camera is only open for several nanoseconds. The intensity at the detector can be increased, to offset the reduction in intensity from using smaller pinholes by moving the camera closer to the source. With the correct pinholes, filters, and intensity at the detector, many shots would then have to be made to get enough information to determine the size of the pinches. Pictures would also have to be taken at several places in the radiation pulse to ensure the smallest pinches are observed.

With these improvements to the diagnostics, a better understanding of superdense plasmas like the Phoenix device could be achieved and this could lead to improved performance of pulsed radiation sources.

SECTION 6
REFERENCES

1. E. Oks, Plasma Spectroscopy: The Influence of Microwave and Laser Fields, Springer Ser. Atoms and Plasmas, (Springer-Verlag, Berlin, Heidelberg, 1995) Chp. 3. (Unclassified)

2. E. Oks, Plasma Spectroscopy: The Influence of Microwave and Laser Fields, Springer Ser. Atoms and Plasmas, (Springer-Verlag, Berlin, Heidelberg, 1995) Chp. 7 and references therein. (Unclassified)

3. J. D. Huba, NRL Plasma Formulary, (Naval Research Laboratory, Washington, (1994). (Unclassified)

4. R. G. Breene Jr., Rev. Mod. Phys. **29**(1), 94-143 (1957). (Unclassified)

5. Hans R. Griem, Plasma Spectroscopy, (McGraw-Hill, New York, 1964). (Unclassified)

6. R. J. Armstrong, and D. S. Darrow, *Nuclear Fusion* **34**(11), 1532-1537 (1994). (Unclassified)

7. C. Boucher et. al., *Journal of Nuclear Materials* 176 & 177, 1050-1054 (1990). (Unclassified)

8. A. Schulz, Ph.D. Dissertation, Bochum University, Germany (1992). (Unclassified)

9. H. A. Bethe and E. E. Salpeter, Quantum Mechanics of One-and Two-Electron Atoms, (Academic Press Inc., New York, 1957). (Unclassified)

10. L. D. Landau and E. M. Lifshitz, Quantum Mechanics, (Pergamon Press, Oxford, 1977). (Unclassified)

11. L. I. Schiff, Quantum Mechanics, (McGraw-Hill, New York, 1968). (Unclassified)

12. B. H. Brandsden and C. J. Joachain, Introduction to Quantum Mechanics, (Longman Scientific & Technical, New York, 1989). (Unclassified)

13. M. Barranger, *Physical Review* **111**(2), 481-493. (Unclassified)

14. V. Weisskopf, *Z. Phys.* **25,** 287 (1932). (Unclassified)

15. V. S. Lisitsa, *Sov. Phys. Usp.* **20**(7), 603 (1977). (Unclassified)

16. Hans R. Griem, Spectral Line Broadening by Plasmas, (Academic Press, New York, 1972). (Unclassified)

17. J. Holtsmark, *Ann. Phys.* **58**, 577 (1919). (Unclassified)

18. I. I. Sobelman, Introduction to the Theory of Atomic Spectra, (Paragon Press, New York, 1972), p. 387. (Unclassified)

19. I. I. Sobleman, L. A. Vainshtein and E. K. Yukov, Excitation of Atoms and Broadening of Spectral Lines, Springer Ser. Chem. Phys. (Springer, Berslin Heidelberg, 1981), Chap. 7. (Unclassified)

20. H. M. Foley, *Physical Review* **69**(11,12), 616-628 (1946). (Unclassified)

21. F. F. Chen, Introduction to Plasma Physics and Controlled Fusion, (Plenum Press, New York and London, 1984), pp. 179-181. (Unclassified)

22. D. I. Blochinzew, *Phys. Z. Sow. Union* **4**, 501 (1933). (Unclassified)

23. E. Oks, Plasma Spectroscopy: The Influence of Microwave and Laser Fields, Springer Ser. Atoms and Plasmas,(Springer-Verlag, Berlin Heidelberg, 1995), p. 3. (Unclassified)

24. J. W. Strutt and B. Rayleigh, The Theory of Sound, (Dover, New York, 1945) p. 38. (Unclassified)

25. J. Richter, In: Plasma Diagnostics, Ed. W Lochte-Kotgreven, (North-Holland, Amsterdam, 1968), pp. 1-65. (Unclassified)

26. R. E. Terry et. al., A Detailed Characterization of Power Flow and PRS Performance on Phoenix, (Naval Research Laboratory, 1996) NRL/MR/6720-7812. (Unclassified)

27. International Tables for X-ray Crystallography, (The Kynoch Press, Birmingham, England 1962), Vol. III, pp. 157. (Unclassified)

28. R. Jenkins, and J. L. de Vries, Worked Examples in X-ray Analysis, (Springer-Verlag, New York, 1970). (Unclassified)

29. J. L. Wiza, Microchannel Plate Detectors, Galileo Electro-Optics Corp. (Unclassified)

30. J. L. Jones, K. W. Paschen, and J. B. Nicholson, *Applied Optics* **2**(9), 955 (1963)

31. Shigeru Morita, Ph.D. Dissertation, Institute of Plasma Physics, Nagoya University, Japan (1983). (Unclassified)

32. W. Press, S. Teukolsky, W. Vetterling, and B. Flannery, Numerical Recipes in C, (Cambridge University Press, New York, 1992), p. 311. (Unclassified)

33. Clothiaux et. al., *Journal of Quantitative Spectroscopy and Radiative Transfer*, Accepted, (1997). (Unclassified)

34. P. A. Robinson and D. L. Newman, *Phys Fluids B* **2**(12), 3120 (1990). (Unclassified)

35. B. L. Henke, E. M. Gulllikson, and J. C. Davis, *Atomic Data and Nuclear Data Tables* **54**, 181-342 (1993). (Unclassified)

36. M. L. Iosifovich, Handbook of X-ray analysis of polycrystalline materials, (Consultants Bureau, New York, 1964), pp. 326-327. (Unclassified)

37. N. G. Alexandropoulos, and G. G. Cohen, *Applied Spectroscopy* **28**(2), 155-164 (1974). (Unclassified)

38. R. W. G. Wyckoff, Crystal Structures, (Interscience Publishers, New York, 1963). (Unclassified)

39. E. A. Wood, Crystal Orientation Manual, (Colombia University Press, New York and London, 1963). (Unclassified)

40. H. Dumont and P. Troussel, *Rev. Sci. Instrum.* **62**(7), 1749-1753 (1991). (Unclassified)

APPENDIX A
CONVOLUTION OF LINE PROFILES

A.1 CONVOLUTION OF DOPPLER, HOLTSMARK AND LORENTZ PROFILES.

To arrive at the convolution of the Doppler, Holtsmark, and Lorentz profiles we first convolute the Doppler and Holtsmark profiles and then convolute the result with the Lorentz profile.

A.1.1 Convolution of the Gaussian and Holtsmark Profiles.

We are first interested in convoluting the Doppler profile given by

$$G(u) = \frac{\alpha}{\sqrt{\pi}} e^{-\alpha^2 u^2} \tag{A.1}$$

with the normalized Holtsmark profile in wavelength given by

$$W_H(v) = \frac{\beta^2 v}{\pi} \int_0^\infty e^{-y^{3/2}} y \sin(\beta v y) dy$$

$$= \mathrm{Re}\left[\frac{i\beta^2 v}{\pi} \int_0^\infty e^{-y^{3/2}} e^{-i\beta v y} y dy \right]. \tag{A.2}$$

The convolution of these two profiles is obtained from

$$I_{GH}(x) = \int_{-\infty}^{\infty} G(z) W_H(x-z) dz = \mathrm{Re} \frac{\beta^2 \alpha i}{2\pi^{2/3}} x \int_{-\infty}^{\infty} y e^{-y^{\frac{3}{2}} - i\beta x y} dy \int_{-\infty}^{\infty} (x-z) e^{-\alpha^2 z^2 + i\beta z y} dz . \tag{A.3}$$

Performing the integration in z using

$$\int_{-\infty}^{\infty} e^{-(az^2+bz)}dz = \sqrt{\frac{\pi}{a}}e^{\frac{b^2}{4a}} \tag{A.4}$$

and

$$\int_{-\infty}^{\infty} ze^{-az^2+bz}dz = \frac{b}{2a}\sqrt{\frac{\pi}{a}}e^{\frac{b^2}{4a}}, \tag{A.5}$$

we arrive at

$$I_{GH}(x) = \mathrm{Re}\frac{\beta^2\alpha i}{2\pi^{2/3}}\int_{-\infty}^{\infty} ye^{-|y|^{\frac{3}{2}}-i\beta xy}dy\left(x\frac{\sqrt{\pi}}{\alpha}-\frac{i\beta y}{2\alpha^2}\frac{\sqrt{\pi}}{\alpha}\right)e^{-\frac{\beta^2y^2}{4\alpha^2}}$$

$$= \mathrm{Re}\frac{\beta^2}{2\pi}\int_{-\infty}^{\infty} ye^{-|y|^{\frac{3}{2}}-\frac{\beta^2y^2}{4\alpha^2}}i\left(x-\frac{i\beta y}{2\alpha^2}\right)e^{-i\beta xy}dy. \tag{A.6}$$

With

$$ie^{-i\beta xy} = \sin(\beta xy) + i\cos(\beta xy),$$

$$\mathrm{Re}\left[\left(x-\frac{i\beta y}{2\alpha^2}\right)ie^{-i\beta xy}\right] = x\sin(\beta xy) + \frac{\beta y}{2\alpha^2}\cos(\beta xy), \tag{A.7}$$

and the final expression for the integral simplifies to

$$I_{GH}(x) = \frac{\beta^2}{\pi}\int_0^{\infty} ye^{-y^{\frac{3}{2}}-\frac{\beta^2y^2}{4\alpha^2}}\left(x\sin(\beta xy)+\frac{i\beta y}{2\alpha^2}\cos(\beta xy)\right)dy. \tag{A.8}$$

A.1.2 Convolution of the Gauss-Holtsmark and Lorentz Profiles

Once we have the convolution of the Gaussian and Holtsmark profiles we need to convolute this profile with the Lorentz profile given by

$$L(x) = \frac{\delta}{\pi}\frac{1}{x^2+\delta^2}. \tag{A.9}$$

The convolution of these profiles is obtained from

$$I_{GHL}(x) = \int_{-\infty}^{\infty} I_{GH}(z)L(x-z)dz$$

$$= \mathrm{Re}\frac{\delta}{\pi}\frac{\beta^2 i}{2\pi}\int_{-\infty}^{\infty}\int_{-\infty}^{\infty} e^{-y^{\frac{3}{2}}-i\beta zy-\frac{\beta^2y^2}{4\alpha^2}}\left(z-\frac{i\beta y}{2\alpha^2}\right)ydy\frac{1}{(x-z)^2+\delta^2}dz. \tag{A.10}$$

Making the substitution

$$\frac{1}{(x-z)^2+\delta^2} = \frac{1}{2i\delta}\left[\frac{1}{z-(x+i\delta)}-\frac{1}{z-(x-i\delta)}\right], \tag{A.11}$$

the integral becomes

$$I_{GHL}(x) = \mathrm{Re}\frac{\beta^2}{2\pi^2}\int_{-\infty}^{\infty} ye^{-y^{\frac{3}{2}}-\frac{\beta^2y^2}{4\alpha^2}}dy\int_{-\infty}^{\infty} e^{-i\beta zy}\left(z-\frac{i\beta y}{2\alpha^2}\right)\left[\frac{1}{z-(x+i\delta)}-\frac{1}{z-(x-i\delta)}\right]dz. \tag{A.12}$$

Breaking the integral into positive and negative intervals of y we obtain

$$I_{GHZ}(x) = \mathrm{Re}\frac{\beta^2}{2\pi^2}\int_{0}^{\infty} ye^{-y^{\frac{3}{2}}-\frac{\beta^2y^2}{4\alpha^2}}dy\int_{-\infty}^{\infty} e^{-i\beta zy}\left(z-\frac{i\beta y}{2\alpha^2}\right)\left[\frac{1}{z-(x+i\delta)}-\frac{1}{z-(x-i\delta)}\right]dz$$

$$+\mathrm{Re}\frac{\beta^2}{2\pi^2}\int_{-\infty}^{0} ye^{-y^{\frac{3}{2}}-\frac{\beta^2y^2}{4\alpha^2}}dy\int_{-\infty}^{\infty} e^{-i\beta zy}\left(z-\frac{i\beta y}{2\alpha^2}\right)\left[\frac{1}{z-(x+i\delta)}-\frac{1}{z-(x-i\delta)}\right]dz. \tag{A.13}$$

The integrals in z both contain two poles. We must choose the contours correctly such that the part of contour off of the real axes vanishes as z goes to $\pm\infty$. For $y > 0$ we have to make the integration with the imaginary part of z negative. For $y < 0$ we have to use a positive value for z. Applying the residue theorem, the integral becomes

$$I_{GHL}(x) = \mathrm{Re}\frac{\beta^2\pi i}{2\pi^2}\int_0^{\infty} y e^{-iy^{\frac{3}{2}}-\frac{\beta^2 y^2}{4\alpha^2}} e^{-i\beta(x-i\delta)y}\left((x-i\delta)-\frac{i\beta y}{2\alpha^2}\right)dy$$

$$+\mathrm{Re}\frac{\beta^2\pi i}{2\pi^2}\int_{-\infty}^{0} y e^{-iy^{\frac{3}{2}}-\frac{\beta^2 y^2}{4\alpha^2}} e^{-i\beta(x+i\delta)y}\left((x+i\delta)-\frac{i\beta y}{2\alpha^2}\right)dy. \qquad \text{(A.14)}$$

The sign of the first term is positive because a minus sign is picked up by the direction of the contour. Reversing the limits of integration and letting y become $-y$ in the second integral we have

$$I_{GHL}(x) = \mathrm{Re}\frac{\beta^2 i}{2\pi}\int_0^{\infty} y e^{-iy^{\frac{3}{2}}-\frac{\beta^2 y^2}{4\alpha^2}} e^{-i\beta(x-i\delta)y}\left((x-i\delta)-\frac{i\beta y}{2\alpha^2}\right)dy$$

$$+\mathrm{Re}\frac{\beta^2 i}{2\pi}(-)\int_0^{\infty}(-y)e^{-(-y)^{\frac{3}{2}}-\frac{\beta^2 y^2}{4\alpha^2}} e^{-i\beta(x+i\delta)(-y)}\left((x+i\delta)-\frac{i\beta(-y)}{2\alpha^2}\right)d(-y)$$

$$= \mathrm{Re}\frac{\beta^2 i}{2\pi}\int_0^{\infty} y e^{-y^{\frac{3}{2}}-\frac{\beta^2 y^2}{4\alpha^2}-\beta\delta y}\left[e^{-i\beta xy}\left((x-i\delta)-\frac{i\beta y}{2\alpha^2}\right)-e^{i\beta xy}\left((x+i\delta)+\frac{i\beta y}{2\alpha^2}\right)\right]dy. \qquad \text{(A.15)}$$

Putting the exponential back in terms of sin and cosine and taking the real part we arrive at the final integral for the profile

$$I_{GHL}(x) = \frac{\beta^2}{\pi}\int_0^{\infty} y e^{-y^{\frac{3}{2}}-\frac{\beta^2 y^2}{4\alpha^2}-\beta\delta y}\left[x\sin(\beta xy)+\left(\delta+\frac{\beta y}{2\alpha^2}\right)\cos(\beta xy)\right]dy. \qquad \text{(A.16)}$$

APPENDIX B
DISPERSION OF FLAT CRYSTAL SPECTROMETER

B.1 CALCULATION OF DISPERSION FOR THE AUBURN FLAT CRYSTAL SPECTROMETER

To calculate the dispersion $\lambda(x)$ on the film for the flat crystal spectrometer, we need to define some physical dimensions for the spectrometer. The setup for the Auburn flat crystal spectrometer is shown in Figure 3-13. We take the distance from the crystal to the source to be U and the distance from the center of the two crystals to the film plane to be V. The flat crystals are set to an angle α relative to the source. With these parameters defined we can use geometry to find the dispersion.

To begin, we find the wavelength λ of the source that will satisfy Bragg's law a distance h from the center of the two crystals. From the law of sines, the angle β that a ray makes a distance h from the center of the crystals is given by

$$\beta = \sin^{-1}\left[\frac{U\sin(\alpha)}{\sqrt{U^2 + h^2 + 2hU\cos(\alpha)}}\right]. \tag{B.1}$$

From Bragg's Law, $\lambda = 2d\sin\beta$, we find the wavelength λ that corresponds to this angle is

$$\lambda = \frac{(2d)U\sin(\alpha)}{\sqrt{U^2 + h^2 + 2hU\cos(\alpha)}}. \tag{B.2}$$

Solving for h we get

$$h = -U\cos(\alpha) \pm U\sqrt{\cos^2(\alpha) + \left[\frac{2d\sin(\alpha)}{\lambda}\right]^2 - 1}\,. \tag{B.3}$$

We take the positive solution, since the negative root corresponds to the same Bragg angle but on the opposite side of the normal that we are interested in.

We can now proceed to find $x(\lambda)$ by finding the intersection of the Bragg reflected ray from the crystal and the line of the film. The equation for the line of the ray is given by

$$Y_R = mX_R + b\,, \tag{B.4}$$

where the slope m is

$$m = \tan(\alpha + \beta)\,. \tag{B.5}$$

The y-intercept b can be found since we know that the point

$$Y_R = h\sin(\alpha) \quad X_R = h\cos(\alpha) \tag{B.6}$$

lies on the reflected line. Solving for b and plugging it back into Eq. (B.4) we have

$$Y_R = \tan(\alpha + \beta)X_R + h[\sin(\alpha) - \tan(\alpha + \beta)\cos(\alpha)]\,. \tag{B.7}$$

This line intersects the film when $Y_R = V$. Plugging V in for Y_R in Eq. (B.3) and solving for X_R we get

$$X_R = h\cos(\alpha) + \frac{V - y\sin(\alpha)}{\tan(\alpha + \beta)}\,. \tag{B.8}$$

$x(\lambda)$ can then be found by putting in Eq. (B.1) for h, that is

$$x(\lambda) = U\cos(\alpha)\xi + \frac{V - U\xi\sin(\alpha)}{\tan(\alpha + \beta)} \tag{B.9}$$

where

$$\xi = \left[-\cos(\alpha) + \sin(\alpha)\sqrt{\frac{(2d)^2}{\lambda^2} - 1} \right] \tag{B.10}$$

and

$$\beta = \sin^{-1}\left[\frac{\sin(\alpha)}{\sqrt{\xi^2 + 1 + 2\xi\cos(\alpha)}} \right]. \tag{B.11}$$

To find $\lambda(x)$, the expression for $x(\lambda)$ is most easily inverted numerically.

APPENDIX C
POLARIZATION BY CRYSTALS

C.1 POLARIZATION CALCULATIONS FOR REFLECTION FROM SEMI-INFINITE CRYSTALS.

To properly design spectrographs that are capable of distinguishing between states of polarization it is necessary to understand how x rays are polarized under Bragg reflection from crystals. The problem of x ray scattering from crystals is treated in detail by Henke et. al using modified Darwin Prin theory.[35] The calculations based on the MDP theory will be summarized and applied here to the quartz crystals used in the experiment. From MDP theory the reflected intensity for a semi-infinite crystal is given by

$$\frac{I}{I_0} = \left| \frac{-sP(2\theta)}{(\sigma+\varepsilon) \pm \sqrt{(\sigma+\varepsilon)^2 - ks\bar{s}[P(2\theta)]^2}} \right|^2 . \tag{C.1}$$

The parameters s and σ are defined such that the fractional reflected amplitude is *-is* and the fractional transmitted amplitude is 1-*i*σ as shown in Figure C-1. s and σ can be calculated by

$$s = -r_0 \lambda \frac{MF_1(\theta) + iMF_2(\theta)}{\sin\theta} \tag{C.2}$$

and

$$\sigma = -r_0 \lambda \frac{MF_1(0) + iMF_2(0)}{\sin\theta}, \tag{C.3}$$

where

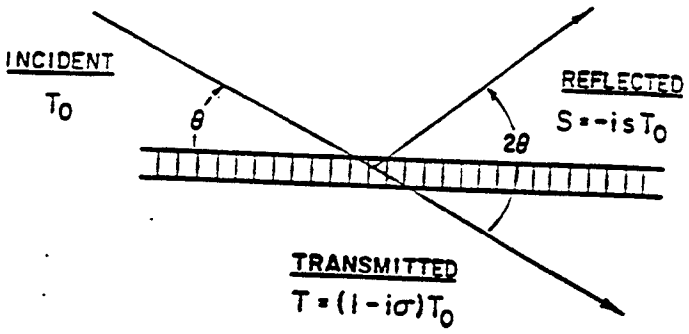

(a) Scattering parameters s and σ.

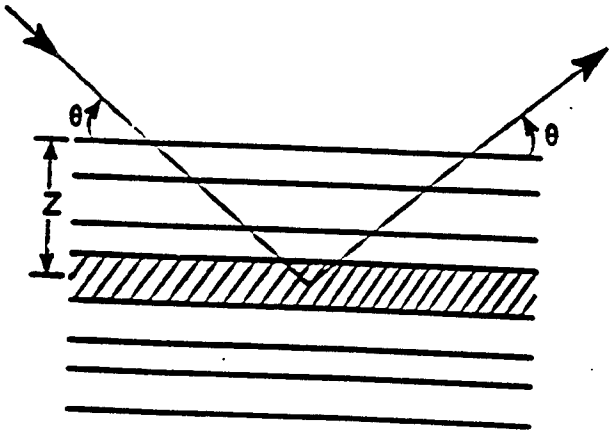

(b) A ray being scattered a distance z from the scattering plane.

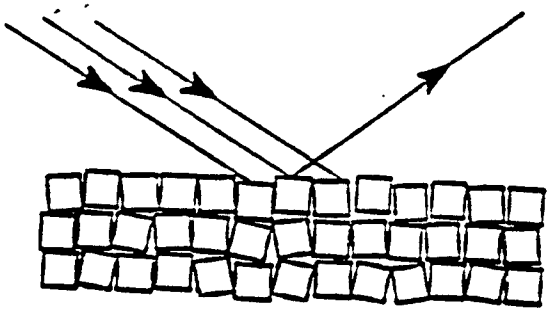

(c) Scattering from a mosaic crystal.

Figure C-1. Details of a scattering process.

$$MF(\theta) = \sum_q m_q f_q \exp\left(\frac{i4\pi z_q \sin\theta}{\lambda}\right) \tag{C.4}$$

is the number of unit cells per unit area M multiplied by the average structure factor F of the unit cell. The average structure factor F is calculated by averaging the contributions of the x rays scattered from each atom in the unit cell. The quantity m_q is the number of atoms of type q that are a distance z_q from the reference plane of scattering as per Figure C-1. The scattering from each type of atom is given by an atomic scattering factor

$$f = f_1(0) + if_2(0) - \Delta f(\theta), \tag{C.5}$$

which has an angle independent part described by scattering in the forward direction and an angle dependent correction term $\Delta f(\theta)$ due to the interference affects of waves scattered from different parts of the atom. The angle independent scattering is primarily due to photoabsorption and Compton scattering. The angle dependent correction term is given by

$$\Delta f(\theta) = Z - f_o \tag{C.6}$$

where f_o is the atomic scattering factor which depends on $sin\theta / \lambda$. The atomic scattering factors for atoms can be found in tables.[36]

The factor ε , given by

$$\varepsilon = \frac{2\pi d \sin\theta}{\lambda} - m\pi, \tag{C.7}$$

represents the phase difference from the phase required for the m^{th} order reflection. Order $m = 0$ corresponds to non Bragg reflection, $m = 1$ to 1st order Bragg reflection, etc.

The polarization factor $P(2\theta)$ for the incident radiation is given by 1 for the σ polarization and $cos(2\theta)$ for the π polarization. σ is the polarization with the electric field perpendicular to the plane of incidence and π is the component with polarization parallel to the plane of incidence.

A factor k is introduced to take into account the quality of the crystal. In many crystals there can be a misorientation of "crystal segments" as illustrated in Figure C-1. A value of $k = 0$ corresponds to a mosaic crystal and a value of $k = 1$ corresponds to a perfect crystal. Since quartz is nearly a perfect crystal, in all successive calculations involving quartz, k will be taken to be unity.[37]

The use of Modified Darwin Prin theory for calculating reflectivities is applicable only for $\theta > \theta_c$ where

$$\theta_c \approx 3\lambda\sqrt{\frac{MF_1(0)}{2\pi d}} . \qquad \text{(C.8)}$$

When the angle is smaller than this critical angle, the Optical Electromagnetic Model must be used. This consists of defining a complex index of refraction in terms of s and σ and solving the Fresnel equations.

C.1.1 POLARIZATION OF X RAYS FROM QUARTZ $10\underline{1}0$ IN BRAGG REFLECTION.

To show a sample of how MDP theory was used to find the relative reflectivity of the σ and π components for the crystals used in the experiment, we calculate the reflection of 6.053Å from the $10\underline{1}0$ plane of quartz $(SiO_2)_3$ under Bragg reflection.

Quartz has a hexagonal structure with the dimensions of the unit cell given by

$$a_o = 4.913\,\mathring{A} \quad c = 5.4\,\mathring{A}. \tag{C.9}$$

The 2d spacing in quartz for the $10\underline{1}0$ plane is 8.51 Å and the critical cutoff angle for using MDP theory is $\theta_c = 0.86^o$. The position of the atoms in the unit cell of quartz given by Wychoff are[38]

Si:	-0.465, -0.465, 0.333	0.465, 0.000, 0.000	0.000, 0.465, 0.670
O:	0.415, 0.272, 0.120	-0.143, 0.415, 0.455	-0.272, 0.143, 0.787
	0.143, -0.272, -0.120	0.272, 0.415, 0.0055	0.415, -0.143, 0.215

The reflectivity for a crystal is obtained from integrating the rocking curve given by Eq. (C.1). The rocking curve is the reflected intensity *I*, as a function of the angle θ, for a given wavelength. In order to calculate the rocking curve for quartz, we have to first compute *MF(0)* and *MF(θ)* for quartz using Eq. (C.4).

In general, the distance z_q of an atom in the unit cell from the plane of scattering is calculated by its miller indices *h, k,* and *l* using $z_q / d = hx_q + ky_q + lz_q$, but since the $10\underline{1}0$ plane of quartz corresponds to planes perpendicular to the *x* axes, z_q in the expression for *MF* is simply given by the *x* position of the atom in the unit cell. A further simplification arises in calculating *MF* for quartz because the atoms in the unit cell are symmetric about $x = 0$. This allows us to simplify the expression for *MF* to

$$MF(\theta) = M\sum_q g_q f_q \cos\left(\frac{4\pi z_q}{\lambda}\sin\theta\right). \qquad \text{(C.10)}$$

For quartz $10\underline{1}0$, *MF(0)* and *MF(θ)* are then given by

$$MF(0) = M(3f_{si} + 6f_o) \qquad \text{(C.11)}$$

and

$$MF(\theta) = M\left\{\begin{matrix}2f_{si}\cos[2\pi(.465)] + f_{si}\cos(0) + 2f_o\cos[2\pi(.415)] + 2f_o\cos[2\pi(.143)] \\ +2f_o\cos[2\pi(.272)]\end{matrix}\right\}$$

$$= M\{(-.95)f_{si} + (-.75)f_o\}. \qquad \text{(C.12)}$$

M is calculated in terms of the unit cell volume by

$$M = \left(\frac{V}{d}\right)^{-1}, \qquad \text{(C.13)}$$

using the expression from crystallography

$$\left(\frac{V}{d}\right)^2 = (hbc\sin\alpha)^2 + (kac\sin\beta)^2 + (lab\sin\gamma)^2 + 2hk(abc^2)(\cos\alpha\cos\beta - \cos\gamma)$$

$$+ 2kl(a^2bc)(\cos\beta\cos\gamma - \cos\alpha) + 2lh(ab^2c)(\cos\gamma\cos\alpha - \cos\beta).^{(40)} \qquad \text{(C.14)}$$

a, b and *c* are points where the scattering plane intersects the axis and α, β and γ are the direction cosines between the axes in a particular crystal "system". For quartz which is a hexagonal "system", $\alpha = \beta = 90$, and $\gamma = 120$. To calculate *M* we need to know the Cartesian dimensions of the unit cell *a, b,* and *c.* For hexagonal crystals $a = b = a_o$ and we find that $M = 3.766 \times 10^{14}\ \text{cm}^{-2}$.

To finish calculating *MF(0)* and *MF(θ)* we need the scattering factor for Silicon f_{Si} and the scattering factor for Oxygen f_O. The angle independent scattering terms f_1 and f_2 in Eq. (C.5) are found in tables by wavelength for each element.[35] For the angle dependent term $\Delta f(\theta)$ we need to calculate $sin\theta / \lambda$ to find the atomic scattering factors f_o for Silicon and Oxygen. For quartz $10\underline{1}0$ at the wavelength $\lambda = 6.053$ Å the ratio is given by

$$\frac{\sin\theta}{\lambda} = \frac{1}{2d} = 0.12\,. \tag{C.15}$$

The atomic scattering factors for Silicon and Oxygen and were found in the tables to be $\Delta f(\theta)_{Si} = 11.35$ and $\Delta f(\theta)_O = 7.25$.[36] The scattering factors at $\lambda = 6.053$ Å are then given by

$$f_{si} = 12.33 + 3.58\,i - (14\text{-}11.35) = 9.68 + 3.58\,i \tag{C.16}$$

and

$$f_O = 8.31 + 0.51\,i - (8\text{-}7.25) = 7.56 + 0.51\,i, \tag{C.17}$$

resulting in

$$MF(0) = 3.2x10^{16} + 5.2x10^{15}\,i \tag{C.18}$$

and

$$MF(\theta) = (-6.7x10^{15}) + (-1.4x10^{15})i\,. \tag{C.19}$$

A computer program was used to compute the rocking curves from Eq. (C.1) for angles around the Bragg angle for both the σ and π states of polarization. These curves were then integrated to yield the reflected intensities R_σ and R_π. The ratio of the reflected

intensities for the π and σ polarization gives a measure of how the crystal polarizes incident x rays.

The resulting rocking curves for $\lambda = 6.053$ Å along with the results for two other wavelengths, 1.50 Å and 4.25 Å, are given in Figure C-2. The ratio of reflected intensities for the two states of polarization at these wavelengths are listed in table IV.

Table C-1. Ratio of integrated reflectivity for σ and π polarizations under Bragg reflection from quartz $10\underline{1}0$ for several wavelengths.

Wavelength (Å)	Angle (degrees)	R_π / R_σ
1.5	10	0.97
4.255	30	0.33
6.053	45.2	0.001

Most important for this experiment is the result for $\theta = 45^\circ$. Here only one state of polarization is reflected by the crystal.

C.2 TRANSMISSION AND REFLECTION FOR CRYSTALS OF N LAYERS.

Here we consider the reflection and transmission of x rays through a crystal composed of *N* layers. The calculation uses MDP to add all multiple reflections which occur in the crystal. The solutions are calculated in terms of the transmission per layer *x*.

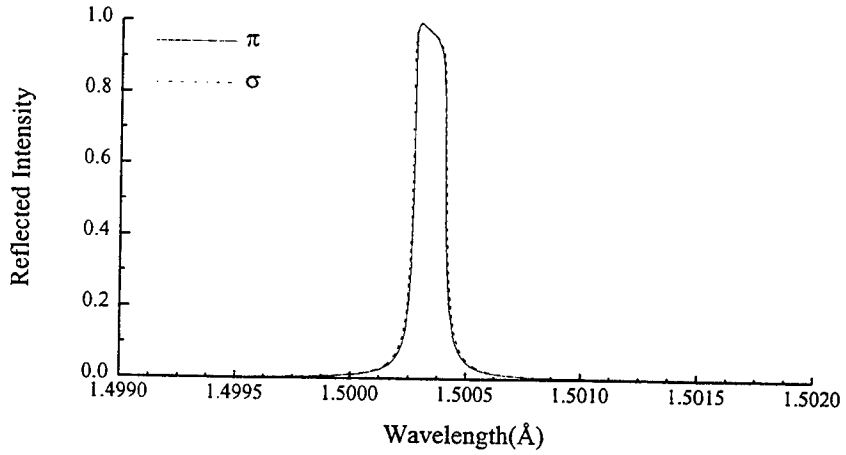

(a) $\lambda = 1.5$ Å

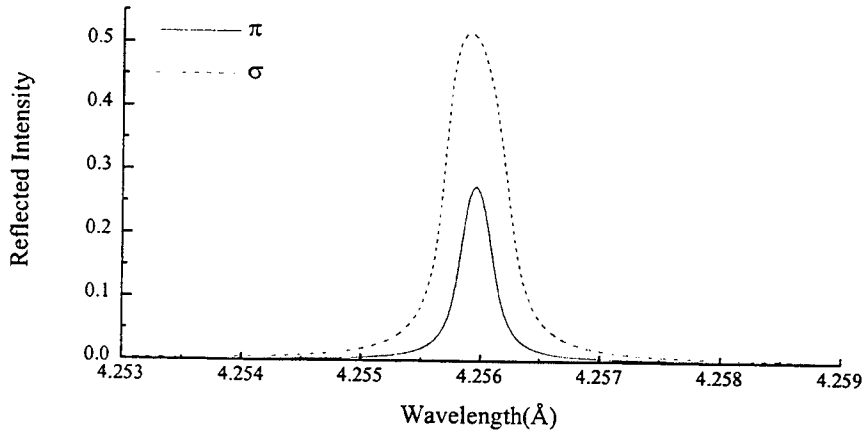

(b) $\lambda = 4.2$ Å

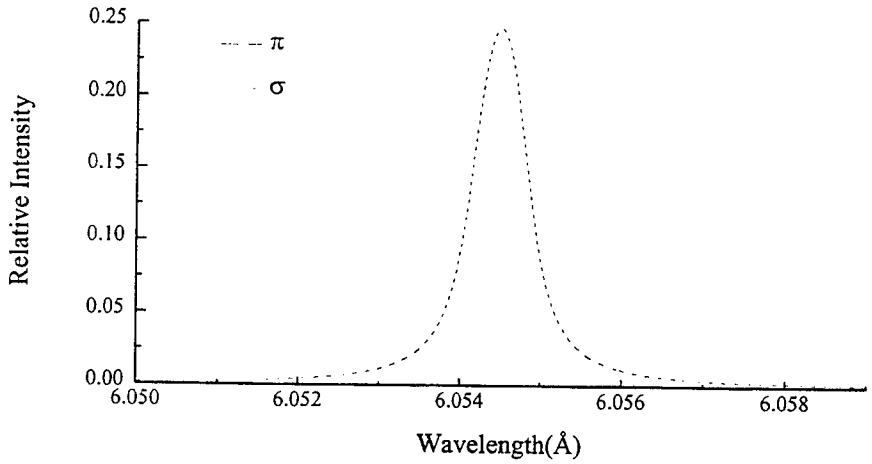

(c) $\lambda = 6.053$ Å

Figure C-2. Quartz $10\underline{1}0$ rocking curves under Bragg reflection for both the π and σ components.

$$x = (-1)^m \exp(-\eta), \tag{C.20}$$

where

$$\eta = \pm\sqrt{s\bar{s} - (\sigma + \varepsilon)^2}\,. \tag{C.21}$$

The parameters s, σ and ε are defined as in the case of a reflection from a thick crystal. The sign in η is chosen such that the real part of η is negative so the wave is attenuated as is passes through the crystal.

The reflected intensity and transmitted intensities for N layers are given by

$$R_N = \left|\frac{S_{0N}}{T_0}\right|^2 = \left|\frac{S_0}{T_0}\left[\frac{1 - x^{2N}}{1 - (S_0 / T_0)^2 x^{2N}}\right]\right|^2 \tag{C.22}$$

and

$$T_N = \left|\frac{T_{0N}}{T_0}\right|^2 = \left|x^N\left[\frac{1 - (S_0 / T_0)^2}{1 - (S_0 / T_0)^2 x^{2N}}\right]\right|^2. \tag{C.23}$$

C.2.1 Transmission and Reflection from N Layers of Quartz 10$\underline{1}$0.

The transmission and reflection for quartz 10$\underline{1}$0 was calculated for $N = 1000$, $N = 5000$, and $N = 10000$ under the Bragg condition $\lambda = 2d \sin\theta$. The calculations were performed for both states of polarization at $\lambda = 5.739$ Å. The values of *MF(0)* and *MF(θ)* for Quartz 10$\underline{1}$0 at this wavelength are *MF(0)* = $2.86 \times 10^{16} + 4.786 \times 10^{15}\, i$ and *MF(θ)* = $-5.80 \times 10^{15} - 1.320 \times 10^{15}\, i$.

The results of the transmission and reflection calculations for the different number of layers are shown in Figure C-3. Also included in these plots is the reflected intensity for the semi-infinite crystal for comparison. The plots show that away from the Bragg angle, the transmission through the crystal is the same as that from bulk material absorption of x rays. This is true for both states of polarization showing that the x rays that pass through the crystal which are not at the Bragg angle are not polarized.

In the vicinity of the Bragg angle, the reflection for the σ polarization increases with crystal thickness as expected until it reaches the semi-infinite crystal results. Here the transmission has a decrease from the bulk absorption transmission value. This is reasonable because as more intensity is reflected, less should be transmitted. On the other hand, the π polarization shows very little reflection. This is occurs because the Bragg angle is near 45° where the π polarization is not reflected with any significant intensity. The corresponding transmission shows little variation from the bulk transmission near the Bragg angle.

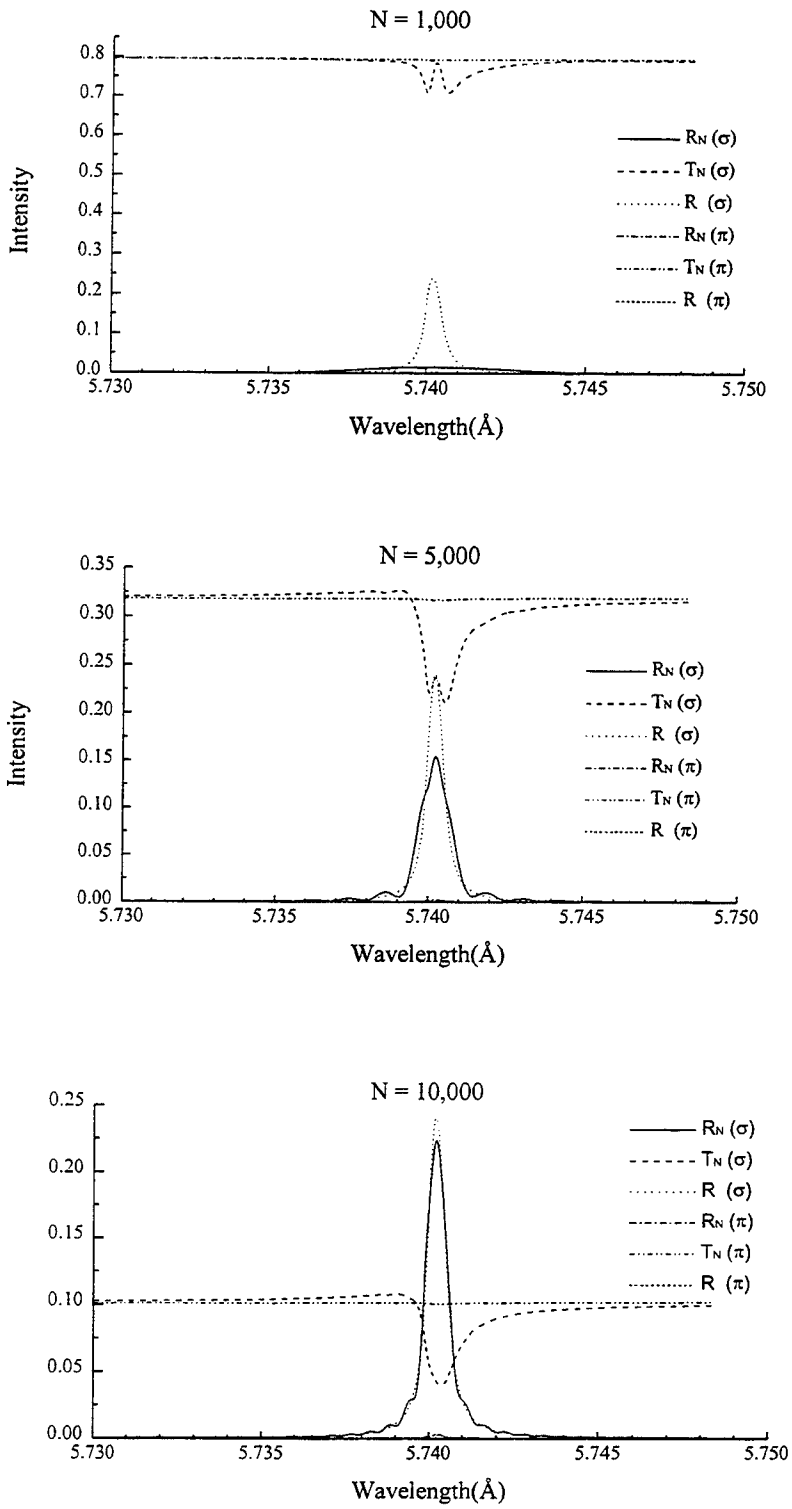

Figure C-3. Transmission T_N and reflection R_N of 5.739 Å from Quartz $10\underline{1}0$ for N layers and reflection R from a semi-infinite crystal.

APPENDIX D
RAY TRACING

D.1. RAY TRACING FOR JOHANN SPECTROMETERS.

Ray tracing involves tracing each x ray from the source to the detector to get an intensity distribution at the detector. In the calculations for the Phoenix experiment, we were interested in performing ray tracing for spectrometers in the Johann configuration for both a point and line source.

The Johann spectrometer consists of a crystal bent to radius of curvature of R with a detector placed on a circle of diameter R. A point or line source is placed a distance D from the center of the crystal at the Bragg angle corresponding to the line being observed. Figure D-1 shows this setup.

The procedure for finding the resulting intensity at the detector is as follows. Find the flux at the detector at a particular wavelength for a point in the source. Sum the contributions of flux from all points in the source at this given wavelength. This was the calculation performed by Morita to obtain the resolving power of the spectrometer for a line source at a given wavelength.[31] We extended this calculation by summing over the spectral profile at each point to produce a complete spectral profile from the source. The ray tracing equations derived from Morita are presented as the starting point.

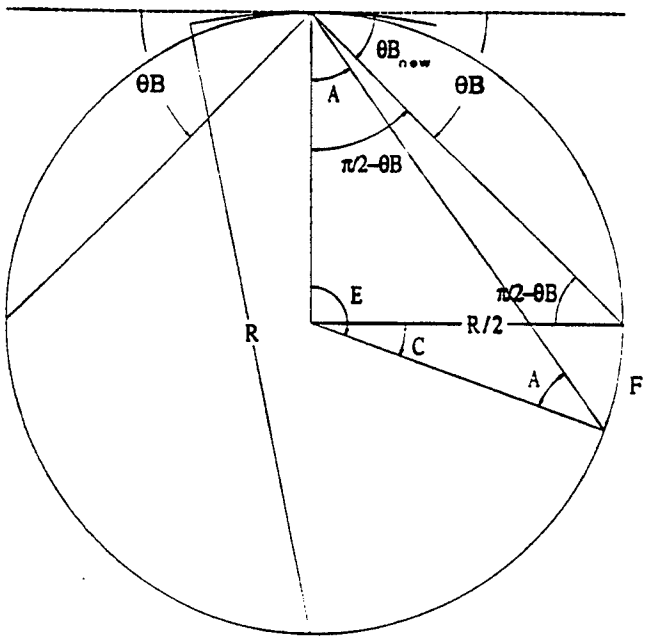

Figure D-1. Johann Spectrograph.

We assume that we have a source with a normalized spectral profile $J(\lambda-\lambda_0,x,y)$ and radiance $H(x, y)$. For a small area in the source $ds\,dz$, the flux emitted into the solid angle $d\xi\,d\psi$ in the directions of the ray being traced is given by

$$J(\lambda-\lambda_0,x,y)H(x,y)\cos(\xi)\,d\lambda\,ds\,dz\,d\xi\,d\psi\,, \tag{D.1}$$

where ξ is the angle relative to the normal of ds in the direction of the crystal as shown in Figure D-2 and $d\psi$ is the angle of elevation of the ray out of the plane of the spectrometer. The total flux received at the detector for a point source at a single wavelength is then given by

$$F = I(\lambda)\int W(\theta-\theta_B)\cos(\xi)\,d\lambda\,ds\,dz\,d\xi\,d\psi\,, \tag{D.2}$$

where $W(\theta-\theta_B)$ is a weight corresponding to the rocking curve of the crystal. This is the reflectivity of the crystal as a function of crystal angle for a particular wavelength. For most flat crystals the rocking curves have been measured to be Gaussian. In this calculation we assume a Gaussian rocking curve. This will not be a bad assumption since the radius of curvature of the crystal used in the experiment is large. The normalized rocking curve is expressed

$$W(\theta-\theta_B) = \sqrt{2}Ge^{-2\pi G^2(\theta-\theta_B)^2}\,, \tag{D.3}$$

with

$$G = \frac{2}{\theta_h}\sqrt{\frac{\ln 2}{2\pi}}\,, \tag{D.4}$$

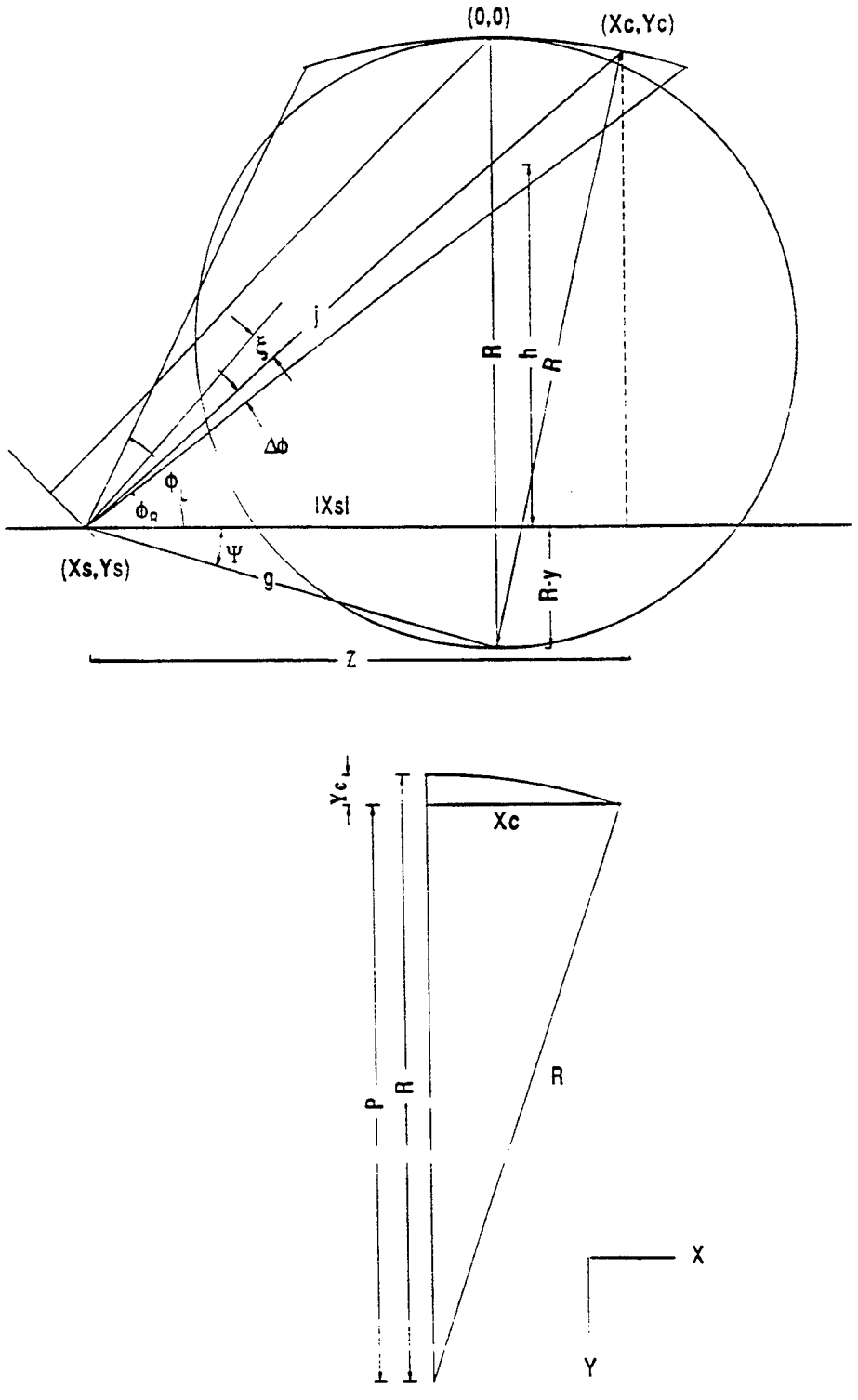

Figure D-2. Ray tracing geometry.

where θ_h is the halfwidth of the Gaussian line in radians. θ_h can be calculated using Bragg's law from the known resolving power of the crystal $\lambda / \Delta\lambda$.

Using the relationship for arc length $L_{scd} d\psi = dh$, with L_{scd} the source to crystal distance plus crystal to detector distance, we can write the flux in terms of the height *dh* at the detector

$$F = C\,dz\,dh\,I(\lambda)\int \frac{W(\theta - \theta_B)}{L_{scd}} \cos(\xi)\,ds\,d\xi . \tag{D.5}$$

For a point source s with a wavelength λ, the flux S at the detector will then be

$$S_{\lambda s} \propto I_s(\lambda)\int \frac{W_s(\lambda)}{L_{scd}} \cos(\xi)\,d\xi , \tag{D.6}$$

with $I_s(\lambda)$ being the relative intensity of the input point at the given wavelength λ.

Numerically, the integral in ξ becomes a sum over discrete angular steps starting from the right end of the crystal and proceeding to the left end of the crystal. Each angle is traced and the flux arriving at the detector is added to the appropriate bin in the detector. The angular step size must be small enough so that the continuous nature of the integration is not lost. Using the approximation that $\cos\xi \approx 1$, which is valid because the distance to the crystal is large compared to the size of the crystal, the discrete form of Eq. (D.6) becomes

$$S_s(\lambda) \propto I_s(\lambda)\sum_{\xi} \frac{W_{s\xi}(\lambda)}{L_{scd}} . \tag{D.7}$$

To calculate the spectra $N(\lambda)$ for an extended source at a single wavelength, we sum over all points in the source

$$N(\lambda) \propto \sum_s S_s(\lambda) = \sum_s I_s(\lambda) \sum_\xi \frac{W_{s\xi}(\lambda)}{L_{scd}}. \tag{D.8}$$

The final profile for the source is computed by summing over all the wavelengths in all of the source points. For a spectral profile $J_s(\lambda - \lambda_0)$, the flux at the detector is

$$F(\lambda - \lambda_0) \propto \sum_\lambda N(\lambda) = \sum_\lambda \sum_s J_s(\lambda - \lambda_0) \sum_\xi \frac{W_{s\xi}}{L_{scd}}. \tag{D.9}$$

This sum represents the total flux from every point and wavelength in the source.

To generate a profile we must add the flux from each ray in the source to the appropriate place on the detector. To do this we have to determine where each ray strikes the detector. The calculation begins by finding the point where each ray strikes the crystal, X_c and Y_c, as a function the angle Φ from the x axis to the ray being traced and the source point X_s and Y_s. Referring to Figure D-2 we can calculate X_c from

$$X_c = Z - X_s = j\cos(\Phi) - X_s, \tag{D.10}$$

by using

$$\tan(\phi_R + \Delta\phi) = \tan(\Phi) = \frac{h}{X_s} \tag{D.11}$$

and

$$R^2 = j^2 + g^2 - 2jg\cos(\Psi + \Phi), \tag{D.12}$$

where

$$g^2 = X_s^2 + (R - Y_s)^2,$$

$$\Psi = \cos^{-1}\left(\frac{X_s}{\sqrt{X_s^2 + (R - Y^2)^2}}\right), \tag{D.13}$$

and

$$\cos(\Psi + \Phi) = \cos(\Psi)\cos(\Phi) - \sin(\Psi)\sin(\Phi)$$

$$= \frac{X_s \cos(\Phi) + (R - Y_s)\sin(\Phi)}{X_s^{\,2} + (R - Y_s)^2}. \tag{D.14}$$

Solving the quadratic Eq. (D.12) for j

$$j = X_s \cos(\Phi) + (R - Y_s)\sin(\Phi)$$

$$\pm\cos(\Phi)\sqrt{(X_s \cos(\Phi) + (R - Y_s)\sin(\Phi))^2 - (X_s^{\,2} + (R - y)^2 - R^2)}. \tag{D.15}$$

Plugging this expression into Eq. (D.10) we then have

$$X_c = \cos^2(\Phi)\left[(1 + \sec^2\Phi)X_s + (R - Y_s)\tan(\Phi)\right]$$

$$\pm\cos^2(\Phi)\sqrt{X_s^2 + 2X_s(R - Y_s)\tan\Phi + (R - Y_s)^2\tan^2\Phi + \sec^2\Phi(2RY_s - X_s^2 - Y_s^2)}. \tag{D.16}$$

With the appropriate trigonometric identities this can be rewritten

$$X_c = \cos^2\Phi\left[(Y_s - R - X_s\tan\Phi)\tan\Phi \right.$$

$$\left. \pm\sqrt{(R^2 - X_s^2)\tan^2\Phi - Y_s^2 - 2X_sY_s\tan\Phi + 2RY_s + 2RX_s\tan\Phi}\right]. \qquad \text{(D.17)}$$

By defining $A = -\tan(\Phi)$ and $B = Y_s - AX_s - R$,

$$Xc = \frac{-AB \pm \sqrt{A^2B^2 - (1+A^2)(B^2 - R^2)}}{1+A^2}. \qquad \text{(D.18)}$$

From Figure D-3, since $R^2 = P^2 + X_c^2$ and $Y_c = R - P$, we find $Y_c = R - \sqrt{R^2 - X_c^2}$.

Once we have found out where each ray strikes the crystal, we can proceed to find the position, X_r and Y_r, where the rays strike the detector. We can find X_r and Y_r by finding the intersection of the line of the reflected ray from the crystal with the Rowland circle. From Figure D-2 we see that line from where the ray strikes the crystal to the detector is given by $Y = (X - X_c)\tan\alpha + Y_c$. Plugging this expression for Y into the equation of the Rowland circle, given by $X^2 + [Y - (R/2)]^2 = (R/2)^2$, with

$$(Y_r - R/2)^2 = (X_r\tan\alpha + Y_c - X_c\tan\alpha - R/2)^2$$

$$= (X_r - 2X_c)X_r\tan^2\alpha + (2Y_cX_r - RX_r - 2X_cY_c + RX_c)\tan\alpha_c^2$$

$$-2X_cX_r\tan^2\alpha + Y_c^2 - RY_c + \frac{R^2}{4}, \qquad \text{(D.19)}$$

we have

$$(1+\tan^2\alpha)X_r^2 + (2Y_c - 2X_c\tan\alpha - R)Xr\tan\alpha + Y_c^2 - RY_c + RX_c\tan\alpha$$

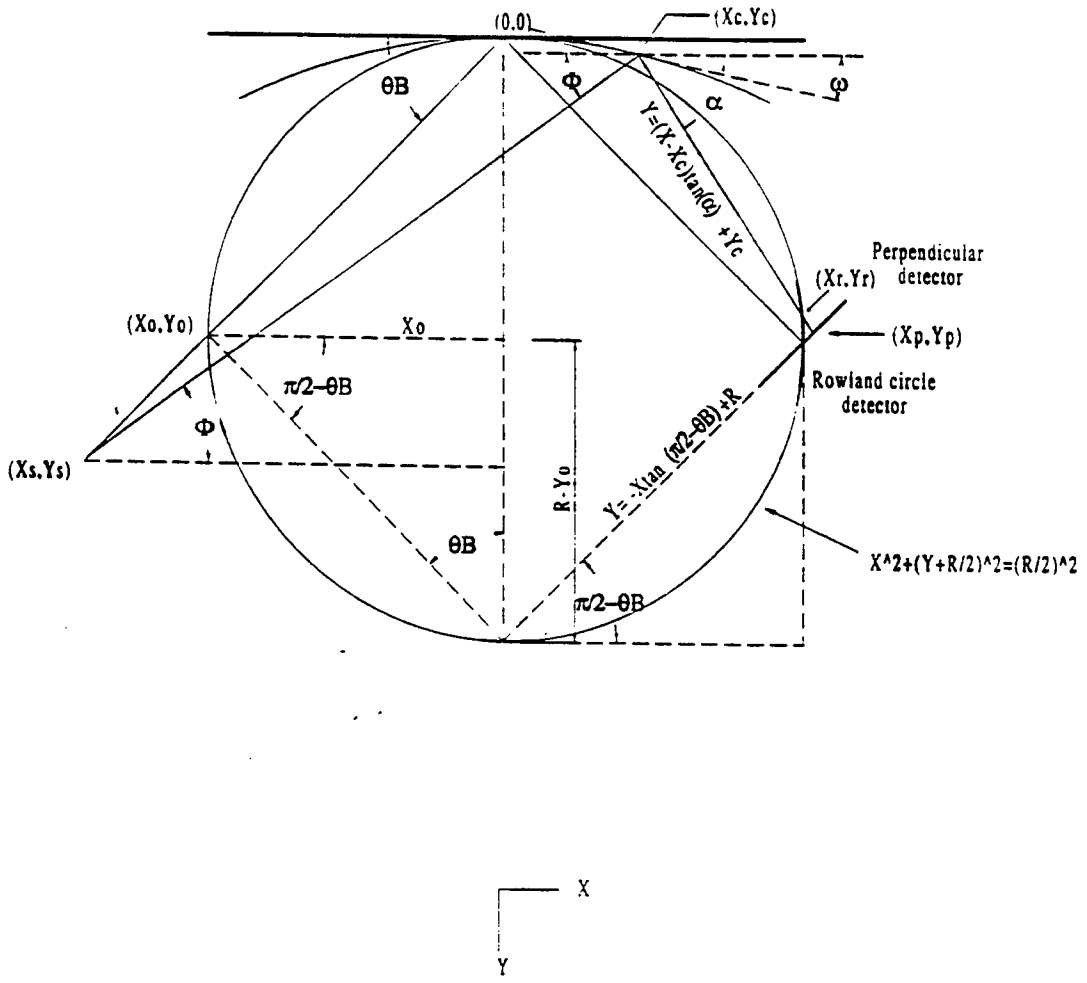

Figure D-3. Ray intersection with perpendicular and Rowland circle detectors.

$$-2X_c Y_c \tan\alpha + X_c^2 \tan^2\alpha = 0. \tag{D.20}$$

Simplifying this,

$$X_r^2 \sec^2\alpha + (2Y_c - 2X_c \tan\alpha - R)X_r \tan\alpha + Y_c^2 - RY_c + RX_c \tan\alpha - 2X_c Y_c \tan\alpha$$

$$+X_c^2 \tan^2\alpha = 0, \tag{D.21}$$

and letting

$$C = (2Y_c - 2X_c \tan\alpha - R)\tan\alpha \tag{D.22}$$

and

$$D = (X_c \tan\alpha - 2Y_c + R)X_c \tan\alpha + (Y_c - R)Y_c, \tag{D.23}$$

we then have

$$\sec^2\alpha\, X_r^2 + CX_r + D = 0. \tag{D.24}$$

Taking the positive root, since X_r will always be positive,

$$X_r = \frac{-C \pm \sqrt{C^2 - 4D^2 \sec^2\alpha}}{2\sec^2\alpha}, \tag{D.25}$$

and Y_r is then simply found from $Y_r = X_r \tan\alpha - X_c \tan\alpha + Y_c$.

Once we know where the ray strikes the detector, we have to add its flux to the appropriate part of the detector. For the ray tracing program, the length of the detector has to be divided into discrete bins. Otherwise each ray will arrive at a unique place on the film, to the precision of the computer, and the additive effect of flux from different regions of the source will be lost. Knowing the distance F, where the ray arrives along the detector from the center of the detector (X_0, Y_0), we can perform bin assignments as

$$Bin\ Number = \left(\frac{Number\ Bins}{2}\right)\left(1+\frac{2\,F}{L}\right), \tag{D.26}$$

where L is the length of the detector. With this expression, when F is L / 2, the flux is added to the last bin corresponding to the number of bins and when F is -L / 2, the bin number is zero. The minus sign refers to spectra on the detector closest to the crystal. Using this method the number of bins can be changed easily if necessary. The number of bins used in the simulations presented here is 100. Using too many bins in the calculation can present problems. The main problem is that intermediate bins may not get filled up. This is caused by too large an angle increment across the crystal compared to the distance between bins. This can be resolved by decreasing the angular steps in the ray tracing calculation, but this results in increased computational time.

With the rays properly assigned to their bins, then it is a simple matter finding the distance x of these bins on the detector

$$x = \frac{L[Bin\ Number - (Number\ of\ Bins\ /\ 2)]}{Number\ of\ Bins}. \tag{D.27}$$

When the bin number is zero, x will be equal to -L / 2 and when the bin number equals the number of bins, x will be equal to L / 2.

The bins then have to be converted from distance on the detector to wavelength. Figure D-4 shows the setup required for the calculation of the detector on the Rowland circle.

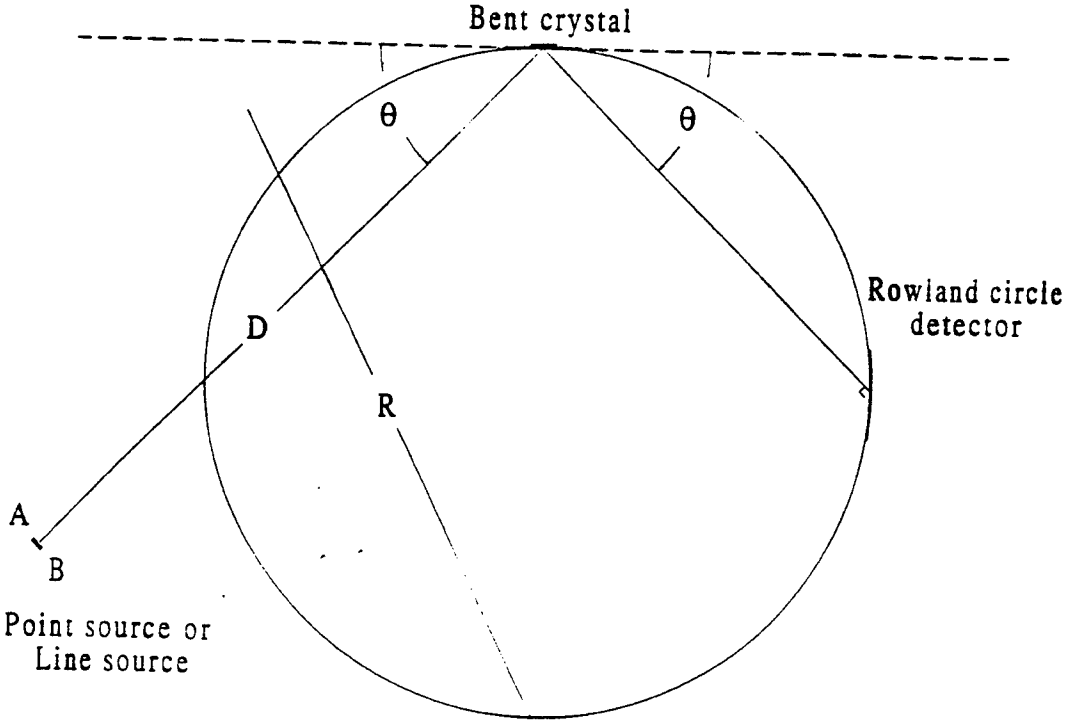

Figure D-4. Wavelength vs. position calculation for the Rowland circle detector.

To find the wavelength corresponding to a distance F from the center of the detector we must find the new Bragg angle corresponding to the position on the film.

From Figure D-4 the new Bragg angle is

$$\theta B_{new} = \frac{\pi}{2} - A = \theta_B + \frac{C}{2} = \sin^{-1}(\frac{\lambda_0}{2d}) + \frac{F}{R}, \tag{D.28}$$

and the wavelength corresponding to a distance F on the Rowland circle detector is then simply given by

$$\lambda_{RC}(F) = 2d\sin(\sin^{-1}(\frac{\lambda_0}{2d}) + \frac{F}{R}). \tag{D.29}$$

Using this expression, replacing F by x, we can calculate the wavelength of each of the bins that the rays are assigned to.

APPENDIX E
X-RAY FILM CALIBRATION

E.1 CALIBRATION OF KODAK BIOMAX MR FILM.

Kodak Biomax MR 4099 film was used in the spectrometers for the Phoenix experiments. This film is a high speed, high contrast film, with low fog designed for use in DNA sequencing autoradiography. The film is coated with a thin gelatin layer to help prevent damage to the emulsion. Since this film is not standardly used as x ray film for the wavelength region below 10 Å, calibration was necessary to determine the saturation level and the range of optical densities where the response of this film is linear. This calibration was performed for the L_β line of Al XIII using a vacuum spark source. The calibration was done by controlling the exposure of the film and measuring the resulting optical density of the film. The technique of Troussel and Dumont as shown in Figure E-1 was employed for this task.[40] A flat crystal spectrograph was used to disperse the x rays from an x ray source source and a stack of varying thickness absorption foils were placed in front of the film to vary the exposure across the spectral lines.

The source of the x rays used for the calibration of the Biomax MR film was a vacuum spark with an aluminum anode and cathode. Since the yield of x rays on vacuum spark is low, several hundred shots had to be taken to produce the intensities required to calibrate the film.

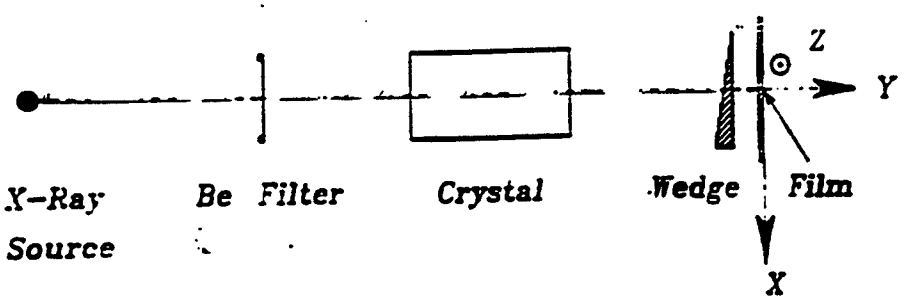

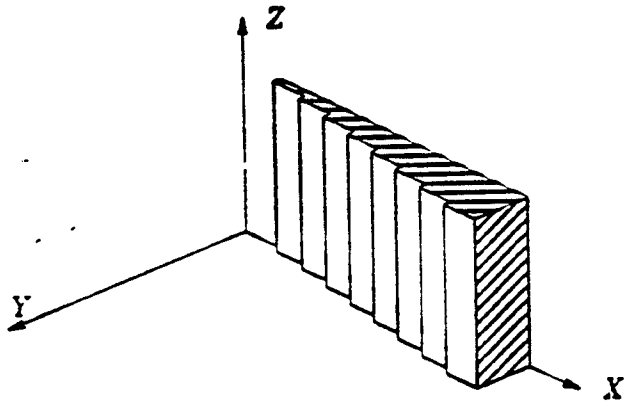

Figure E-1. Experimental arrangement for film calibration (Dumont and Troussel).

A flat crystal spectrograph utilizing a single ADP 101 crystal with $2d = 10.648$ Å was employed. The spectrograph varied slightly in design from the spectrograph presented in appendix A in that only one crystal was used. The spectrograph was designed in such a way that the ray reflected from the center of the crystal would strike the center of the film perpendicular to it. The crystal was located a distance of 32.4 cm from the source. The distance from center of the film to the crystal was 6 cm and the angle the crystal made with the center of the source was 38.9°, in order to place the L_β line in the center of the film. This configuration resulted in a dispersion of 2.2 Å/mm on the film. The aluminum spectra with no filters obtained with the flat crystal spectrograph for the vacuum spark is shown in Figure E-2. Table E-1 contains the line assignments for the spectra.

Table E-1. Aluminum spectra from vacuum spark.

Line ID	State	Transition	Wavelength (Å)	Designation
1	ALXIII	1s-7p	5.493	Lyman ξ
2	ALXIII	1s-6p	5.534	Lyman ε
3	ALXIII	1s-5p	5.605	Lyman δ
4	ALXIII	1s-4p	5.739	Lyman γ
5	AL XIII	1s-3p	6.053	Lyman β
6	AL XII	$1s^2$-1s5p	6.1745	NA

For the calibration to work correctly a scan across the L_β line needed to have a flat region in intensity, so that the difference in intensities getting to the film was only due to

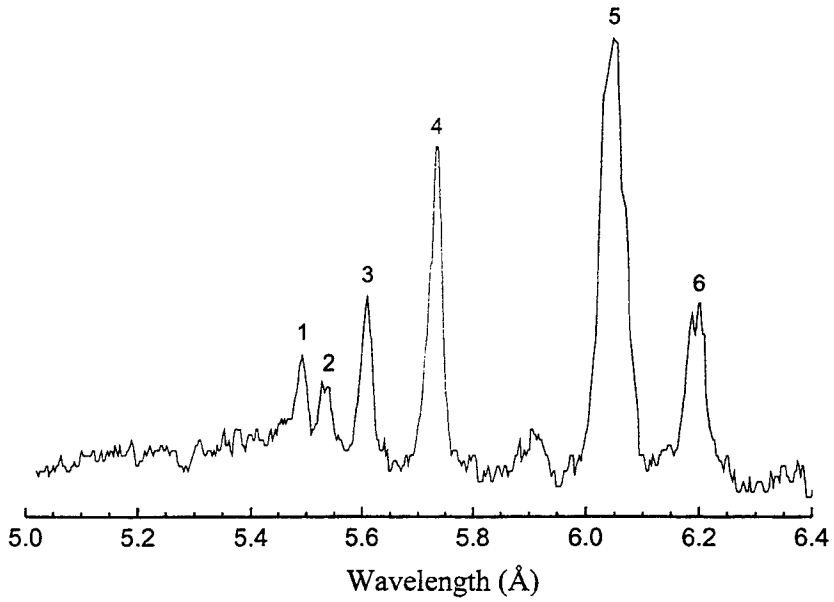

(a) Aluminum spectra from vacuum spark

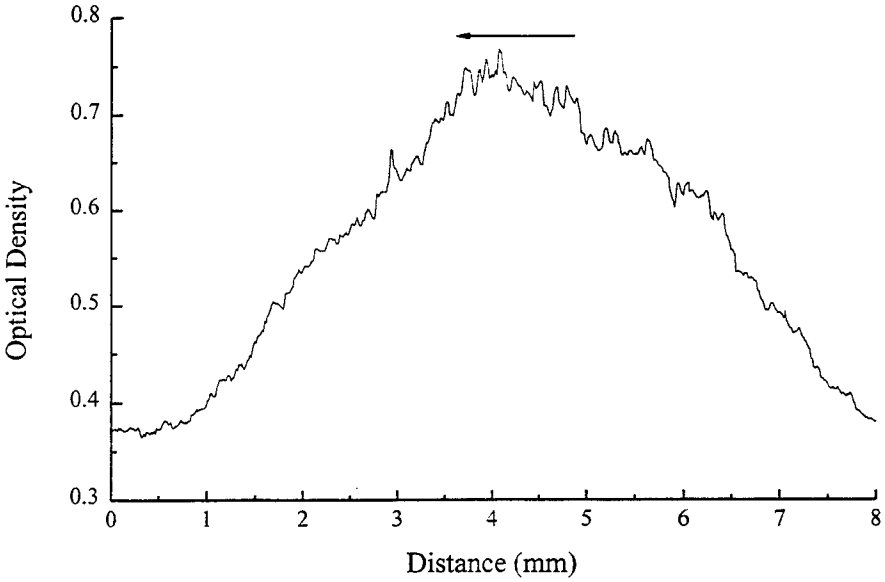

(b) Density scan across L_β line (5)

Figure E-2. Aluminum spectra obtained from vacuum spark and density scan across the L_β line (5).

the absorption foils and not to a variation in source intensity. A scan across the L_β line is shown in Figure E-2. For the region designated, the intensity does not vary more than 10%. The filters were then placed so the steps were within this region. The absorption foils placed in front of the film consisted of a stack of six 1-mil Be foils offset such that the width of each step was 0.1 mm, resulting in foil thicknesses which ranged from 1 to 6-mil.

The film was scanned using a Joyce Loebl scanning densitometer (Appendix F). An aperture of 0.1 was used with an occult of 0.7 mm, and a scan width of 50 μm. Either the C383 wedge or H5Z wedge was used depending upon the maximum density of the film. The density scale on the densitometer was calibrated on each film scan by using at least two of the following filters: Melles Griot 03FNG085 ($D = 0.5$), 03FNG015 ($D = 1.0$), and 03FNG023 ($D = 2.0$). To find the saturation level of the film, a piece of film was overexposed and scanned. This resulted in a saturation density of 2.73 ± 0.03.

The scans of the L_β lines where the step filters were used are shown in Figure E-3. To analyze the data, the background fog level (typically 0.39 ± 0.02) was subtracted. The recorded density of the various steps was tabulated for each set of data. The standard x ray transmission calculations for various thicknesses of Be were used to scale the theoretical exposure of the film.[27] The simple empirical model of Dumont et. al. was then used to generate response curves. The expression from Dumont et al. for the optical density is given by

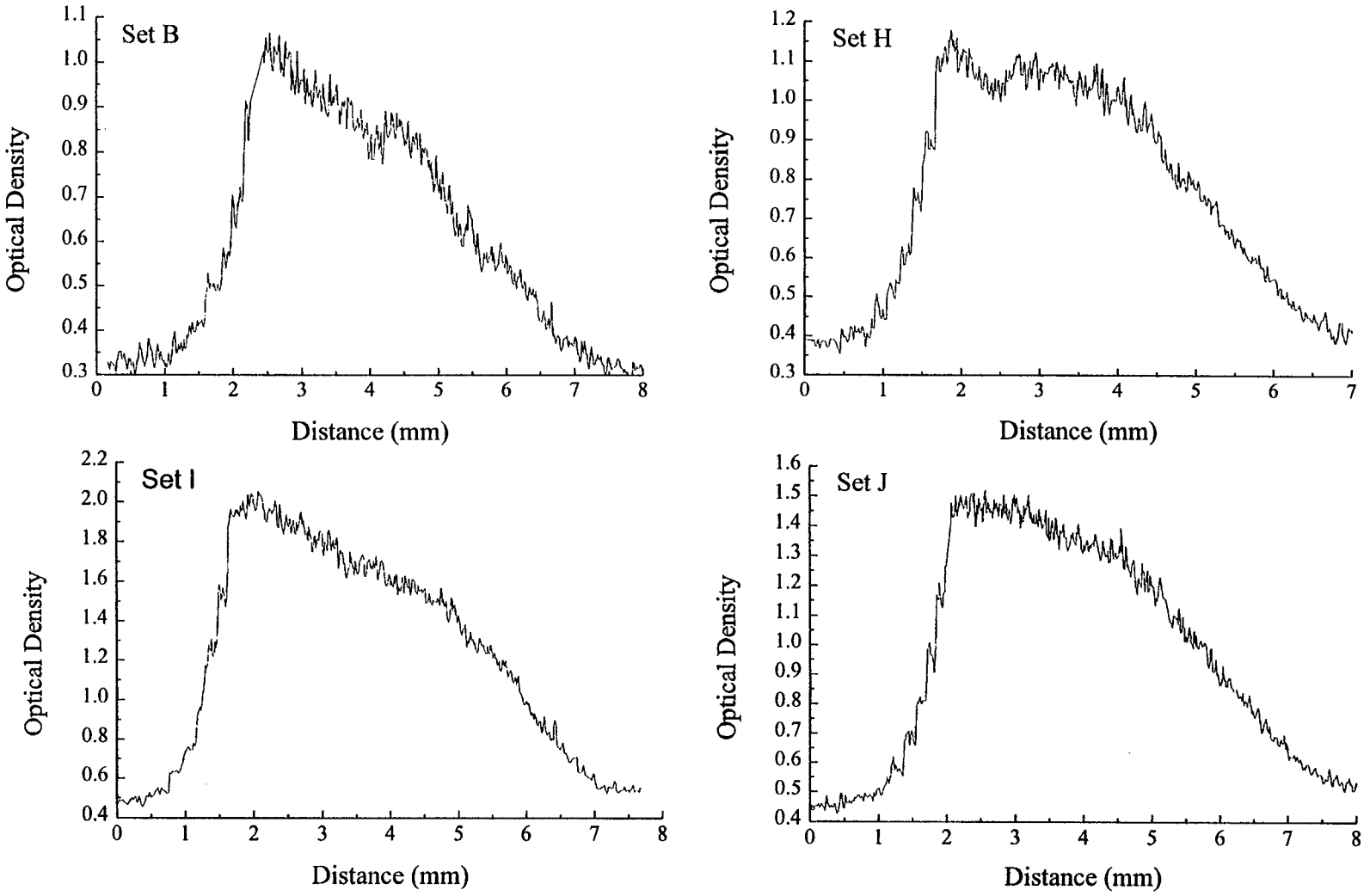

Figure E-3. Scans across the L β lines with Be step filters.

$$D = \frac{(L/L_0)^k}{1+(L/L_o)^k} D_{sat}, \qquad \text{(E.1)}$$

where L is an arbitrary exposure defined where an exposure of L_o leads to an optical density of $D_{sat}/2$. L_o was chosen to be 500. The equation for optical density was then fit to all of the data sets. For each set a k value was obtained. The data with the fits are shown in Figure E-4. The value of k varied from 1.33 to 1.58. The discrepancy of k between data sets can be attributed to poor filter placement and the difficulty of determining the intensity at each filter step. Poor filter placement resulted in a variation of the intensity across the film in addition to the variation imposed by the filters. The problem of determining the intensity levels at each step resulted from two factors, the quality of the step filter and the noise caused by graininess in the film. The poor quality of the step filter came from the difficulty of producing the Be foil stack without chipping away the edges of the brittle Be foils. A higher quality step filter could reduce this problem and produce better intensity plateaus. The noise could be reduced by enlarging the distance between steps so that the densitometer can scan with a wider slit. When using a vacuum spark, however, this makes it more difficult to get all of the steps in the region of constant intensity in the scan across the line.

From the data it can be seen that the region of linear response is approximately 1.7 orders of magnitude. It is necessary to make sure the lines analyzed in the experiment do not have peak optical densities, with fog subtracted, that exceed this level.

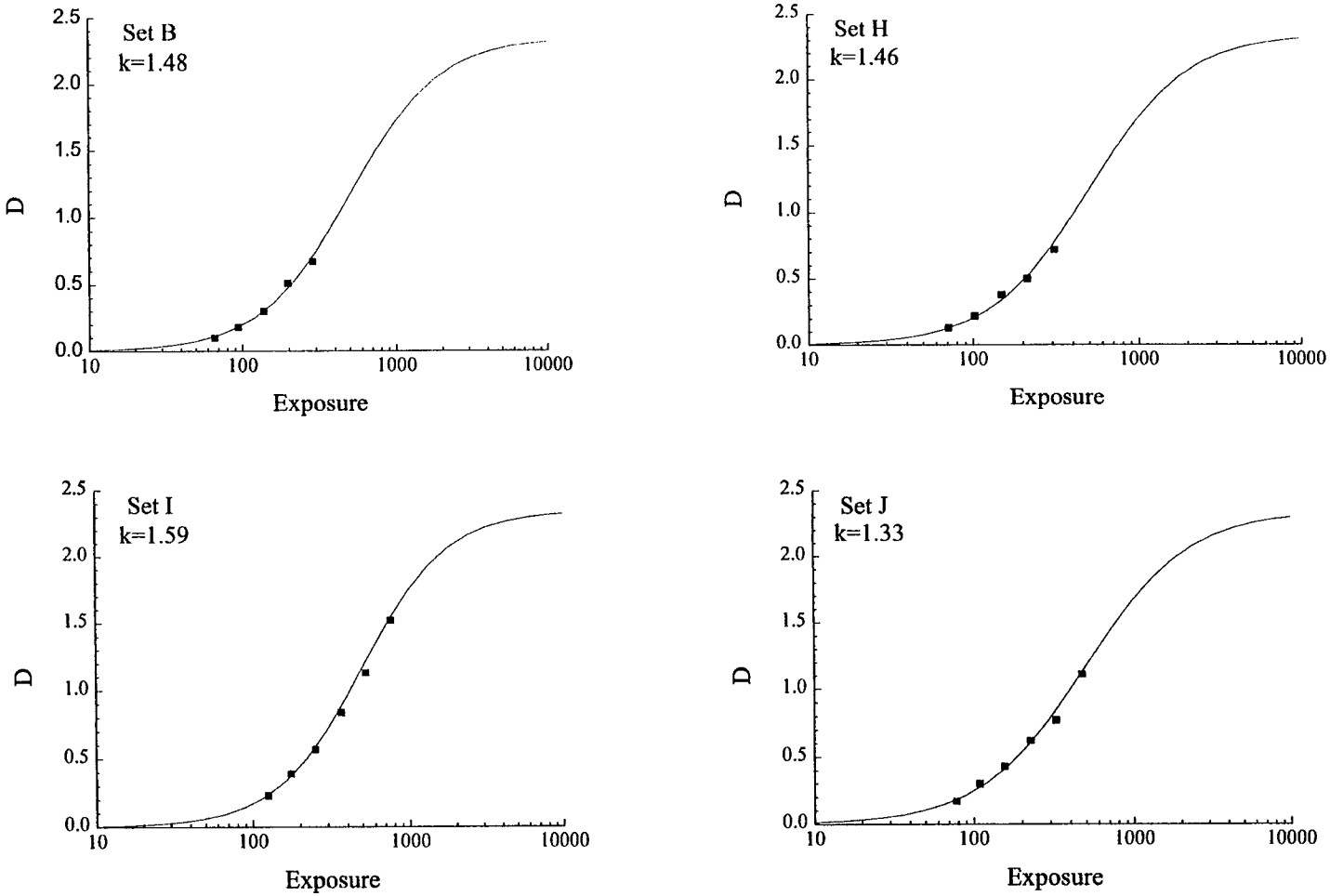

Figure E-4. Film calibration curves for L_β.

APPENDIX F
DATA SCANNING

F.1 JOYCE-LOEBL DENSITOMETER.

The spectral lines were scanned from the film using a Joyce Loebl microdensitometer, which measures the opacity of the film as a function of position. The schematic diagram for the densitometer is given in Figure F-1. Light from an incandescent bulb (A) is split into two optical paths. The light from one path passes through the sample (J) and the light from the other path is sent through a calibrated wedge with linearly varying optical density (K). The beams are brought together at a photomultiplier tube (E) which is switched to look alternately at each beam. A servo motor (N) moves the optical wedge so that the signal from both beam legs are the same. The recording pen is coupled to the wedge to produce the displacement in the pen.

F.1.1 Densitometer Parameters for Phoenix Data Scans.

The alignment procedure for the sample follows from the instruction manual for the Joyce Loebl instrument. For the Phoenix data, a 5x objective with 0.1 aperture lens was used in the instrument. The iris was set so that the slit height on the sample was 0.7 mm. A source slit width of 25 was used which corresponds to 50 μm on the sample. An arm ratio of 2 was used for all Johann Spectrometer data and 5 for all flat crystal data. The scans were run with a forward speed of 3.5. The H2Z wedge was used for the

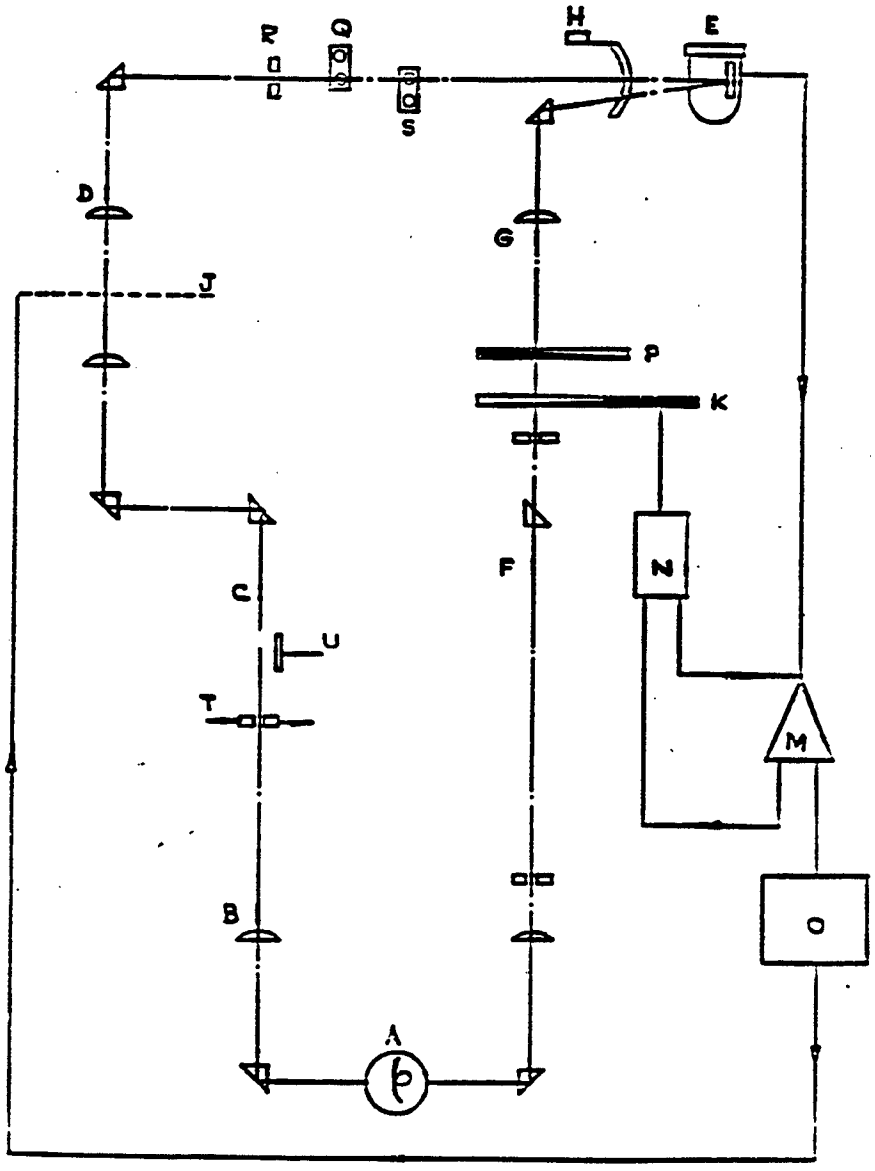

Figure F-1. Joyce Loebl scanning densitometer.

analysis of the Johann spectrometer data and the C383 wedge was used for the flat crystal data.

F.1.2 Data Digitization.

For data analysis it was necessary to have the data in digital form. The analog data from the Joyce Loebl were digitized using an Apple color scanner in combination with the program Datathief 1.0.8, which extracts the data from the scan. The scanning procedure follows. First the film was scanned on the densitometer in the usual way. A reference line was placed on the film horizontal to the spectra with a fixed length of 200 mm. The densitometer spectra was then scanned using Ofoto 2.0, a standard scanning program for the Apple Macintosh computer. The scanning software was set to scan a grayscale photo with 8:G scan bits, 135 scan dpi, 8:G print bits, and 135 print dpi. Once the spectra had been scanned it was checked for alignment. The horizontal reference marker was checked to ensure that it was aligned with the page. The spectra was rescanned if the scan was not aligned correctly. The data was then rotated to bring the spectra in the proper orientation. The focusing feature of Ofoto 2 was employed on the data to raise the contrast of the data so that it was more easily read by the DataThief program. Finally the data was saved in the PICT ColorSync Image format for use by the DataThief software. The final step to digitizing the data was to extract the numbers from the scanned image of the spectra. The program DataThief was used for this purpose. The program reads the x and y components of a line into numbers in text format. Once an image has been loaded into the program the *x, y* scales have to be assigned. For the Phoenix data, the x scale was

set using the 200 mm reference marker. This calibrated the scale of the spectra to mm (On the film the actual scale was half of this since the arm ratio used was 2). The *y* scale was chosen at the extremes of the page. A few parameters had to be set before the data was finally read in. The trace width and trace height tell the program how many pixels to look horizontally or vertically if there is a gap in the data, since the data from the scanner will not be perfect. A trace width of 4 pixels and trace height of 30 pixels was used. With the auto trace feature turned on, the spectral lines were scanned and data saved as text files. The data was then ready for manipulation by a standard scientific program package.

DISTRIBUTION LIST

DEPARTMENT OF DEFENSE

BALLISTIC MISSILE DEFENSE OFFICE
7100 DEFENSE PENTAGON
WASHINGTON, D.C. 20301-7100
ATTN: T/SL

DEFENSE ADVANCED RESEARCH PROJECTS AGENCY
3701 NORTH FAIRFAX DRIVE
ARLINGTON, VA 22203-1714
ATTN: DED

DEFENSE INFORMATION SYSTEMS AGENCY
PACIFIC AREA
WHEELER AFB, HI 96854-5000
ATTN: COMMANDER

DEFENSE TECHNICAL INFORMATION CENTER
8725 JOHN J KINGMAN RD., SUITE 0944
FORT BELVOIR, VA 22060-6218
ATTN: DTIC/OCP

DEFENSE THREAT REDUCTION AGENCY
45045 AVIATION DRIVE
DULLES, VA 20166-7517
ATTN: CPF, P HEBERT
ATTN: CPWP, T KENNEDY
ATTN: CPWT
ATTN: NSC
ATTN: NSS, JOAN MA PIERRE
ATTN: NSSA, G DAVIS
ATTN: NSSA, W SUMMA
ATTN: NSSE, W J SCOTT
ATTN: NSSS, K WARE
ATTN: NSSS, L PRESSLEY
ATTN: NSSS, R GULLICKSON
ATTN: NSSS, R SCHNEIDER
ATTN: TRC

DEFENSE THREAT REDUCTION AGENCY
ALBUQUERQUE OPERATIONS
1680 TEXAS ST. SE
KIRTLAND AFB, NM 87117-5669
ATTN: CPT
ATTN: SWP, G BALADI
ATTN: SWTI, R W SHOUP

NATIONAL DEFENSE UNIVERSITY
FORT LESLEY J MCNAIR
WASHINGTON, DC 20319-6000
ATTN: NWCO

NATIONAL SECURITY AGENCY
FORT GEORGE G MEADE, MD 20755-6000
ATTN: TECHNICAL LIBRARY

NET ASSESSMENT
OFFICE OF THE SEC OF DEFENSE
ROOM 3A930, THE PENTAGON
WASHINGTON, DC 20301
ATTN: DOCUMENT CONTROL

DEPARTMENT OF DEFENSE CONTRACTORS

ALME AND ASSOCIATES
ATTN DOC
P O BOX 4057
ALEXANDRIA, VA 22303
ATTN: JOHN F DAVIS
ATTN: S SEILER, G101

APTEK, INC.
1257 LAKE PLAZA DRIVE
COLORADO SPRINGS, CO 80906-3578
ATTN: T MEAGHER

AUBURN UNIVERSITY
DEPARTMENT OF PHYSICS
206 ALLISON LABORATORY
AUBURN, AL 36849-5311
ATTN: EUGENE J. CLOTHIAUX
ATTN: EUGENE OKS
ATTN: J D PEREZ

BERKELEY RSCH ASSOCIATES, INC.
P O BOX 852
SPRINGFIELD, VA 22150-0852
ATTN: N PEREIRA

CHARLES STARK DRAPER LAB, INC.
555 TECHNOLOGY SQUARE
CAMBRIDGE, MA 02139
ATTN: LIBRARY, MS #74

DEFENSE GROUP, INC
P O BOX 7522
SWNTA MONICA, CA 90406-7522
ATTN: ROBERT POLL

E-SYSTEMS, INC.
ECI DIVISION
P O BOX 12248
ST PETERSBURG, FL 33733-2248
ATTN: MAIL STOP 3, TECH INFO CTR

HY-TECH RESEARCH CORP.
104 CENTRE COURT
RADFORD, VA 24141
ATTN: E J YADLOWSKY

DISTRIBUTION LIST

DEPARTMENT OF DEFENSE CONTRACTORS

ITT INDUSTRIES
ITT SYSTEMS CORP
ATTN: AODTRA/DASIAC
1680 TEXAS ST SE
KIRTLAND AFB, NM 87117-5669
ATTN: DASIAC
ATTN: DASIAC/DARE

ITT SYSTEMS CORP
2560 HUNTINGTON AVENUE
ALEXANDRIA, VA 22303
ATTN: CLAUDE FORE

KTECH CORP.
2201 BUENA VISTA DR SE STE 400
ALBUQUERQUE, NM 87106-4265
ATTN: FRANK DAVIES

LOGICON RDA
2100 WASHINGTON BLVD
ARLINGTON, VA 22204-5706
ATTN: ED QUINN
ATTN: IHOR VITKOVITSKY

MAXWELL TECHNOLOGIES
8888 BALBOA AVE., BLDG. 1
SAN DIEGO, CA 92123
ATTN: JOHN THOMSON
ATTN: PHIL COLEMAN
ATTN: WILLIAM H RIX

PRIMEX TECHNOLOGIES, ORDNANCE
& TACTICAL SYSTEM
1840 FAIRWAY DRIVE
P O BOX 2055
SAN LEANDRO, CA 94577-0205
ATTN: B FAILOR
ATTN: H SZE

PULSE SCIENCES, INC.
600 MCCORMICK STREET
SAN LEANDRO, CA 94577
ATTN: TECHNICAL LIBRARY

SCIENCE APPLICATIONS INTL CORP
P O BOX 1303
MCLEAN, VA 22102
ATTN: W CHADSEY

SRI INTERNATIONAL
333 RAVENSWOOD AVENUE
MENLO PARK, CA 94025-3434
ATTN: ELECTROMAG SCI LAB TECH LIB

SVERDRUP INC AEDC
253 1ST STREET
ARNOLD AFB, TN 37389-2250
ATTN: L S CHRISTENSEN, MS 640
ATTN: V KENYON

TEXAS TECH UNIVERSITY
PULSED POWER LAB
PHYSICS DEPARTMENT
LUBBOCK, TX 79409
ATTN: L HATFIELD, M/S 1051
ATTN: M KRISTIANSEN, M/S 3102

DEPARTMENT OF ENERGY

LAWRENCE LIVERMORE NATIONAL LAB
P O BOX 808
LIVERMORE, CA 94551-9900
ATTN: L-477 C BACK
ATTN: L-477 L SUTER

SANDIA NATIONAL LABORATORIES
ATTN: MAIL SERVICES
P O BOX 5800
ALBUQUERQUE, NM 87185-0459
ATTN: C DEENEY MS 1194
ATTN: M K MATZEN/MS 1187
ATTN: TECH LIB

DEPARTMENT OF THE AIR FORCE

AFIWC/MSO
102 HALL BLVD STE 315
SAN ANTONIO, TX 78243-7016
ATTN: TECHNICAL LIBRARY

AIR FORCE FOR STUDIES & ANALYSIS
1570 AIR FORCE PENTAGON
WASHINGTON, DC 20330-1570
ATTN: SATI, RM 1D363

AIR FORCE RESEARCH LABORATORY
DIRECTED ENERGY DIRECTORATE
3550 ABERDEEN AVE., SE
KIRTLAND AFB, NM 87117-5776
ATTN: PL/WSP, J KIUTTU
ATTN: WSP/J DEGNAN

AIR UNIVERSITY LIBRARY
600 CHENNAULT CIRCLE
BLDG 1405 - ROOM 160
MAXWELL AFB, AL 36112-6424
ATTN: AUL-LSE

DISTRIBUTION LIST

DEPARTMENT OF THE AIR FORCE

ARNOLD ENGINEERING DEVELOLPMENT CENTER
1099 AVENUE C
ARNOLD AFB, TN 37389-9011
ATTN: MAJ J ROWLEY/DOT

SAN ANTONIO AIR LOGISTICS CTR
DIRECTORATE OF SPECIAL WEAPONS
KELLY AFB, TX 78241-5000
ATTN: ALC/SW MR F CRISTADORO

USAF ROME LABORATORY TECHNICAL LIBRARY, FL2810
CORRIDOR W. STE 262, RL/SUL
26 ELECTRONICS PKWY, BLDG 106
GRIFFIS AFB NY 13441-4514
ATTN: RBCM
ATTN: RBCT

DEPARTMENT OF THE ARMY

DEPUTY CHIEF OF STAFF FOR
OPERATIONS AND PLANS
PENTAGON
WASHINGTON, DC 20310-0460
ATTN: DAMO-ODW

US ARMY RESEARCH LABORATORIES
2800 POWDER MILL ROAD
ADELPHI, MD 20783-1197
ATTN: (TECH LIB)
ATTN: AMSEL-WT-NH/KEHS
ATTN: AMSRL-WT-KEHS

US ARMY SPACE & STRATEGIC DEFENSE
COMMAND
CSSD-TC-SR
P O BOX 1500
HUNTSVILLE, AL 35807-3801
ATTN: CSSD-ES-E1, R CROWSON

US ARMY THAAD PROJECT OFFICE
P O BOX 1500
HUNTSVILLE, AL 35807-3801
ATTN: CSSD-WD

US ARMY VULNERABILITY ASSESSMENT LAB
WHITE SANDS MISSILE RANGE, NM 88002-5513
ATTN: SLCVA-TAC

DEPARTMENT OF THE NAVY

NAVAL AIR SYSTEMS COMMAND
47123 BUSE RD, #IPT
PATUXENT RIVER, MD 20670
ATTN: AIR 5161
ATTN: AIR-5164
ATTN: AIR-933

NAVAL RESEARCH LABORATORY
4555 OVERLOOK AVE, SW
WASHINGTON, DC 20375-5000
ATTN: CODE 6720 J APRUZESE
ATTN: CODE 6720 J DAVIS
ATTN: CODE 6770 G COOPERSTEIN

NAVAL SURFACE WARFARE CENTER
17320 DAHLGREN ROAD
DAHLGREN, VA 22448-5000
ATTN: B DEPARTMENT

OFFICE OF NAVAL INTELLIGENCE
4251 SUITLAND ROAD
WASHINGTON, DC 20395-5720
ATTN: DEOO
ATTN: LIBRARY